DEVELOPMENT OF MOLECULAR CONTRAST-ENHANCED IMAGING FOR OPTICAL COHERENCE TOMOGRAPHY

A Dissertation

by

WIHAN KIM

Submitted to the Office of Graduate and Professional Studies of
Texas A&M University
in partial fulfillment of the requirements for the degree of

DOCTOR OF PHILOSOPHY

Chair of Committee,	Brian E. Applegate
Co-Chair of Committee,	Javier A. Jo
Committee Members,	Alvin T. Yeh
	Yong-joe Kim
Head of Department,	Anthony Guiseppi-Elie

May 2017

Major Subject: Biomedical Engineering

ABSTRACT

Biological imaging techniques that are able to detect a contrast-enhanced signal from the target molecules have been widely applied to various techniques in the imaging field. The complex biological environment provides numerous and more efficient pathways along which the chromophores (light absorber) may release its energy. This energy can provide not only morphological information, but also specific molecular information such as a biochemical map of a sample. All diseases correlate with both morphological and biochemical changes.

Optical coherence tomography (OCT) system is one of the biological imaging techniques. OCT has widely been applied to many medical/clinical fields, giving benefit from a penetration depth of a few millimeters while maintaining a spatial resolution on the order of a micron. Unfortunately, OCT lacks the straightforward functional molecular imaging extensions available for other technologies, e.g. confocal fluorescence microscopy and fluorescence diffuse optical tomography. This is largely because incoherent processes such as fluorescence emission and Raman scattering are not readily detectable with low coherence interferometry that is the central technique that underlies all OCT systems. Despite a drawback of molecular imaging with OCT, it is highly desirable to measure not only morphological, but also molecular information from either endogenous or exogenous molecules.

In order to overcome the limitation of molecular contrast imaging for OCT, our group has been researched the hybrid OCT imaging technique and a new exogenous contrast agent. Our contrast-enhanced imaging technique integrates OCT with a well-researched and well-established technique: two-colored pump-probe absorption spectroscopy. Our novel imaging technique is called Pump-Probe OCT (PPOCT). Based upon current successful results, molecular imaging with OCT potentially gives us the ability to identify pathologies. In order to expand the capacity of PPOCT, this dissertation focuses on development of molecular contrast-enhanced imaging for optical coherence tomography (OCT).

In the first phase of the research, we developed and optimized for sensitivity a two-color ground state recovery Pump-Probe Optical Coherence Tomography (gsrPPOCT) system and signal algorithm to measure the contrast-enhanced signal of endogenous and exogenous contrast agents such as Hemoglobin (Hb) and Methylene blue (MB) from in vivo samples. Depending on the absorption peak of a target molecule, the pump light sources for PPOCT used 532nm Q-switched laser or 663nm diode laser. Based on different experimental application, Ti:sapp or SLD of 830nm center wavelength were utilized. The PPCOT system was firstly used to image Hb of *in vivo* vasulature in a *Xenopus laevis* as the endogenous contrast agent and a larval stage zebrafish using MB as the exogenous contrast agent via transient changes in light absorption. Their morphological in addition to molecular specific information from a live animal was described. The incorporation of a pump laser in an otherwise typical spectrometer based OCT system is sufficient to enable molecular imaging with PPOCT.

In the second phase of this research, based on endoscopic molecular contrast-enhanced applications for OCT, we invented an ultra-wideband lensless fiber optic rotary joint based on co-aligning two optical fibers has excellent performance (~0.38 dB insertion loss). The developed rotary joint can cover a wavelength range of at least 355-1360 nm with single mode, multimode, and double clad fibers with rotational velocities up to 8800 rpm (146 Hz).

In the third phase of this research, we developed and manufactured a microencapsulated methylene blue (MB) contrast agent for PPOCT. The poly lactic-co-glycolic acid (PLGA) microspheres loaded with MB offer several advantages over bare MB. The microsphere encapsulation improves the PPOCT signal both by enhancing the scattering and preventing the reduction of MB to leucomethylene blue. The surface of the microsphere can readily be functionalized to enable active targeting of the contrast agent without modifying the excited state dynamics of MB that enable PPOCT imaging. Both MB and PLGA are used clinically. PLGA is FDA approved and used in drug delivery and tissue engineering applications. 2.5 μm diameter microspheres were synthesized with an inner core containing 0.01% (w/v) aqueous MB. As an initial demonstration the MB microspheres were imaged in a 100 μm diameter capillary tube submerged in a 1% intralipid emulsion. By varying the oxygen concentration both 0% and 21%, we observed he lifetime of excited triple state using time-resolved Pump-Probe spectroscopy and also the relative phase shift between the pump and probe is a reliable indicator of the oxygen concentration. Furthermore, these results are in good agreement with our theoretical predictions. This development opens up the possibility of using MB for 3-D oxygen sensing with PPOCT.

DEDICATION

To my family, parents and parents-in-law.

ACKNOWLEDGEMENTS

Thanks for all people those who support me.

NOMENCLATURE

OCT	Optical Coherence Tomography
PPOCT	Pump-probe Optical Coherence Tomography
Hb	Hemoglobin
MB	Methylene Blue
LMB	Leuco-methylene Blue
PLGA	Poly Lactic-co-glycolic Acid
FDOCT	Frequency-domain Optical Coherence Tomography
SDOCT	Spectral-domain Optical Coherence Tomography
SNR	Signal-Noise-Ratio
CNR	Contrast-Noise-Ratio
FORJ	Fiber Optic Rotary Joint
PTOCT	Photodermal OCT
EGFR	Epidermal Growth Factor Receptor
SOCT	Spectroscopic OCT
MMOCT	Magentomotive OCT
RGD	aRginine-Glycine-aspartic Acid
SPIOs	Superparamagnetic Iron Oxides
FDA	Food and Drug Association
SHOCT	Second Harmonic OCT
FLIM	Fluorescence Lifetime Imaging Microscopy

NADH	Nicotinamide Adenine Dinucleotide
LIF	Laser-Induced Fluorescence
SCST	Solid Sex Cord-Stromal Tumor
FAD	Flavin Adenine Dinucleotide
SCC	Squamous Cell Carcinoma
FLOT	Fluorescence Laminar Optical Tomography
RS	Raman Spectroscopy
SLO	Scanning Laser Ophthalmoscope
SEM	Scanning Electron Microscope
FD-PPOCT	Frequency-domain Pump-probe Optical Coherence Tomography

TABLE OF CONTENTS

LIST OF FIGURES

1. INTRODUCTION*

1.1 Background

Optical coherence tomography (OCT) is a rapidly developing imaging technology that is gaining clinical acceptance in cardiology and is widely used in clinical ophthalmology. Beyond what is currently FDA approved, OCT is being investigated as a tool for a variety of applications including; diagnosing cancer (e.g. esophageal [2, 3], bladder [4], and oral [5, 6] cancers), diagnosing skin diseases [7], monitoring wound/burn healing [8, 9], and assessing tumor margins [10, 11]. Similarly, OCT is playing a growing role in support of research into the development and progression of human disease as well as the development of organ systems in animal models [12].

OCT can provide tomographic images with micron scale resolution and rapid imaging speeds. Typically, the imaging depth in highly scattering tissues is 1-2 mm, but it can be much higher in weakly scattering tissues such as the eye. A unique aspect of OCT among other optical imaging technologies is that the axial resolution is independent of the lateral resolution. This feature is particularly important for imaging in the eye where the optics of the eye determine the lateral resolution. Likewise, imaging the coronary arteries requires a long depth of focus (lower lateral resolution) due to the fact that the relative position of the intravascular catheter endoscope to the artery lumen

---

* Parts of this section were taken from [1] P Mattison, Scott, Wihan Kim, Jesung Park, and Brian E Applegate. "Molecular Imaging in Optical Coherence Tomography." Current molecular imaging 3, no. 2 (2014): 88-105.

is not controlled. While the lateral resolution may suffer in both cases, the axial resolution can be maintained at the obvious expense of an asymmetric voxel. Typical lateral resolutions range from 10-40μm, whereas the axial resolution is inversely proportional to the frequency bandwidth of the light source and typically ranges from 3-15μm.

Cross-sectional and volumetric images are captured by scanning the illumination in x and y while collecting line images in z. Hence, the line-rate fundamentally limits the image acquisition speed. Typical line rates for OCT range from 50-200 kHz and are sufficient to mitigate many of the issues other imaging technologies have with motion artifact, even the fast saccades of the eye. Line rates in excess of 1 MHz [13, 14] have been demonstrated; opening up the possibility of measuring fast dynamical processes.

OCT fills a niche between the higher-resolution optical imaging technologies such as confocal reflectance microscopy and the lower-resolution technologies such as diffuse optical tomography. It offers high-speed, high-resolution tissue level imaging of morphology that cannot readily be generated in any other way. Unfortunately, OCT lacks the straightforward functional molecular imaging extensions available for these other technologies, e.g. confocal fluorescence microscopy and fluorescence diffuse optical tomography. This is largely due to the fact that incoherent processes such as fluorescence emission and Raman scattering are not readily detectable with the technique that underlies all OCT systems, low coherence interferometry. Fundamentally, OCT images are derived from measuring spatial variations in the intensity of backscattered near infrared light. These spatial variations arise from small changes in the tissue refractive index. Changes in the refractive index unfortunately correlate poorly with specific biomolecular species. These facts have made it difficult to develop functional extensions of OCT that would enable molecular imaging. Still, molecular imaging with OCT through either endogenous or exogenous contrast agents is highly desirable, as it would enable functional biomolecular imaging in addition to the morphological imaging available through standard OCT.

Given the growing penetration of OCT into clinical practice, robust molecular imaging extensions could have long term clinical impact. To that end, a significant effort has been brought to bear on the development of techniques to enable molecular imaging with OCT. A variety of approaches have been and are continuing to be developed. There is also a growing body of work dedicated to combining OCT with other optical imaging technologies that can already garner molecular information.

The primary examples of molecular imaging with OCT are photothermal OCT [15, 16], magnetomotive OCT [17, 18], and spectroscopic OCT [19, 20]. Photothermal OCT (PTOCT) provides absorption based contrast by monitoring changes in the optical path length caused by the photothermal effect [21] via phase-sensitive OCT. The primary contrast agent used with PTOCT is gold nanoparticles. It has also been shown to have some limited sensitivity to hemoglobin [22]. Magnetomotive OCT (MMOCT) exploits induced magnetic motion to enable molecular contrast in OCT. Since human tissues have a low magnetic susceptibility, the introduction of targeted magnetic particles to tissues enables MMOCT to provide highly sensitive molecular contrast [23]. An external electromagnet is modulated to induce nanometer scale motion which is then detected by phase-sensitive OCT. MMOCT has been used to image superparamagnetic iron oxides (SPIO) which are more commonly known for their use as MRI contrast agents [24,25]. Spectroscopic OCT [26] exploits the broad spectrum light sources used for OCT to garner absorption contrast. Spectral windows with different center wavelengths are typically formed in post processing to provide spectral resolution at the price of spatial resolution [27-29]. These techniques work best for highly peaked absorption spectra which can readily be separated from scattering based on their unique shape. Recent work using wavelengths down into the visible were able to measure absorption due to hemoglobin and blood oxygen saturation [30]. PPOCT integrates OCT with the pump-probe spectroscopy to provide molecular contrast. The pump-probe technique has been widely employed in experimental molecular physics to measure excited electronic states and molecular dynamics. It is well suited to imaging molecular chromophores like hemoglobin and methylene blue. It has a couple of advantages over spectroscopic OCT which is similarly sensitive to molecular chromophores. Contributions from absorption and scattering are easily separated so the absorption spectrum need not be highly peaked over the spectral bandwidth of the system. It has higher molecular specificity since there must be a resonance at both the pump and probe wavelengths. The molecular specificity can be improved by measuring the excited state lifetime. The excited state lifetime can also be used to measure quenching of the excited state, a mechanism commonly used in optical sensors for measuring changes in molecular concentration, e.g. oxygen. An obvious disadvantage compared to spectroscopic OCT is the increased complexity of the optical system, however in our most recent work I have largely mitigated this issue adding very common pump laser sources to an otherwise typical OCT system. An additional important point to make is that while PPOCT may use a pump in the visible, all of the applications we are proposing would use a probe in the near IR. Since the pump only needs to go it into the tissue (not back out like the probe) and we can tolerate multiple scattering events, we do not expect visible pump wavelengths to significantly limit the imaging depth of PPOCT. Especially, PPOCT is unique among the few available techniques for molecular contrast in OCT in that it can measure the excited state lifetime of the contrast agent which can be very sensitive to the local environment.

As an exogenous contrast agent, MB has a well-characterized singlet ground state absorption in the visible wavelength range and a triplet state absorption in the near infrared (NIR) range [31]. Also, MB is one of the few dyes that have been widely used for clinical applications. It was originally used as an antimalarial drug in the early 20th century and was the first synthetic drug [32]. More recently, methylene blue has been investigated for photodynamic therapy [33] and chemotherapy for melanoma [34] Additionally, MB has been shown to selectively stain specialized columnar epithelium in Barrett’s esophagus [35]. In the presence of oxygen, the lifetime of the MB excited triplet state is dramatically decreased, causing variations up to a few microseconds. The transfer energy within the oxygen molecules and the formation of the singlet oxygen causes to decrease the lifetime by a few microseconds [36]. This phenomenon makes MB as useful as an oxygen sensor.

Although MB has been utilized in the medical filed, it has photo toxicity to the applied area [37]. Also, pure MB is rapidly converted to its colorless leuco-methylene blue (LMB) that decreases absorption peak under caused by photobleaching and oxygen presenting [38]. PPOCT signal intensity is theoretically related to the scattering and absorption coefficient of a target sample [39]. In order to make MB more proper as the contrast agent using in vivo PPOCT, solvent evaporation technique using poly lactic-co-glycolic acid (PLGA) as the polymer is useful to encapsulated MB within a polymer shell [40]. PLGA is biocompatible, biodegradable, and has FDA approval [41]. It is commonly used for applications in drug delivery and tissue engineering. Given that both PLGA and MB are biocompatible and used clinically, their combination should yield a contrast agent that is well tolerated with the potential for eventual FDA approval. A microencapsulated MB contrast agent that offers several advantages over bare MB for in vivo PPOCT imaging. First, since the PPOCT signal is a function of both the scattering and transient absorption, scattering from the polymer used to encapsulate MB improves the PPOCT signal. Second, MB is photobleached to colourless LBM in vivo, thus diminishing the PPOCT signal since LMB is transparent at 663 nm. Microencapsulation sequesters the MB and prevents the reduction reaction. Finally, the surface of the polymer can be readily functionalized to enable active tagging of various receptors. While MB could also be functionalized for active tagging, it would risk altering the excited state dynamics that enable PPOCT via the transient absorption of the triplet state.

1.2 Objective and dissertation outline

The goal of the project is to develop a molecular contrast-enhanced system with OCT to image endogenous or exogenous contrast agent. These aims are reached using the following steps.

To begin, PPOCT system is designed and developed. In order to detect sensitively the signal from the endogenous or exogenous target molecule, a signal-processing algorithm is also optimized. The main OCT system is based on spectral-domain OCT (SDOCT) to have a few millimeters imaging penetration with a micron-scale imaging resolution. Depending on the absorption peaks of the target molecule, the wavelength of a pump and a probe light source is selected. As a part of the development, the system is validated calculating Signal-Noise-Ratio (SNR) and Contrast-Noise-Ratio (CNR) the measured PPOCT signal.

As a test of the PPOCT imaging system capabilities in a realistic ex or in vivo settings, Hemoglobin (Hb) and methylene blue (MB) are used as the target molecule. As an initial test, the Hb and aqueous MB were imaged in a capillary tube. We also demonstrate a pump-probe OCT (PPOCT) system capable of measuring molecular contrast-enhanced signal from a live animal. Xenopus tadpoles and zebra fish in particular have been chosen because they are a frequent target for optical imaging due to their size and relative translucence, and the fact that they are a common model for developmental biology [42]. Especially a zebra fish in larval stage was stained with MB by submersion in a 0.01% (w/v) solution of MB for 6 hours. The PPOCT image collected from the zebra fish is evaluated a PPCOCT system's capability to provide morphological and molecular contrast-enhanced images that can be correlated to each other and to the corresponding histology.

In order to expand the application of the molecular contrast-enhanced system with OCT on the clinical field such as intravascular optical imaging in arteries using catheter endoscopes, it is necessary to use very broad spectral bandwidths (near UV to short-wave IR) and specialized optical fibers, such as double-clad fiber, and have the capacity to accommodate high rotational velocities. A lensless fiber optic rotary joint (FORJ) based on co-aligning and placing in contact two optical fibers is developed. The capability of developed lensless FORJ is demonstrated with a wide range of wavelength (355~1360nm) and high rotational velocities.

In order to overcome the limitations of MB as a contrast agent for *in vivo* PPOCT, microencapsulated MB is fabricated based on PLGA. The capability of a MB microsphere as a new contrast agent for PPOCT was tested. As an initial demonstration simulated with biological conditions, the MB microspheres is imaged in a 100 μm diameter capillary tube submerged in a 1% intralipid emulsion and on the gelatin based artificial tissue. In order to use a MB microsphere as the oxygen sensor, the lifetime of transient absorption and relative phase shift are measured using time-resolved Pump-Probe spectroscopy and PPOCT by varying the oxygen concentration from 0% to 21%.

This dissertation mainly is composed with the design, development and validation of molecular contrast-enhanced system and a new contrast agent for OCT.

Based on the aforementioned objectives, this dissertation has been organized as follows:

Chapter 2 does primarily be dedicated to the former, i.e. techniques that derive their molecular information directly from OCT images. It provides some basic understanding of the physical process being exploited, noting some of the distinct properties of each technique, along with the essential technical details of the optical system. Subsections introduce each technique of molecular contrast-enhanced OCT system.

Chapter 3 describes the design and development of the PPOCT system, and provides experimental *ex/in vivo* results.

Chapter 4 shows the lensless and ultra-wideband fiber optic rotary joint for endoscopic molecular-enhanced OCT imaging, and also describes how the performance of FORJ was tested.

Chapter 5 discusses the design and development of the microencapsulated MB using PLGA as a new contrast agent for PPOCT. First subsection describes the how the microencapsulate MB was tested for PPOCT. Second subsection deals with how the microencapsulated MB works using PPOCT as the oxygen sensor.

Parts of [1] have been dealt with permission and arranged throughout the dissertation.

2. MOLECUALR IMAGING IN OPTICAL COHERENCE TOMOGRAPHY[*]

This chapter primarily deals with the former, i.e. techniques that derive their molecular information directly from OCT images. It provides some basic understanding of the physical process being exploited, noting some of the distinct properties of each technique, along with the essential technical details of the optical system. Subsections introduce each technique of molecular contrast-enhanced OCT system.

2.1 Photothermal OCT

2.1.1 Theory of Photothermal OCT

Photothermal OCT (PTOCT) provides absorption based contrast by monitoring changes in the optical path length caused by the photothermal effect [43]. In the photothermal effect, photons are absorbed by chromophores within a sample causing a localized rise in temperature. Thermoelastic expansion caused by the photothermal effect generates isolated variations in the refractive index which in turn generates a variation in the optical path length [44]. The optical path length variations typically generated by the photothermal effect, often nanometer in scale, can be resolved with phase-sensitive OCT [45, 46].

PTOCT utilizes separate laser sources for photothermal excitation and OCT signal generation. The photothermal source is coupled into the sample arm of the OCT

---

[*] Reprinted with permission from [1] P Mattison, Scott, Wihan Kim, Jesung Park, and Brian E Applegate. "Molecular Imaging in Optical Coherence Tomography." Current molecular imaging 3, no. 2 (2014): 88-105.

system. Amplitude modulation of the photothermal source enables the differentiation of photothermal heating from the scattering signal [46]. Selecting the ideal wavelength for absorption by the target chromophore enables specific molecules to be targeted. Figure 1 depicts a typical schematic for performing PTOCT.

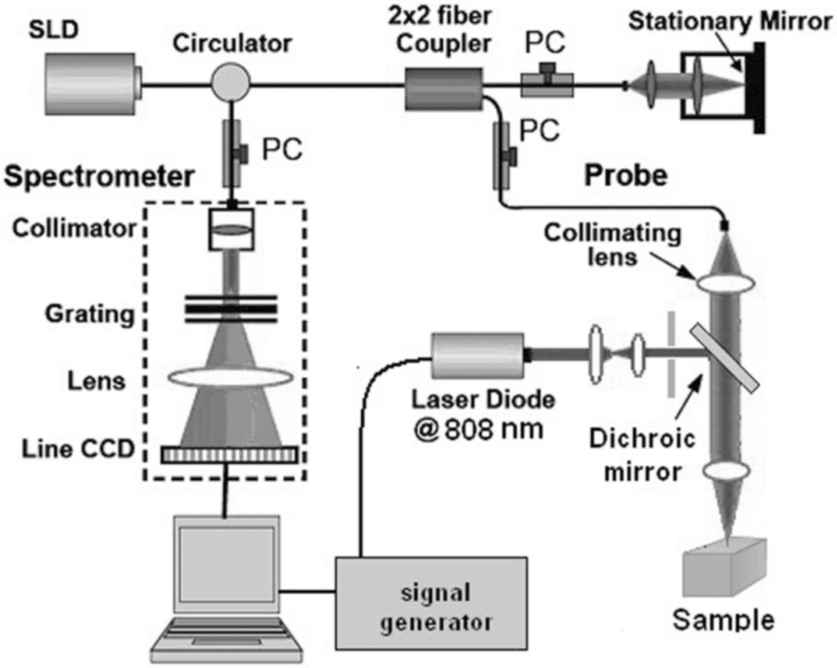

Figure 1: Schematic diagram of the photothermal phase sensitive spectral domain optical coherence tomography system. Reprinted with permission from [47]

In most applications of PTOCT, a series of temporally resolved depth scans (M-mode scans) are obtained. Following a Fourier transform of the OCT phase data at each point in depth, the magnitude of the PTOCT data is located at the modulation frequency of the photothermal laser[46, 48]. Prior studies have investigated the relationships between the magnitude of PTOCT signal and the concentrations of the target chromophores [46, 48]. Additionally, a relationship has been demonstrated between PTOCT signal and the intensity of the photothermal source. The magnitude of the phase shift generated in the OCT signal, Δφ, is related to the change in refractive index per unit temperature of the sample, $\frac{\partial n}{\partial T}$, the thermal conductivity, k, the center wavelength, λ, the concentration of the absorbing sample, and the size of the excitation volume [48-51]. For gold nanoparticles, a common target of photothermal OCT, the phase shift, elicited by the photothermal response can be approximated by Eq. 1 [48].

$$\Delta\phi = .64\left[\frac{\partial n}{\partial T}\frac{1}{k}\right]\left[\frac{I(\vec{r}_0)}{\lambda}\right]N\sigma \qquad (1)$$

Where N is the number of gold nanoparticles in the optical excitation volume, and $I(\vec{r})$ is the intensity of the photothermal source.

A variety of work has gone into improving the sensitivity of PTOCT. As Eq. 1 shows, the magnitude of the PTOCT signal is linearly dependent upon the optical intensity of the photothermal source as well as the concentration of the targeted chromophore. However, as the modulation frequency of the photothermal source increases, the signal strength decreases logarithmically [49]. A range of modulation frequencies from 25 Hz up to 120 kHz have been explored. Due to the logarithmic decrease in signal with modulation frequency, there is a trade-off between image speed and signal strength. Additionally, while the amplitude of the OCT signal does not directly impact the intensity of the PTOCT signal, lower OCT signal amplitude increases the noise of PTOCT. Complex post processing algorithms have been attempted to increase phase sensitivity, including averaging of overlapping short time Fourier transforms [49], subtraction of frequency components to compensate for additive noise [51], and polynomial background order subtraction [48, 52].

An alternative approach for monitoring the photothermal signal has been explored through photothermal optical lock-in optical coherence microscopy (OCM). Phase modulations are generated in the reference arm to match the amplitude modulation frequency of the heating beam. The result is a demodulated photothermal signal of the absorbers without the need for m-mode scanning [53].

2.1.2 Applications

Photothermal OCT is often used to monitor exogenous contrast agents, most notably gold nanoparticles. In addition to their biocompatibility, gold nanoparticles are desirable because they have established methods for molecular targeting, and can easily be used for photothermal therapy [54]. PTOCT imaging of immunotargeted gold nanoparticles has been demonstrated by Skala, *et al* for detection of epidermal growth factor receptor (EGFR) [48]. EGFR is a cell surface receptor which binds specific ligands, and mutations to EGFR which have been linked to the formation of cancer [55, 56]. To target EGFR, gold nanospheres were conjugated with EGR specific antibodies. The targeted nanospheres were placed in cell cultures expressing EGFR (Figure 2(a)) and cell cultures with no expression of EGFR (Figure 2(b)). Additionally, non-targeted nanospheres were added to cell culture containing cellular overexpression of EGFR (Figure 2(c)). Figure 2(d) demonstrates the specific targeting of the antibody conjugated nanoparticles to cellular expression of EGFR.

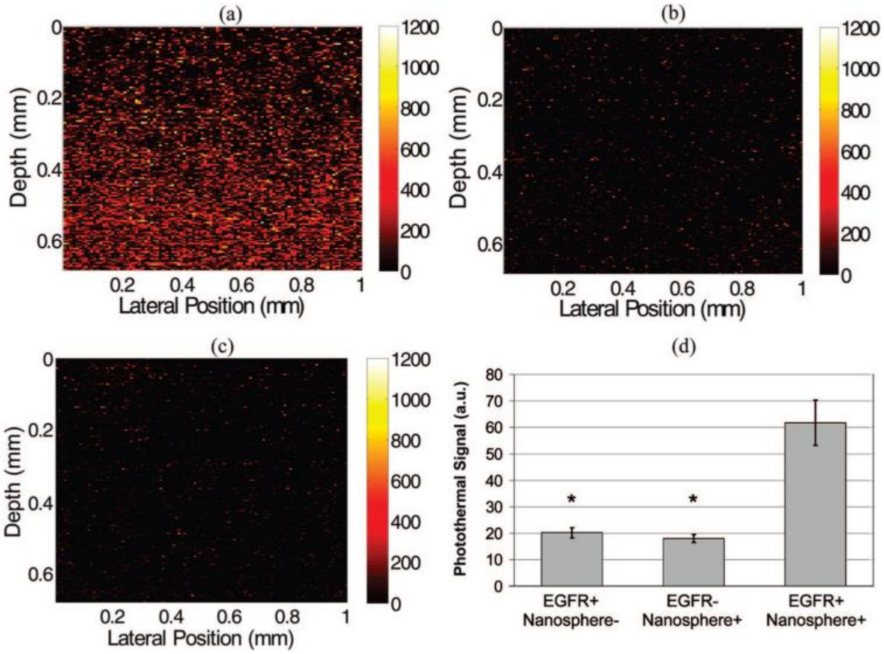

Figure 2: Images of EGFR expression in three-dimensional cell constructs containing EGFR+ cells (MDA-MB-468) with and without antibody-conjugated nanospheres (a and c, respectively) and EGFR- cells (MDA-MB-435) with antibody-conjugated nanospheres (b). There was a significant increase in the photothermal signal from EGFR overexpressing cell constructs labeled with antibody conjugated nanospheres (d) compared to the two controls (EGFR+/Nanosphere- and EGFR-/Nanosphere+). $N = 17$ images for each group, (*, $p < 0.0001$). Pump power 8.5 kW/cm2. Reproduced with permission from [48].

To the best of our knowledge, this is currently the only documented use of a targeted contrast agent for PTOCT imaging of nanoparticles. However, gold nanoparticles have widely been used for targeted molecular contrast for various applications [58]. Tumors are also often passively labeled with gold nanoparticles via the enhanced permeability and retention effect [59]. Other exogenous contrast agents have been demonstrated in the form of carbon nanorods [52], polypyrrole nanoparticles [60], indocyanine green encapsulated by poly (lactic-co-glycolic) acid nanoparticles [61], and iron oxide-silica-gold nanoprobes [62].

While PTOCT has largely been applied to exogenous contrast agents, it can potentially be used to image a variety of endogenous chromophores. If we take guidance from photoacoustic microscopy, which operates via a similar contrast mechanism, there is the potential to generate PTOCT images targeting nucleic acids, cytochromes, hemoglobin, and melanin [63-65]. To date only hemoglobin has been successfully measured with PTOCT. Milner and coworkers developed a dual wavelength PTOCT system to characterize the oxygen saturation of hemoglobin. Using 780 nm and 800 nm pump wavelengths coupled with a 1064 nm center wavelength OCT system the oxygen concentration of hemoglobin in a 300 μm microvessel phantom was monitored. Figure 3(a) shows an en-face image of this sample, while Figure 3(b) shows a b-scan of the region of interest. Using a dual wavelength approach enables PTOCT to monitor the oxygenation of blood. [66]. Figure 3(c) compares the measured oxygen concentration of porcine blood via PTOCT compared to a reading taken using a commercial oximeter [67].

The interest in PTOCT is a rapidly expanding, especially for applications with gold nanostructures. Gold nanoshells and similar plasmonic nanostructures are being investigated for a number of biomedical applications that exploit their tunable plasmon resonances, including biomolecular sensing [68, 69], imaging [70, 71], and diagnostics [72, 73]. They are also under investigation for therapy with ongoing clinical trials for the treatment of primary prostate cancer and primary and/or metastatic lung tumors [74]. Robust PTOCT imaging technology has the potential to make an impact across many of these areas of interest.

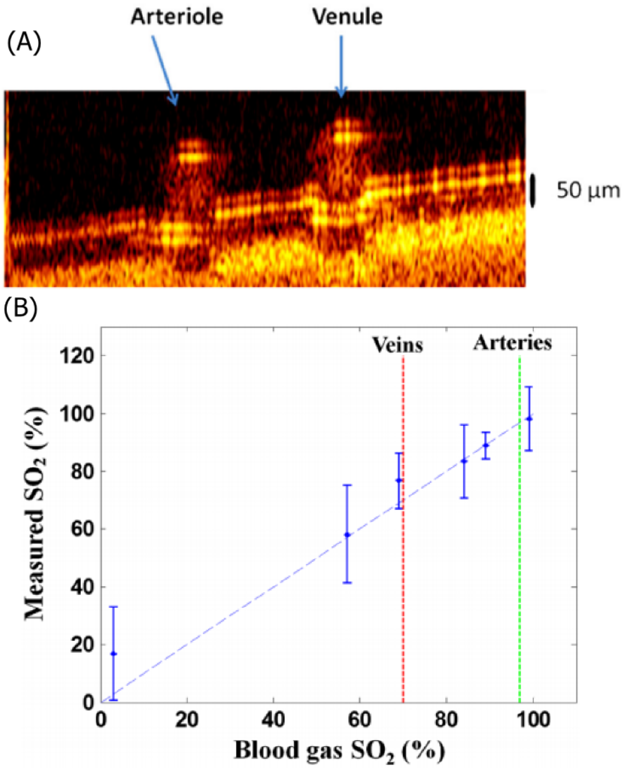

Figure 3: (a) B-scan PTOCT image of an arterial-venous phantom sample. (b) Blood SO2 level measured by DWP-OCT (vertical) versus oximeter values (horizontal). Blood is stationary for all measurements. Modified from [67].

2.2 Spectroscopic OCT

2.2.1 Theory of SOCT

Absorption spectroscopy is a common analytical tool used to identify specific molecules, sometimes in very complex samples, not unlike biological tissues. All molecular species have the capacity to absorb light. The absorption spectrum is characteristic of a particular molecular species, but also sensitive to environment. The broad spectral bandwidth of low-coherence light sources used in OCT, especially those used for ultrahigh resolution, are well suited to measuring absorption spectra. Thus, a natural method to achieve molecular contrast via OCT is through what is known as spectroscopic OCT (SOCT) [75] which exploits the broad spectrum light source to garner absorption contrast.

In SOCT there is always a competition between the desire for high spatial resolution and high spectral resolution. Both cannot be simultaneously satisfied leading to the development of a variety of approaches to the inevitable compromise. The approaches, in general, fall into two categories, those that make the compromise in hardware by selecting several light sources with different center wavelength [76, 77] and those that make the compromise in software using post processing algorithms and a single broadband light source [78-81]

One hardware approach uses three light sources to triangulate a peak in the absorption spectrum of a target chromophore [77]. The center wavelength of one source is chosen to coincide with the peak absortion while the other two wavelengths are chosen to coincide with low absorption regions above and below the peak. This method enables the identification of the peak in the attenuation and therefore separate attenuation due to scattering which is approximatelly linear over this range from attenuation due to absorption. Using this approach, Yang et al. [77] imaged indocyanine green in a Xenopus Laevis tadpole. A limitation of this approach is the requirement to select source wavelengths based on *a priori* knowledge of a given chromophore absorption spectrum.

More commonly, SOCT is performed in post-processing of broadband OCT data via time-frequency transform. This approach is more versatile, enabling the adaptation of the algorithm for each target chromophore in the sample. A detailed discussion of the competing algorithms is beyond the scope of this review. A discussion may be found in the literature [82] [79] [83], for the pros and cons of three commonly used methods for obtaining spectral data in SOCT, the short-time Fourier transform, the wavelet transform and the Wigner-Ville distribution.

Wax and coworkers [78] have recently developed an algorithm that incorporates two STFTs, one with a narrow spectral window and one with a broad spectral window. The two TFDs are multiplied point by point to generate a TFD with both high spatial and spectral resolution. The net result minimizes the trade-off between spectral and spatial resolution. Recently, Bosschaart, *et al,* published a quantitative comparison of short-time Fourier transforms and the dual window approach with respect to monitoring the concentration and oxygen saturation of hemoglobin [84]. In addition to the tradeoff between spatial and spectral resolution, Bosschaart, *et al*, discuss the importance of obtaining accurate spectral information when quantifying the concentration of chromophores.

2.2.2 Applications of SOCT

SOCT can gain contrast from a variety of exogenous chromophores, including the catalogue of commercially available fluorescent dyes primarily used for fluorescence microscopy. The best contrast agents possess a strongly peaked absorption spectrum in the range of the broadband source to be used. A discussion of common near infrared dyes well suited for use in SOCT can be found in the literature [85]. Gold nanoparticles have also been utilized for absorption based contrast [48, 86]. Varying the size and geometry gold nanostructure enables tuning of the peak of the absorption spectrum [87] to match the broadband source. Custom nanoparticle contrast agents have also been explored for use with true-color spectroscopic optical coherence tomography [88].

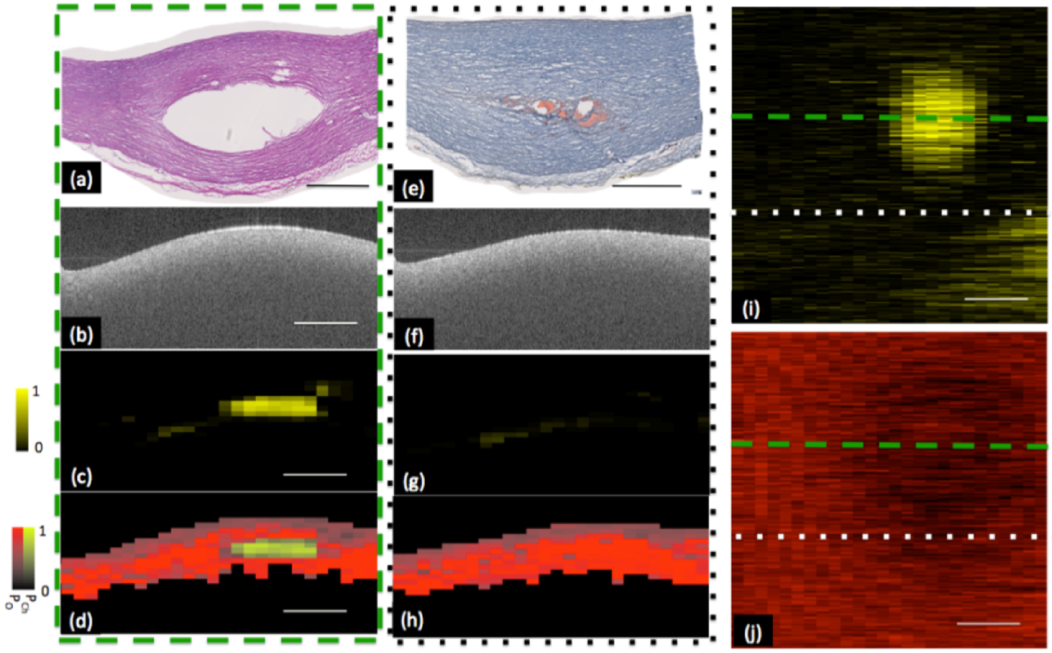

Figure 4: Representative classification of lipid plaque phantom. Two sites within volumetric data set are shown in (a-d) and (e-h). (a,e) Histology taken through two cross sections within phantom plaque, showing void created by injection of fat emulsion. Corresponding H&E and oil-red-o stains respectively showing void created by the injection of a fat emulsion within center of plaque. (b, f) Optical frequency domain imaging (OFDI) image of phantom lipid plaque corresponding to histology shown in panels a and e respectively. OFDI image shown in panel b is taken through the center of the artificial plaque whereas panel f is taken from the edge of the plaque. (c,g) Probability of cholesterol image derived from the output of the classification algorithm. A high probability of cholesterol is measured from the OFDI image taken through the center of the plaque. A low probability of cholesterol is measured through the edge of the plaque. (d, h) Classification and probability image utilizing a Hue-Saturation-Value (HSV) convention where hue encodes class (red-other, yellow- cholesterol) and saturation and value encode probability. (i) Depth resolved integration of cholesterol probability. (j) Depth resolved integration of collagen probability. Within chemograms, lipid plaque can be seen as a circular region with increased cholesterol (i) and decreased collagen probability (j). Low probability of lipid was coded as black and high probability of lipid was coded as bright yellow. Low probability of collagen was coded as black and high probability of collagen was coded as bright red. Scale bar = 1mm. Reproduced from [78].

Endogenous contrast has been widely explored for SOCT. Early work monitored the absorption due to water in the cornea through SOCT [89]. More recently, the potential for utilizing SOCT to monitor the lipid content of atherosclerotic plaques has been investigate [90]. Atherosclerotic phantoms were generated by injecting lipid pools into freshly excised porcine arteries and imaged using a 1300 nm center wavelength FD-OCT system. To obtain spectrally resolved images of the sample, short time Fourier analysis was performed on the raw OCT data. Figure 4 illustrates the system sensitivity to lipid within the sample. The authors compensate for the overlapping spectra of endogenous chromophores through preprocessing to smooth the spectra as well as statistical analysis to determine the presence of lipids [91].

The most common endogenous target for SOCT imaging has been hemoglobin [92, 93]. SOCT has been explored both as a way to map vasculature and as a way to measure blood oxygen saturation [94]. Robles and coworkers demonstrated the use of a dual window approach, noted above, along with a broadband short wavelength (455-695 nm) source for imaging blood oxygen saturation. Using a mouse window chamber model, they were able to measure oxygen saturation *in vivo*. Figure 5 depicts tissue contrast as well as SO_2 measurements in an *en face* image.

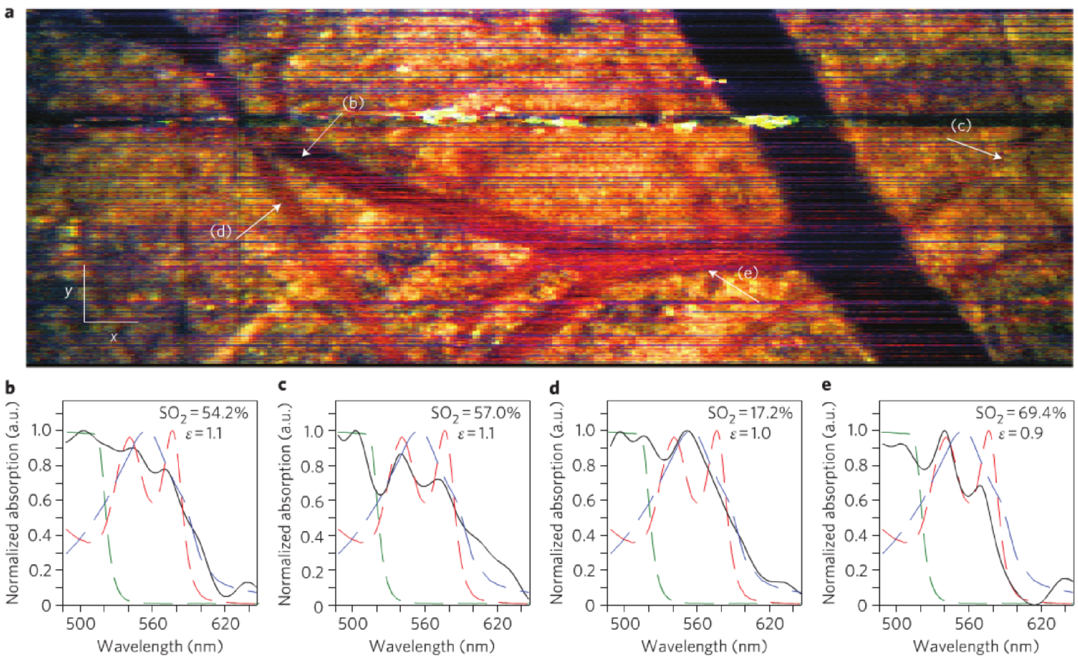

Figure 5: (a) *En face* METRiCS OCT image with arrows indicating points where the spectra are extracted. White *x* and *y* scale bars, 100 µm. (b)–(e) Spectral profiles from corresponding points in (a). Measured spectral profiles (black) are superposed with the theoretical oxy- (dashed red) and deoxy- (dashed blue) hemoglobin normalized extinction coefficients, and normalized absorption of NaFS (dashed green). Also shown are the SO_2 levels and the relative absorption of sodium Fluorescence (NaFS) with respect to total hemoglobin (Hb) ($\varepsilon \equiv$ NaFS/Hb). All spectra were selected from depths immediately below each corresponding vessel. Reprinted with permission from [49].

The development and application of SOCT is in part driven by the fact that it can largely be implemented as a post-processing algorithm. Hence, it could be widely adapted to current OCT systems including commercial devices used clinically. That being said a confounding factor is that SOCT works best when the absorption spectrum of the target chromophore(s) have a distinct peak in the wavelength band of the light source. For exogenous contrast that largely restricts SOCT imaging to near IR dyes. For endogenous chromophores the OCT system sometimes has to be adapted to the absorption spectrum of the chromophore. For instance, the blood oxygen saturation measurements highlighted above used an atypical short wavelength range OCT system in order to overlap with the distinct visible absorption peaks of oxy and deoxy hemoglobin. Such choices can have an impact on other performance metrics for the OCT system such as the imaging depth.

2.3 Magnetic Contrast Agents for OCT

2.3.1 Theory of magnetic contrast agents for OCT

Magnetomotive OCT (MMOCT) exploits induced magnetic motion to enable molecular contrast in OCT. Since human tissues have a low magnetic susceptibility, the introduction of targeted magnetic particles to tissues enables MMOCT to provide highly sensitive molecular contrast [95]. Modulated magnetic fields are generated within the sample arm of the OCT system to induce movement or spin of magnetic particles. Movement of the particles can be detected by monitoring the phase of the OCT system, whereas spin can be detected as amplitude modulations [96].

MMOCT is typically implemented in phase sensitive OCT systems through the addition of an electromagnet to the sample arm as illustrated in Figure 6. To enable frequency domain detection, a sinusoidal modulation is applied to the magnetic field. Localized heating may occur at modulation frequencies greater than 100kHz [97]. Imaging is typically imaging with modulation frequencies on the order of 10s of Hz. It has been noted in the literature that increasing the strength of the magnetic field yields diminishing returns, with high field strengths eventually resulting in saturation of the magnetic movement [98, 99].

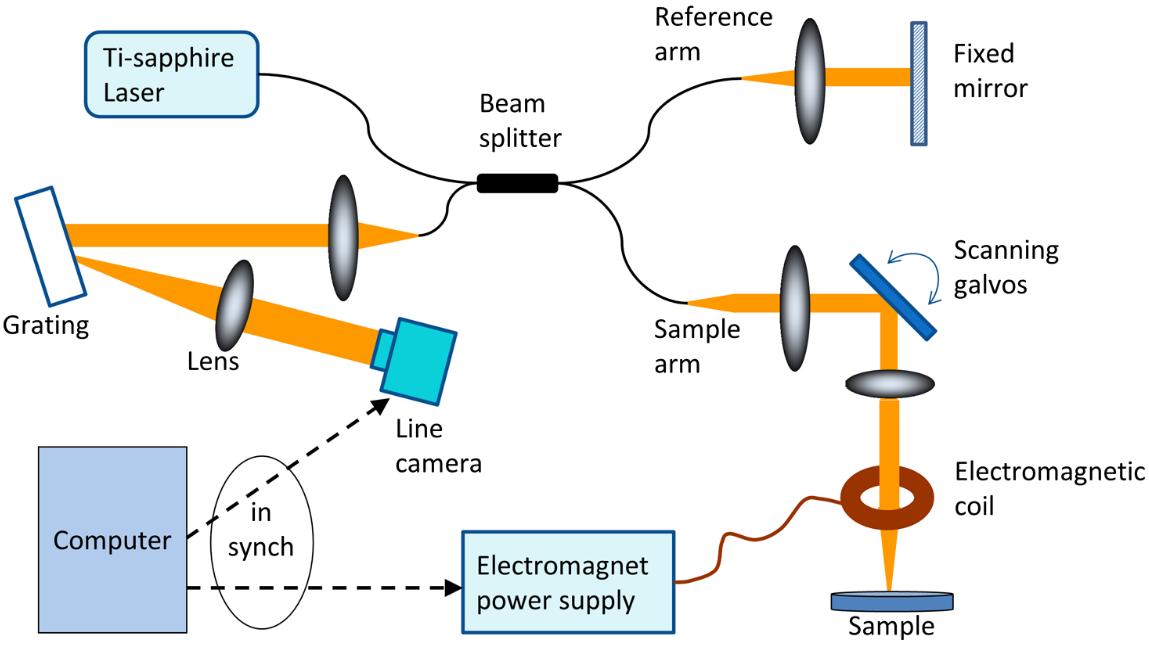

Figure 6: Biological magnetomotive optical coherence elastography (MM-OCE) setup. A standard 800 nm spectral-domain OCT system is used with an electromagnetic coil placed in the sample arm. A magnetic field strength of approximately 400Gwas used to perturb the magnetic nanoparticles (MNPs) inside the sample and changes in the magnitude and phase of the interference pattern were detected in synchrony with the A-line scan rate and activation of the magnetic field coil. Reprinted with permission from [100].

MMOCT has primarily been used to image exogenous contrast agents. Other imaging modalities, such as magnetic resonance imaging [101], x-ray luminescence tomography [102], and single photon emission computed tomography [103], have driven the development of magnetic nanoparticles which may also serve as contrast agents for MMOCT. The most prevalent of these magnetic nanoparticles are superparamagnetic iron oxides (SPIOs). SPIOs are ideal for MMOCT because they have sufficient magnetic susceptibility, proven molecular targeting, and have previously been approved by the FDA for *in vivo* contrast agents in MRI. The primary endogenous magnetic target is hemoglobin (Hb). The high concentration of hemoglobin in red blood cells enables them to serve as targets for MMOCT [104]. However, *in vivo* imaging of hemoglobin with MMOCT is confounded by the fact that the red blood cells are also moving.

2.3.2 Applications of MMOCT

MMOCT has been utilized in targeted applications of magnetic nanoparticles to detect a variety of pathologies. The potential for MMOCT to image atherosclerosis, a disease in which the arterial wall thickens due to the buildup of fats [105], has been explored through selective targeting of key molecular and cellular components. Oh *et al* demonstrated the ability to detect iron oxide nanoparticles taken up by macrophages in an atherosclerosis animal model [106]. More recently, Kim, Ahmad, and coworkers targeted magnetic nanoparticles to $\alpha_v\beta_3$, an integrin overexpressed in atherosclerosis, by functionalizing the surface of the nanoparticle with the arginine-glycine-aspartic acid (RGD) tripeptide. This technique enabled MMOCT to detect *ex vivo* atherosclerotic lesions with high specificity. Figure 7 illustrates the results of this research [107]. The same surface modification can be utilized to target cancerous tissues. In breast cancer, $\alpha_v\beta_3$ and Her_2 receptors are often overexpressed [108]. These receptors can be targeted by functionalizing the surface of magnetic nanoparticles with the RGD tripeptide [109].

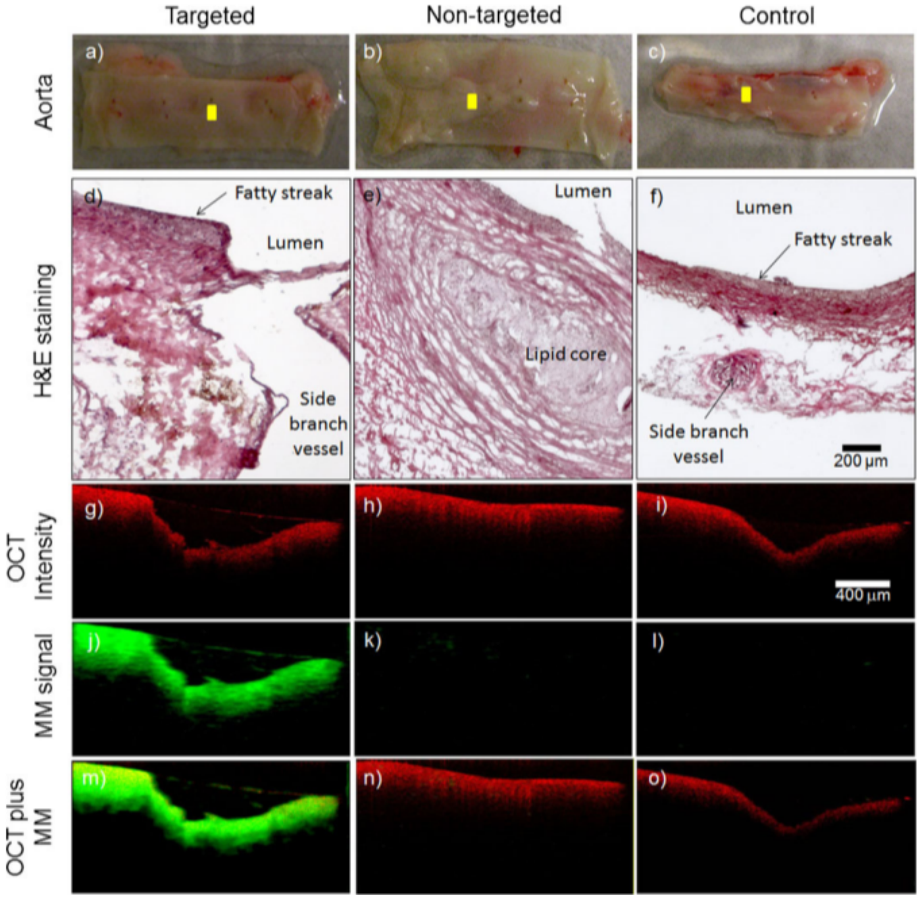

Figure 7: Biological Representative MMOCT images from the ex vivo aorta specimens. The visual appearance of the luminal walls of the aortas (a–c) and corresponding histological sections (d–f) reveal the development of early-stage fatty streaks and plaques with lipid cores. OCT structural images (g–i) were superimposed (m–o) with magnetomotive images (j–l). The cross-sectional MMOCT images correspond to the yellow scan lines shown in (a–c). The red and green channels represent the structural OCT intensity and MMOCT signal, respectively. Reprinted with permission from [107].

As a substitute for targeting magnetic nanoparticles to specific cells or molecular signals, cells may be tagged *in vitro* then introduced to a living sample. Two previous studies performed by Oldenburg *et al* have demonstrated the capability to image magnetically tagged platelets, small cell fragments involved in the wound healing process, using MMOCT. Dextran coated SPIOs were uptaken by platelets and introduced into both *in vitro* and *ex vivo* samples to track the location of injured vasculature [99, 100]. When contacting activating factors, such as collagen, platelets will aggregate at a region of injury, initiating the clotting of blood [111]. Figure 8 depicts the aggregation of SPIO tagged platelets at the site of an injury in vasculature [110].

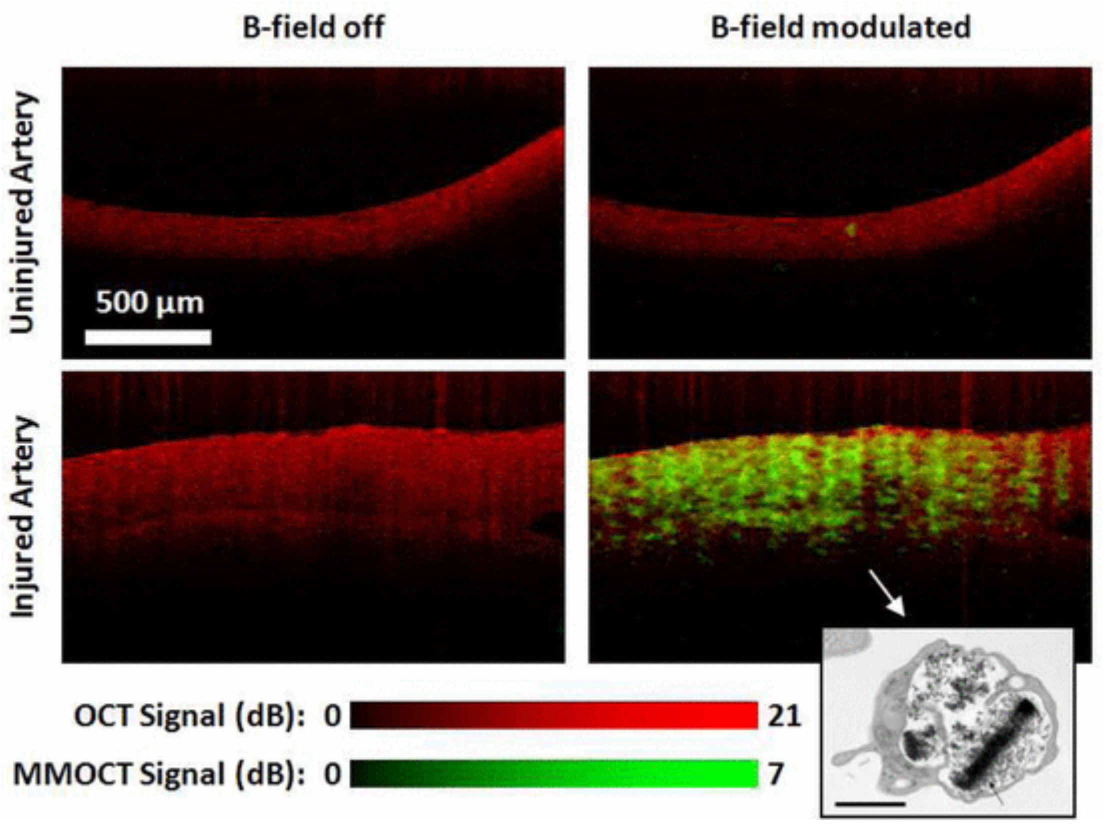

Figure 8: OCT (red) and MMOCT (green) of ex vivo porcine arteries exposed to SPIO loaded rehydrated lyophilized (SPIO-RL)platelets in a flow chamber. MMOCT contrast is specific to the artery that was injured, due to specific adhesion of SPIO-RL platelets. Lower right inset: TEM of an SPIO-RL platelet, 1 µm scalebar. Reprinted with permission from [110].

The fact that there exists FDA approved SPIOs means that MMOCT could make it to clinical application with off-label use of the SPIOs even with only very limited clinical applications. An additional advantage is that much of the labeling chemistry has been worked out such that SPIOs can readily be target to key indicators of pathologies such as cancer and atherosclerosis. Outside of molecular contrast, MMOCT has been shown to potentially be useful for enhancing signal in optical coherence elastography [100] [112].

2.4 Second Harmonic OCT

2.4.1 Theory of second harmonic OCT

Second harmonic optical coherence tomography (SHOCT) provides OCT with contrast via the non-linear process of second-harmonic generation (SHG). SHG fundamentally refers to the phenomena where two photons simultaneously interact with a noncentro-symmetric material and combine to generate a single photon with twice the frequency (half the wavelength) [113]. Second harmonic generation is a coherent process, hence directly detectable using low coherence interferometry.

SHOCT requires the use of a femtosecond laser source due to the fact that the second harmonic signal is inversely proportional to the pulse duration of the light source. As a consequence SHOCT is only compatible with spectrometer based OCT or time-domain OCT, i.e. it is incompatible with swept-source techniques. A second requirement is a nonlinear medium, typically a nonlinear crystal, in the reference arm to generate the second harmonic reference signal. Otherwise, the SHOCT optical system can take on any geometry normally used for OCT. Figure 9 illustrates a typical setup of a SHOCT system. Two spectrometers are necessary in order to collect the backscattered near IR (fundamental) light as well as the visible (second harmonic) light. Depth resolution occurs in the same way as for standard OCT except the SHOCT signal is only generated in the tissue where there is noncentro-symmetric media, typically collagen. A SHOCT system is usually setup to have better lateral resolution than a typical OCT system because there is an added benefit to the second harmonic signal strength which is proportional to the square of the fundamental light intensity.

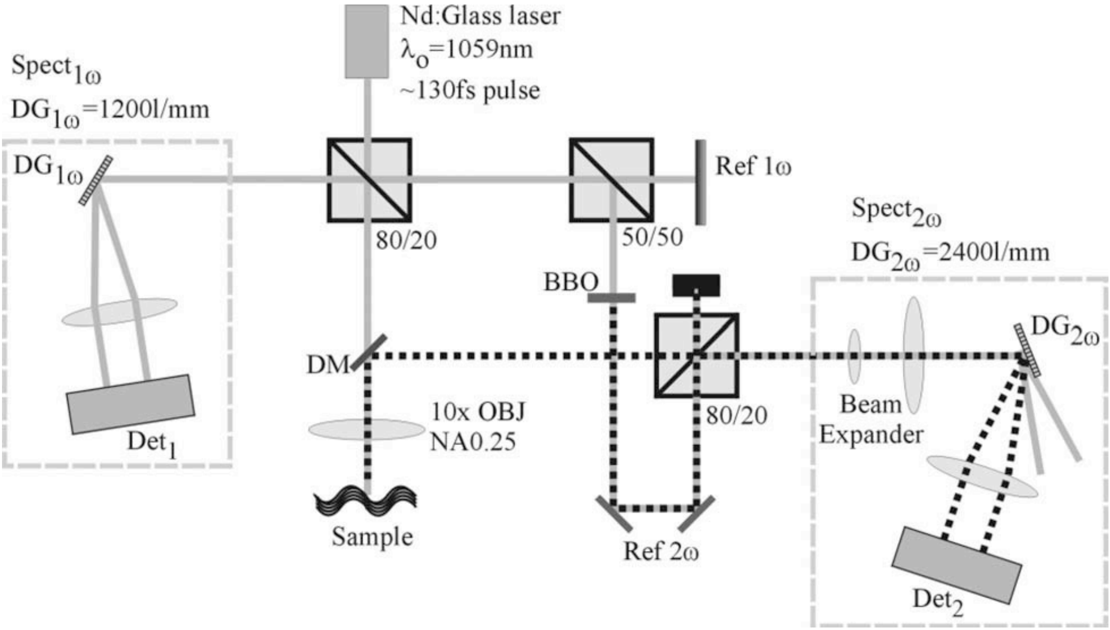

Figure 9: Schematic of the SD SH-OCT layout. The solid gray line represents the fundamental beam path, and the dotted black line represents the beam path for the secondharmonic light. Spectnω , spectrometer designed for the nth harmonic; DG, diffraction grating; Det, detector; OBJ, objective; NA, numerical aperture. Reproduced from [114].

2.4.2 Applications of second harmonic OCT

As noted above the most efficient second harmonic source in biological systems is collagen. The triple helical structure of collagen provides the necessary noncentro-symmetric geometry necessary for SHG [115, 116]. Collagen has been the target from the earliest example of SHOCT imaging in tissue [117]. An example SHOCT image [118] of rat tail tendon is show in Figure 10(a). Many of the morphological structures that are responsible for the mechanical properties of the tendon can be seen in the image, which correlate well with the structures seen in the polarization microscopy image in Figure 10(b).

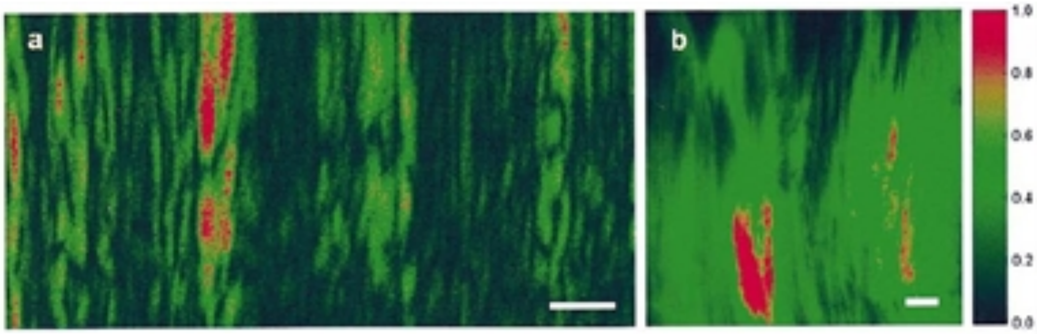

Figure 10: (a) SH-OCT image showing an area of 100 × 50 μm in the rat-tail tendon, where many cable-like, parallel oriented, and slightly wavy collagen fiber bundles (fascicles) can be visualized; (b) 60X polarization microscope image of the same sample (scale bar: 10 μm). Reproduced with permission from [118].

Additional information may be extracted from SHOCT by measuring the polarization dependence of the SHOCT signal. This dependence can be quantified with the anisotropy parameter, $\beta = (I_{\parallel} - I_{\perp})/(I_{\parallel} + 2I_{\perp})$, where $I_{\parallel}$ and $I_{\perp}$are respectively the intensity of parallel and perpendicular linear polarization second harmonic signals emitted from the sample. The anisotropy parameter should vary depending on the relative orientation of the collagen fibrils. Applegate et al. [119] demonstrated the first polarization resolved imaging on a sample of salmon skin shown in Figure 11. Depending on the polarization state, the SHG signal varied across the sample, Figure 11(a) and (b). Vector addition of the signals from the two polarization states lead to the polarization independent image shown in Figure 11(c). Finally, Figure 11(d) is a map of the anisotropy parameter indicating the relative orientation of the collagen fibrils.

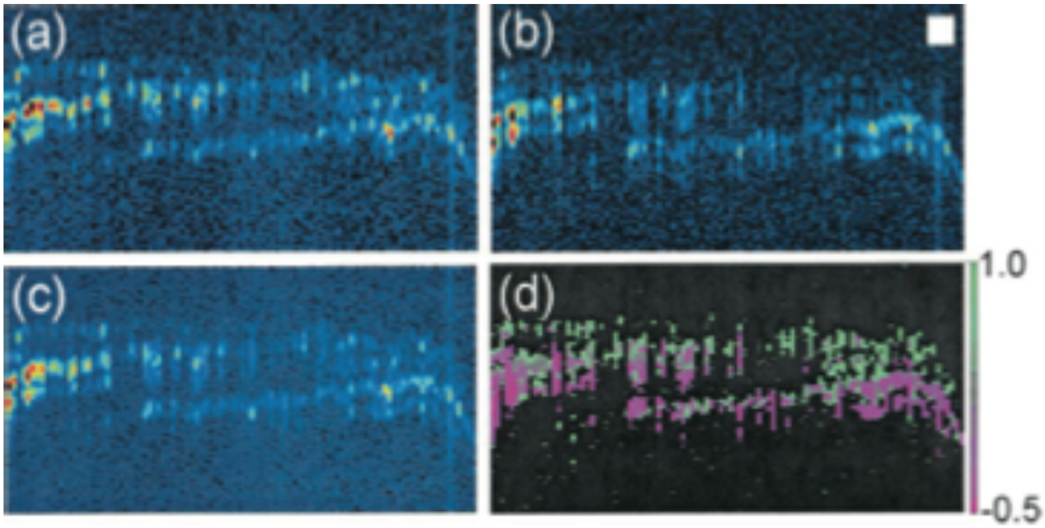

Figure 11: (a) SHOCT image of the overlap of three fish scales, recorded with the reference-arm second-harmonic light polarization parallel to the fundamental light polarization. (b) SHOCT image recorded with the reference-arm second-harmonic light polarization perpendicular to the fundamental light polarization. (c) Polarization-independent image derived from (a) and (b). (d) Image of the anisotropy parameter, β. Reprinted from [119].

Currently, SHOCT is somewhat limited by the prevalent forward scattering of SHG light from collagen. The forward scattered light may be backscattered by a deeper reflector in the sample, confounding localization of the collagen which generated the second harmonic signal. To the best of our knowledge, no exogenous SHG agent has been demonstrated in the literature for SHOCT, further limiting its application.

2.5 Optical Multimodality Imaging with OCT

2.5.1 Background

Thus far we have focused on reviewing imaging technologies that somehow derive molecular information from the OCT signal. A second path to the desired end result, an imaging technology that can effectively probe both morphological and biochemical pathological changes in tissue, is to combine modalities. In many cases, individual optical imaging modalities have demonstrated promising results for differentiating between healthy and diseased tissues and cells. However, the complex, pathological mechanisms of disease progression limit the diagnostic accuracy using individual modalities. Combining two or more optical imaging modalities to provide different optical responses of biological samples improves the accuracy, sensitivity and specificity for early diagnosis. In general, the optical multimodality imaging is constructed by combining morphological and functional imaging modalities. As OCT is an excellent morphological imaging modality, a variety of research combining OCT and functional imaging modalities such as steady-state fluorescence spectroscopy [121-123], time-resolved fluorescence lifetime imaging microscopy (FLIM) [120, 121], florescence laminar optical tomography [126, 126] and Raman spectroscopy [127, 128] have been studied for acquiring complementary optical responses of biological samples.

A multimodality imaging system combining OCT with other functional imaging modalities is typically constructed by partially or fully combining optical and mechanical parts, light sources and data acquisition. Figure 12 is an example of a multimodal system that combines OCT and FLIM by using a common set of imaging optics, but otherwise remains two distinct imaging systems.

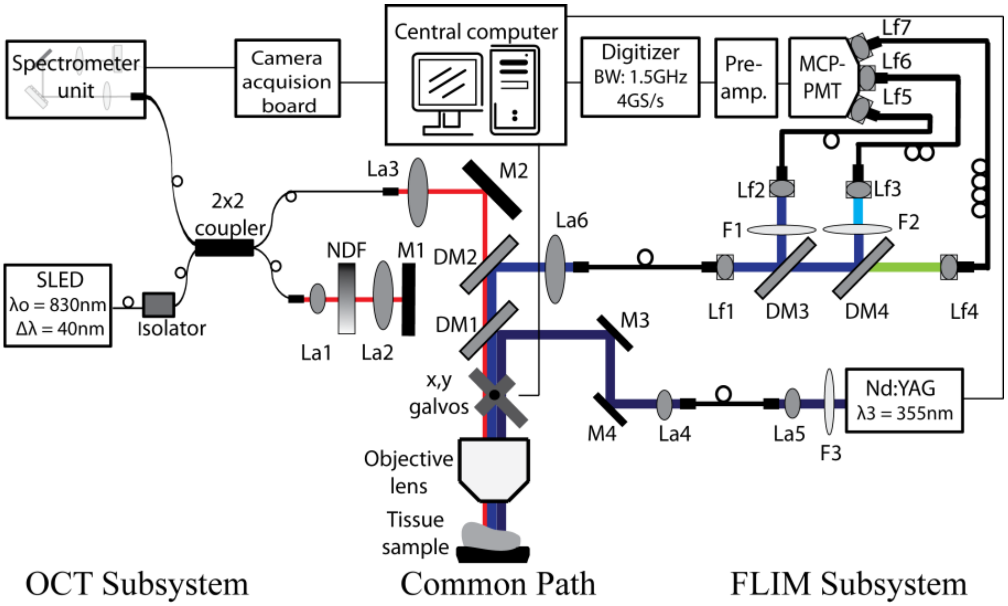

Figure 12: Schematic diagram of the multimodality imaging system by combining OCT and FLIM subsystems. L1, L2 and L5: free-space collimation and coupling lenses, L3, L4, L6-L12: fiber-connected collimation and coupling lenses, NDF: neutral density filter, M1-M4: mirrors, DM1-DM4: dichroic mirrors, and F1-F4: filters. Reprinted with permission from [123].

2.5.2 Applications of optical multimodality imaging with OCT

A Fluorescence is widely used as a method of identifying molecular species. The unique fluorescent characteristics of endogenous (e.g. collagen, elastin and NADH) and exogenous (e.g. luciferase, indocyanine green and fluorescein) fluorophores have been measured by steady-state (intensity) and/or time-resolved (lifetime) fluorescence.

Changes in characteristic fluorescence with the onset of pathological changes in tissues have been investigated for diagnosing and monitoring various diseases.

Simultaneous measurement of morphological and biochemical information by combining OCT and different fluorescence detection modalities increase the sensitivity and specificity for detecting cancers [120-122] and atherosclerotic plaques [124]. Barton et al. developed a multimodality imaging system by combining OCT and steady-state laser-induced fluorescence (LIF) spectroscopy for diagnosis of ovarian [121] and colon [122] cancers, and designed an OCT/LIF miniature endoscope for animal and clinical studies [123]. Figure 13 demonstrates OCT images and corresponding histology of solid sex cord-stromal tumors (SCST) (a-d) and LIF spectral comparison of all experimental groups (f) with murine ovarian model. They reported that OCT images of solid SCST shows rapid attenuating homogeneous masses and large vascular spaces adjacent to neoplastic masses compared to control tissues. In LIF spectra, 390nm peak is greater than 450nm peak due to high collagen content from thin collagenous capsule and decrease NADH content with slowly proliferating neoplasm with sensitivity of 88% to SCST and specificity of 60% to normal cycling ovaries [121].

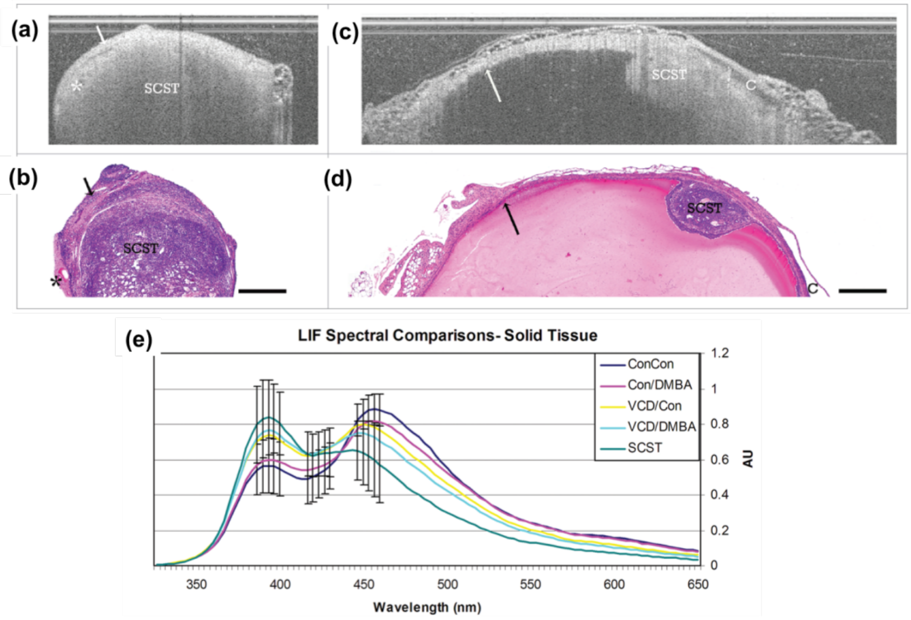

Figure 13: Solid SCST and Life spectral curves. (a) and (b) OCT image of ovary with solid SCST and corresponding histology. (c) and (d) OCT image of solid SCST within benign and corresponding histology. (e) Solid spectral curves. SCST: sex cord-stromal tumor, arrow: benign cyst lining, asterisk: vascular spaces, C: adjacent benign cyst, Scale bar: 500 μm, Con: Control, VCD: 4-vinylcyclohexene diepoxide, DMBA:7,12-dimethylbenz[a]anthracene, Grouping (IP injection/Ovarian injection). Reprinted with permission from [120].

A multimodality OCT/FLIM system was developed to simultaneously acquire co-registered OCT and autofluorescence FLIM images for detection of oral cancer using *in vivo* hamster model [120] and atherosclerotic plaque using ex-vivo human coronary arteries [124]. Compared to the steady-state LIF system providing fluorescence intensity only, FLIM can provide fluorescence intensity as well as lifetime as a function of wavelength. The advantage of using lifetime information over intensity is that it is more stable in the experimental environment including motion artifact of samples and variation of excitation pulse energy, which is a critical factor for clinical measurement. Figure 14 shows a volumetric (a) and cross-sectional (b) OCT structure images of a squamous cell carcinoma (SCC) area in an *in vivo* hamster check pouch, a related histopathology (c) and en-face fluorescence intensity and lifetime images at three target wavelength channels (d). The SCC tumor was significantly thicker (~1mm) than normal oral mucosa (~0.4 mm) and lost the layered structures, as shown in the OCT volume. The fluorescence intensity and lifetime of malignant tissue followed the characteristics of both NADH and FAD, suggesting the autofluorescence emission of malignant tissue [120].

Another optical multimodality imaging technique is to combine OCT and fluorescence laminar optical tomography (FLOT) to simultaneously acquire morphological and molecular information from a biological sample with a depth resolution of a couple millimeters. FLOT uses a photodetector array to detect back-scattered light away from a scanning spot with different pathways. A depth-resolved image is reconstructed from the detected signals utilizing a mathematical algorithm such as a radiative transport equation based on a Monte-Carlo simulation [125, 126].

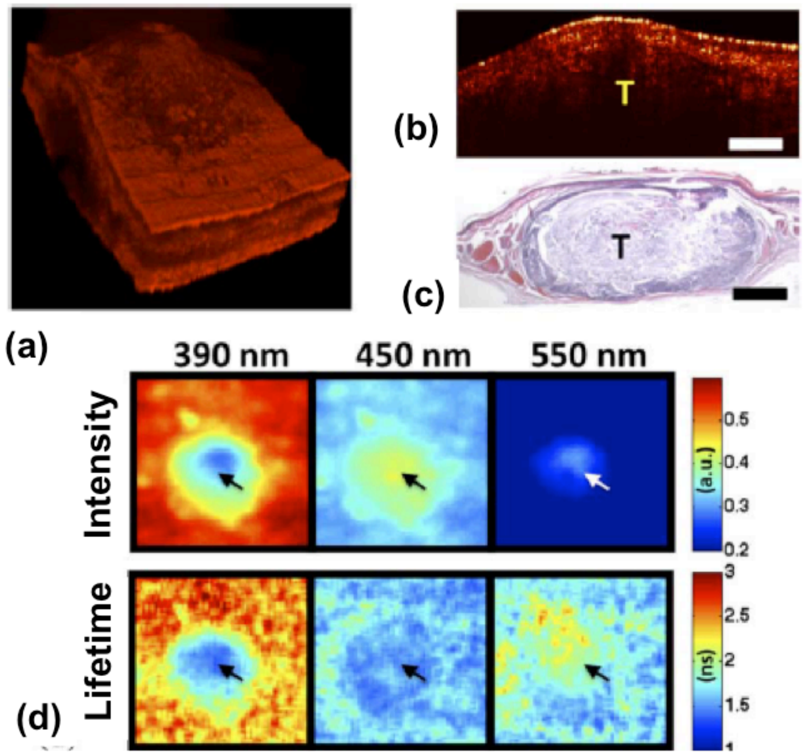

Figure 14: In-vivo co-registered OCT and FLIM images of SCC with hamster check pouch model. (a) OCT 3-D volume shows a thick middle region surrounded by thinner tissue. (b) and (c) sample OCT cross-sectional image and corresponding histology. (d) FLIM images showed two distinct regions: a center area with a fluorescence that is characteristic of nicotinamide adenine dinucleotide (NADH) and flavin adenine dinucleotide (FAD), and a surrounding area with an emission that is characteristic of collagen. Tumor area (tumor (T), scale bar = 300 μm, and field of view: 2 x 2 mm^2). Reprinted with permission from [120].

Figure 14 shows OCT/FLOT images of a human breast cancer xenograft model *in vivo*. In the OCT image (a), the layers of skin are not clear due to the similar scattering, but the boundary between the skin and tumor is clearly visible. The co-registered FLOT image (b) indicates the subcutaneous tumor. The fused OCT/FLOT image (c) demonstrates the position, distribution and size of the tumor located underneath skin, and is confirmed with corresponding histology (d) [126].

The combination of OCT and Raman spectroscopy (RS) is also capable of providing structural and molecular information from complex tissue samples. Despite the long integration times ranging from approximately 3 to 30 seconds and low quality structural information, near-infrared RS techniques have the advantage of high molecular specificity which can be an asset for detecting cancers [127, 128]. The combination with OCT can compensate for some of the drawbacks by providing optical sectioned tomographic images with micron scale resolution. Figure 15 displays an OCT cross-sectional image of ex vivo malignant human breast tissue using an OCT/RS system. Normal and abnormal regions with high-density scattering signals were noted in the OCT cross-sectional image of Figure 15(a). Using the OCT as a guide, RS signal was collected from the areas of interest. Figure 15(b) shows the Raman spectra from the two areas identified as normal and malignant. The Raman spectrum of the normal area was dominated by signals consistent with the presence of lipids. However, the malignant region had showed a higher contribution from DNA and proteins, especially collagen [127].

Development of multimodal OCT systems can clearly profit by tapping into the wealth of research that has gone into the modality that it is being paired with. In the case of fluorescence and Raman spectroscopy there has been considerable research related to cancer diagnosis [129, 130]. Nevertheless, the ensuing technology tends to be much more complex and requires compromises related to the typical mismatch between imaging speed, resolution, and/or dimensionality of the image (e.g. 2-D v. 3-D).

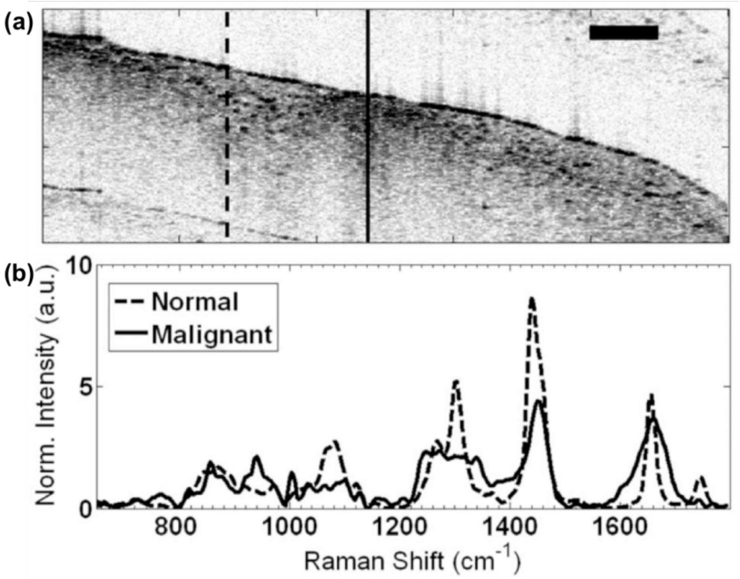

Figure 15: OCT Image and Raman shift of ex-vivo malignant human breast tissue from OCT/RS system. (a) OCT cross-sectional image, normal region of tissue (solid line), malignant region of tissue (dashed line) (b) Intensity of Raman shift signal from the (a), scalebar = 500 µm. Reprinted with permission from [127].

2.6 Pump-Probe OCT

2.6.1 Theory of pump-probe OCT

Pump-Probe optical coherence tomography (PPOCT) integrates OCT with the pump-probe spectroscopy to provide molecular contrast. The pump-probe technique has been widely employed in experimental molecular physics to measure excited electronic states and molecular dynamics. Nominally, in pump-probe spectroscopy, when a molecule absorbs the energy of a pump photon, an electron is promoted into an excited state. The measurements of subsequent probe photon interactions with the molecule reveals how the excited state evolves over time. Both the intensity of the pump-probe interaction and the time evolution of the signal measured by varying the delay between the pump and the probe are unique molecular properties that may be used to distinguish among different molecules. In practice, given the complexity of both the molecules of interest and their tissue environment it is unlikely that the simple mechanism noted above can hold in its entirety. Fundamentally, any mechanism that leads to a change in the probe intensity after interaction with the pump will generate PPOCT signal.

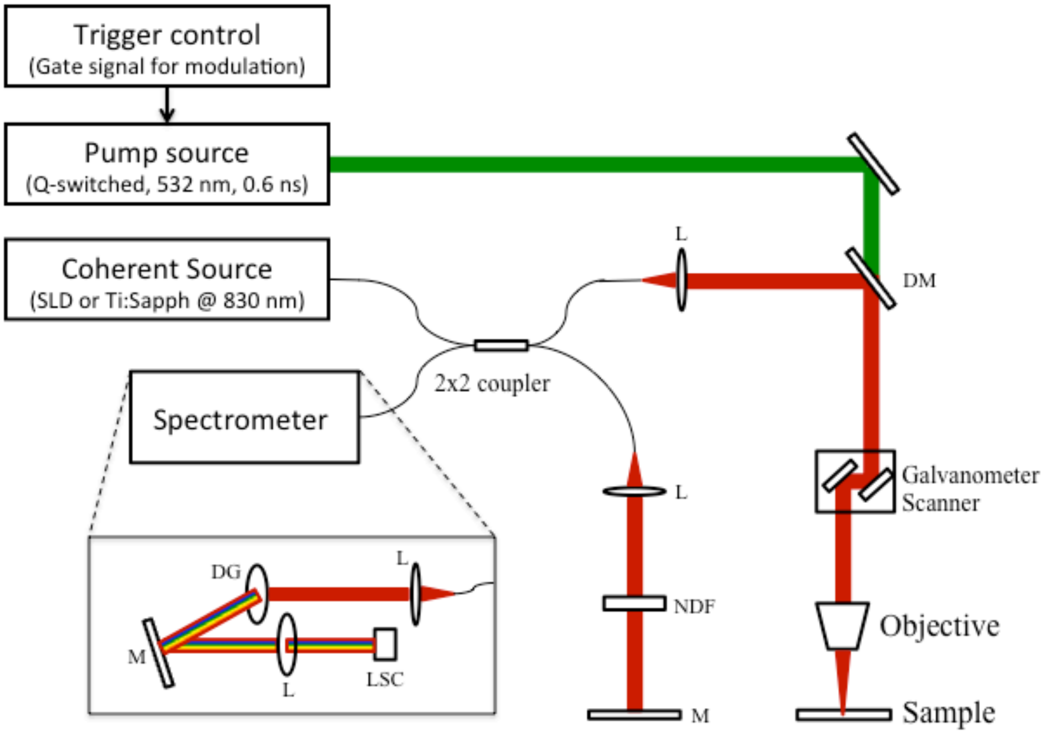

Figure 16: A schematic diagram of PPOCT. Pump light source: Q-switched 532nm laser, Probe light source: SLD or Ti:Sapphire laser at 830nm center wavelength, L: lens, NDF: neutral density filter, DM: dichroic mirror, M: mirror, DG: diffraction grating, LSC: line-scanning camera. Reprinted from [131].

PPOCT may be accomplished by integrating a pump laser into the sample arm of an existing OCT system. The light source for the OCT system may then serve as the probe beam. The pump source needs to be selected based upon the molecular properties of the target molecule. The co-propagating pump and probe beams excite the sample. A typical setup for PPOCT is shown in Figure 16. By modulating the pump beam with frequency, f_m, the pump-probe interaction can be monitored by scanning the sample over time. The frequency response of a time domain PPOCT system can be expressed as the carrier frequency of the reference arm plus or minus f_m [91] . In a spectral-domain OCT system, the pump-probe signal can be filtered out from an OCT M-scan (line images measured as a function of time instead of space). The PPOCT signal from spectral domain OCT may be extracted at the f_m following a Fourier transform along the time axis of an M-scan. A flow chart of this process is shown in Figure 17.

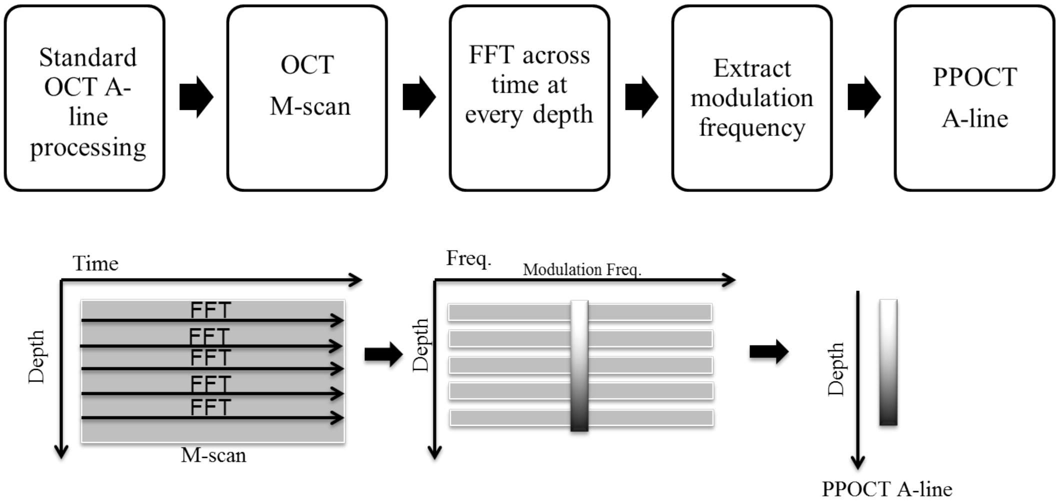

Figure 17: Flowchart of data collection and processing of PPOCT. An M-scan of OCT is collected and a Fourier transform is taken at every depth. The modulation frequency is extracted at each depth to compile the PPOCT A-line.

2.6.2 Applications of pump-probe OCT

In principle, any molecule that absorbs light can be used as an exogenous contrast agent for PPOCT, including fluorescent dyes and proteins. Indocyanine green [133], dsRed [132], and methylene blue [134] have all been shown to provide contrast via PPOCT. In the initial PPOCT experiments, Rao and coworkers [134] demonstrated the ability to monitor the pump-probe interactions of methylene blue using a 532 nm pump and 800 nm probe. Following up this work, Applegate *et al.* [131] developed a degenerate PPOCT system with a pump and probe at 532 nm and used it to image the distribution of the fluorescent protein dsRed in the skeletal muscle of transgenic zebrafish. Some results from this study are shown in Figure 18. Images were recorded from two areas of the zebrafish indicated by the boxes in Fig 18(a). OCT images and overlays of the PPOCT onto the OCT images are shown in Figure 18(b), (c), (e), and (f). Figure 18(d) and (g) show the overlay of the derivative of the PPOCT signal onto the OCT image. The derivative was calculated to take into account the fact that light absorption is integrated in depth, in other words light can be absorbed along the entire path the light travels, not just where the light is backscattered.

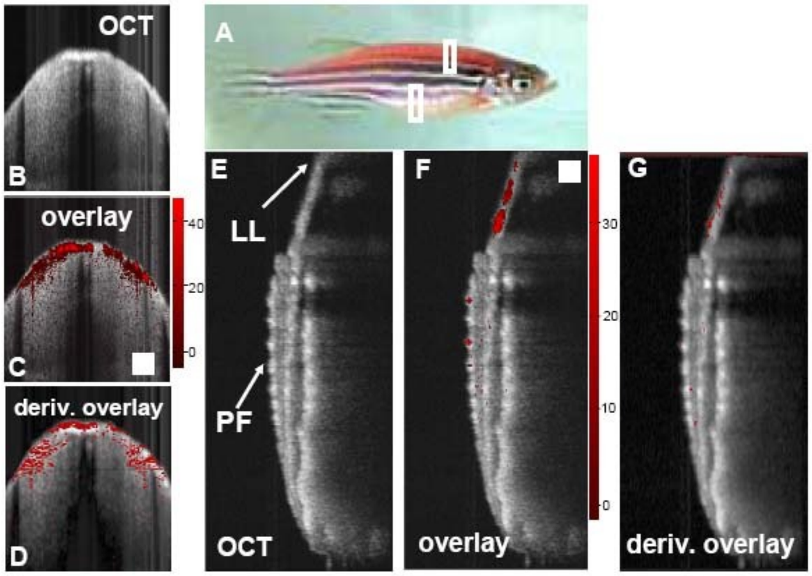

Figure 18: A) Photo of transgenic zebra danio fish expressing dsRed in its skeletal muscle. B) OCT cross-section recorded through the back of the fish, anterior to the dorsal fin as indicated by the top white box in the photo. C) Overlay of the corresponding ground state recovery PPOCT (gsrPPOCT) image onto the OCT image in B. The color bar indicates the SNR of the gsrPPOCT signal (max 47 dB). D) Derivative image derived from panel C. E, F, G) Same as B, C, and D except recorded along a cross-section (bottom white box) bisecting the pectoral fin (PF) and continuing into the lateral line (LL). The maximum recorded SNR gsrPPOCT in panel E was 37 dB. The scale box is 200 μm×200 μm. Reprinted from [132]

Several endogenous chromophores have also been probed with PPOCT. Previous studies have demonstrated melanin [135, 136], Phytochrome A [137], and hemoglobin [131] imaging via PPOCT.

3. DEVELOPMENT OF PPOCT SYSTEM[*]

This chapter describes the design and development of the PPOCT system, and provides experimental *ex/in vivo* results. As an initial test, performance of PPOCT system was demonstrated with a capillary tube model as detailed in the section of Results. Also, the PPOCT system was validated for its ability to acquire morphology and molecular contrast-enhanced signal from endogenous (Hb) or exogenous (MB) agent simultaneously from the experiments on the live animal.

3.1 Imaging in Xenopus laevis

3.1.1 Method

The schematic of the two-color Fourier-domain PPOCT system is illustrated in Figure 16. Two different near-infrared sources were utilized as the probe/ OCT beam. The first was a tunable 140fs Ti:Sapphire laser operated at 830nm. The Ti:Sapphire was spectrally broadened to ~200 nm bandwidth. The SLD with a center wavelength of 830 nm and a bandwidth of 40 nm was utilized as the second probe source. The SLD allowed for greater power on the sample and offered better intensity stability than the Ti:Sapphire. The powers of the pump and probe sources are stated for each individual experiment be- low. The probe source was launched into a 2×2 (50:50) fiber coupler.

---

[*] Reprinted with permission from [131] Carrasco- Zevallos, Oscar, Ryan L. Shelton, Wihan Kim, Jeremy Pearson, and Brian E. Applegate. "In vivo pump- probe optical coherence tomography imaging in Xenopus laevis." Journal of biophotonics 8, no. 1-2 (2015): 25-35
[138] Kim, Wihan, and Brian E. Applegate. "In vivo molecular contrast OCT imaging of methylene blue." Optics letters 40, no. 7 (2015): 1426-1429.

Galvanometer mirrors were used to laterally scan the OCT beam over the sample, while a mirror positioned in the referenced arm completed the Michelson interferometer. The pump source consisted of an actively Q-switched Nd:YVO4 laser, frequency doubled to 532 with a maximum pulse repetition rate of 100 kHz. Co-propagation of pump and probe beams at the sample was achieved using a dichroic mirror. A custom spectrometer employing a linescan camera with a maximum line rate of 53 kHz completed the FD-OCT system.

When precise control of interpulse delay was required, the Ti:Sapphire was utilized as the probe and the Q-switched pump was triggered by a sync pulse from the Ti:Sapphire pulse picker, which enabled temporal synchronization of both lasers. The sync pulse was passed through a digital delay generator (Hiland Technology, P-400) to allow control of the interpulse delay. The sync pulse of the Ti:Sapphire was also used to trigger the linescan camera to capture the back-reflected spectra. A camera integration time of 20 ms was used, which limited the repetition rate to 40 kHz. In order to encode the transient absorption into the OCT signal, a 15 kHz square wave modulation was used to time-gate the Q-switch output and amplitude modulate the pump source. Conventional OCT processing methods were utilized to acquire an OCT M-scan. The pump-modulated PPOCT information was extracted by performing a Fourier transform of the M-scan along the time dimension and subsequently filtering around the modulation frequency at each depth, yielding a PPOCT A-line. Therefore, an OCT M-scan corresponds to a PPOCT A-line. Similarly, a PPOCT B-scan can be obtained from a 2-D OCT M-scan. This processing technique is outlined in more detail in [135].

The imaging speed of the system is governed by the OCT line rate and the number of OCT A-lines (M-scan) used to produce a PPOCT A-line. Due to the PPOCT processing algorithm, reducing the number of OCT A-lines yields faster PPOCT imaging rates, but reduces PPOCT SNR. The number of OCT A-lines used to generate each PPOCT A-line in Figures 4 and 5 was 300 resulting in an effective line rate of 133 Hz. For Figures 3 and 6, 100 a-lines were used for an effective line rate of 400 Hz. Previous work characterized the speed and SNR relationship of a similar Fourier-domain PPOCT system [135].

Pump power also contributes to PPOCT SNR. While higher pump power could be used to achieve better signal quality, the safety of the specimen being imaged needs to be taken into account. For the in vivo experiments in this study, the surface fluence was kept below the ANSI safety limits for skin.

Finally, we should note that PPOCT inherently measures the attenuation of light due to absorption. Absorption of light is integratived over its path- length, hence the PPOCT signal is inherently dependent on the pathlength through the sample. Similarly, since the attenuation is reported by light that is back-reflected from the sample, the signal is dependent on the sample reflectivity and the location in the sample where it was reflected. [139] In other words, probe light incident on the sample that passes through the chromophore will be attenuated and modulated by the pump interaction with the chromophore. This light can be back-reflected at the chromophore or somewhere deeper. The light reflected at the chromophore accurately reports the attenuation and position of the chromophore. However, light reflected deeper than the chromophore accurately reports the attenuation, but not the chromophores location. This effect will be obvious in the images of capillary tubes shown below (Figure 20) where a PPOCT signal is observed at the bottom surface of the capillary tube but not the top. As we have discussed previously [132] this ambiguity may be lifted by normalizing to the reflectivity measured in the OCT image and calculating the derivative after smoothing to reduce speckle.

For the images shown below, we have not taken this additional processing step. Blood is a strong absorber and scatterer, hence the majority of the PPOCT signal is at the position of the blood vessel. In our previous work with imaging blood we only noted a modest improvement by calculating the derivative image but with a substantial sacrifice of resolution.

3.1.2 Results

3.1.2.1 PPOCT system characterization

We have investigated the lifetime characteristics of the PPOCT signal from both MB and hemoglobin with a 532 nm pump and an 830 nm probe. MB serves as an archetypal molecule where the photo- physics are well known. Hemoglobin, on the other hand, is a complex heme protein with photophysics that are not well understood. This leads to some ambiguity in the origin of the hemoglobin PPOCT signal.

The performance of the system was evaluated by measuring the PPOCT signal from a 0.05% solution of MB between two coverslips. The average power of the pump and probe beams were 17 mW and 160 mW (100 kHz repetition rate), respectively. Recording the PPOCT signal as a function of the pump-probe interpulse delay enabled the measurement of the triplet state dynamics. The strongest PPOCT signal arises from the top surface of the bot- tom coverslip with this sample. The peak of that signal is plotted as a function of interpulse delay in Figure 19(A) while Figure 19(B) depicts the pump-probe process exploited for MB PPOCT imaging.

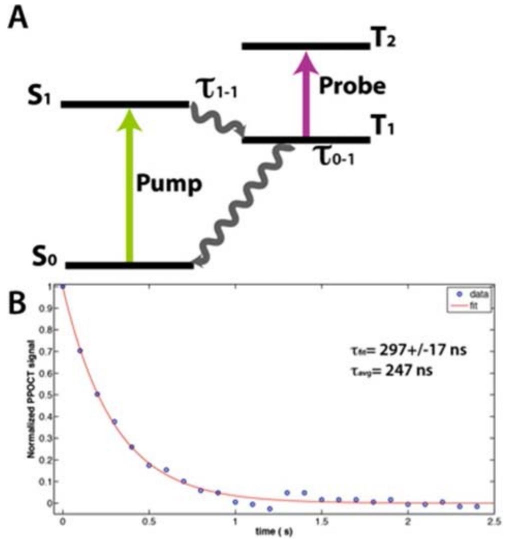

Figure 19: (A) Molecular energy level diagram for the methylene blue PPOCT mechanism. Driven transitions are indicated by straight arrows and spontaneous transitions as wavy arrows. (B) Measured normalized decay (blue cir- cles) and exponential fit of the PPOCT signal due to methylene blue as a function of delay between the pump and probe pulse. The decay has a fit lifetime of 297 ns and a characteristic average lifetime of 247 ns.

The resulting temporal decay was fit to a single exponential curve. The inverse of the decay constant is the lifetime of the T1 state or τ_{0-1} assuming the intersystem crossing is very fast and τ_{1-1} is therefore negligible. A lifetime of 297 ± 17 ns was measured, where the quoted error is the 95% confidence interval from a fit of 25 data points collected at 100 ns intervals. The MB triplet state is readily quenched by oxygen, hence the exact lifetime is a function of the oxygen level in the MB solution and varies from less than 0.3 us to 79.5 us [140]. A highly oxygenated state is expected since no effort was made to deoxygenate the solution. However, the measured lifetime is lower than one would expect given a MB solution stored in air and likely contains some contribution from photobleaching. Nevertheless, this result demonstrates the system's ability to measure the temporal decay of the pump-probe signal with increasing interpulse delay.

The average lifetime ($\tau_{avg} = \sum s \cdot t / \sum s$) is much faster and easier to calculate than an exponential fit. Moreover, it is more reliable for noisy data. The calculated average lifetime for the decay in Figure 19(B) is 247 ns, somewhat lower than given by the fit, but still reasonable. The average lifetime is more practical for high-speed imaging and may prove useful in the future for differentiating chromophores based on their lifetime characteristics.

Since 532 nm and 830 nm pump-probe imaging of Hb has not previously been demonstrated, we sought to characterize the lifetime dynamics of the Hb signal for the first time. Time resolving the PPOCT signal from Hb yielded a somewhat unexpected result. While there is clearly a variation in the Hb signal on the time scale of the 15 kHz modulation (66 us) there was no apparent change in the signal when we varied the delay over the entire 25 us period (40 kHz) between pulses. Given the fairly strong intensity noise due to spectral broadening of the Ti:Sapphire pulses in the single mode fiber, we would estimate the accuracy of our measurement to $\pm 5\%$. Nevertheless, that would seem to indicate that we are exciting the Hb into some long- lived state. A literature search yielded two mechanisms that would explain our observations. The first is that photo-initiated oxidation of þ Fe^{+2} into Fe^{+3} in the heme protein via the 532 nm pump results in the formation of methemoglobin (metHb) [141]. MetHb has a factor of 2–3 larger absorption coefficient than oxy- and deoxy-Hb in the NIR [142]. Since metHb is only slowly enzymatically [143] converted back to Hb, each time the pump interacts with the blood sample the concentration of metHb increases stepwise. The frequency spectrum of a stepwise increasing function has a strong component at the step frequency, hence modulation of the pump intensity leads to a modulation in the nearIR absorption that would be observed in the probe.

The second mechanism involves the population of high lying vibrational states in the ground state of oxy- and deoxy-Hb which will effectively red-shift the absorption spectrum [144] leading to a relative change in the nearIR absorption. The high lying vibrational states are populated via internal conversion of the excited electronic state which has been populated by the 532 nm radiation. This creates “hot bands” in the hemoglobin spectrum that leads to the red-shift. This can be thought of as local heating which shifts the Boltzmann distribution thereby populating higher vibrational states in the ground electronic state. The net result is that a modulation of the pump power leads to a modulation in the nearIR absorption that would be observed in the probe and have a long lifetime.

It seems likely given the results in the literature that both mechanisms play some role. Our current hypothesis is that the first mechanism (metHb) is more important at high power and long dwell times and the second mechanism is more important at lower powers and short dwell times. This hypothesis is based in part on our observation of the formation of solids in capillary flow tubes with high pump powers and with low pump powers on samples with no flow after long exposure times. The formation of solids was accompanied by strong PPOCT signals. These observations are consistent with the prior mechanistic studies of photocoagulation that showed significant concentrations of metHb at the onset of coagulant formation [142]. Taking into consideration light scattering and the relatively low powers used for *in vivo* imaging in this work, the second mechanism most probably is the primary contributor to the PPOCT signal for *in vivo* imaging.

Establishing a more clear understanding of the photophysics at play will be key to moving forward and developing techniques for oxygen saturation measurement. In the first mechanism, formation of metHb is believed to primarily follow from oxy-Hb. The lack of sensitivity to deoxy-Hb would complicate any algorithm designed to measure oxygen saturation. The second mechanism on the other hand would occur in both oxy- and deoxy-Hb and likely change the NIR absorption in different ways. This mechanism would lend itself to a more straightforward algorithm development.

We should also note that there may be some contribution simply from the thermal heating of the sample leading to movement of the scatters. Both mechanisms involve heating of the sample. This type of contrast has been observed previously with gold nanoparticles [70, 145] as well as blood [146]. In these works, thermal heating leads to submicron movement of the scatterers that is detected in the interferometric phase by phase-sensitive OCT. In our PPOCT experiments we measure the modulation of the inter- ferometric amplitude, not the phase. While there is undoubtedly some modulation of the phase as well, the scatterer motion should be well below the resolution of the OCT system and therefore only make a very minor contribution to the signal, if any. Additionally, we would expect a strong signal in the interferometric phase at the modulation frequency if the signal were due to thermally induced movements of the scatters. We only measure a very weak phase signal when the amplitude signal is quite strong. Finally, the PPOCT images of the blood filled capillary tube in Figure 20 shows signal at the bottom surface of the capillary tube but not the top. This is a well-known artifact associated with PPOCT (discussed above) that should not be present if the contrast were due to thermally induced movement of the blood.

3.1.2.2 Time resolved PPOCT for molecular specificity

The vastly different excited state dynamics of Methylene Blue and hemoglobin allow the two chromophores to be differentiated by observing PPOCT signals from two different interpulse delays: one immediately after the pump, where the transient absorption should be greatest, and one long after the excited triplet state of the Methylene Blue has relaxed down to the ground state. The current PPOCT system can image Methylene Blue and hemoglobin simultaneously and subsequently separate the two signals based on ground state recovery time.

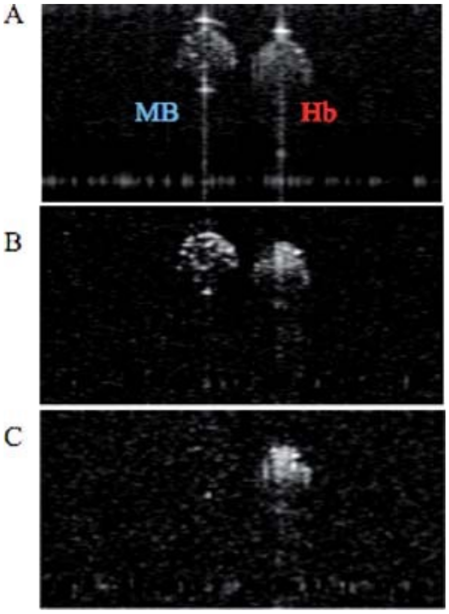

Figure 20: (A) OCT B-scan of Methtylene Blue (MB) and hemoglobin (Hb) in acrylic capillary tube (B) Corrrespoding PPOCT B-scan with a pump/probe delay of 3 ns. (C) Corresponding PPOCT B-scan with a pump/probe delay of 24.8us

In order to verify this assertion, two capillary tubes (200mm inner diameter), one filled with bovine whole blood and the other filled with Methylene Blue, mixed with polystyrene beads to provide scattering contrast, were imaged with the PPOCT sys- tem. The pulse picker of the Ti:Sapphire laser was synchronized with both the trigger input of the Nd:YVO4 and the linescan camera of the spectrometer. The power at the sample of the Ti:Sapphire and the Nd:YVO4 were kept constant at 90 mW and 15 mW, respectively. Both probe and pump were operated at a repetition rate of 40 kHz. As shown in Figure 20, PPOCT B-scans of the capillary tubes containing Methylene Blue and hemoglobin were obtained. Figure 20(A) depicts a conventional OCT B- scan of the capillary tubes. Figure 20(B) depicts a PPOCT B-scan obtained with a pump/probe delay of 3 ns, thus ensuring optimal PPOCT signal from methylene blue. Figure 20(C) shows a

PPOCT B-scan taken at an interpulse delay of 24.8 us, ensuring that the probe irradiation occurs well after the 297 ns ground state recovery time of the triplet state. As expected, this results in no PPOCT signal from Methylene Blue in Figure 20(C). In contrast to Methylene Blue, hemoglobin's long-lived state populated by the pump allows absorption of the probe even at an interpulse delay of 24.8 us. A PPOCT B-scan obtained with the pump blocked was used for back- ground subtraction from each PPOCT image.

It is important to note, that the specular reflection from the top of the capillary tubes only show up in the OCT image, while the specular reflection from the bottom of the capillary tubes show up in all images. This is consistent with expectations as explained in [135], since only surfaces after an absorption event will carry signal due to transient absorption.

This experiment illustrated the first time separation of different chromophores via lifetime with PPOCT. The extreme difference in the dynamics of MB and Hb enabled the use of only two time points to distinguish them. As the dynamics of the chromophores become more similar it will be necessary to use more sophisticated techniques such as fitting the temporal decay or calculating the average lifetime as shown for MB above. Furthermore, differentiation of chromophores via lifetime may prove important when the chromophores of interest exhibit overlap- ping absorption spectra. If the absorption bands of the chromophores are sufficiently distinct, then techniques such as spectroscopic OCT could be used to differentiate the chromophores based on absorption. However, spectroscopic OCT suffers from an inherent tradeoff between depth resolution and spectral resolution. If high spectral resolution is required to separate the chromophores, knowledge of their depth location is sacrificed. Therefore, differentiation of chromophores via lifetime, as demonstrated in this work, may prove important when the chromophores of interest exhibit overlapping absorption spectra.

3.1.2.3 *in vivo* PPOCT imaging

To demonstrate the first in vivo PPOCT images of Xenopus tadpole vasculature, the SLD was used as the probe, which offered better stability and offered higher power than the pulse-picked Ti:Sapph laser. The probe and pump powers were kept constant at 1.2 mW and 10 mW respectively. Live Xenopus tad- poles were anesthetized according to the animal use protocol overseen by the Institutional Animal Care and Use Committee at Texas A & M University and imaged with the PPOCT system. Figure 4 depicts three OCT B-scans overlayed with the intrinsically co-registered, thresholded PPOCT B-scans. The tadpole vasculature is clearly identified via the PPOCT overlay. It is interesting to note that several capillaries (denoted by arrows), which were not identifiable in the conventional OCT B-scan, are easily identified by the added PPOCT molecular contrast.

We have previously explored the sensitivity of PPOCT both theoretically [139, 132] and experimentally [135, 132]. When imaging melanin with a nearIR pump and probe, we were able to measure PPOCT signals at the full depth of the OCT image. In these experiments we do not have the same control over the sample; however, we can compare signals from vessels measured at various depths to get a qualitative feeling for the sensitivity and potential imaging depth. In a cross-sectional image similar to one shown in Figure 21(A) (nearby in the volume stack) we identified 3 nearly equally spaced vessels. The vessels were at a depth of 0 mm, 223 mm, and 450 mm. On an SNR scale the signal from each was 31 dB, 28 dB, and 23 dB, respectively. The two deepest vessels were capillary sized while the surface vessel was larger. Assuming homogenous tissue with a constant scattering coefficient the signal should decay approximately linearly with depth when viewed on a log scale. A linear fit predicts an SNR of 14 dB at the full depth of the OCT image which was ~950 mm. Under these experimental conditions we should be able to observe PPOCT signal from blood up to the full imaging depth in this sample. Of course it is al- ways possible to trade time (number of A-lines used) for signal in order to improve SNR.

The B-scans in Figure 21 clearly illustrate that PPOCT can be used to discriminate vasculature in vivo. As previously discussed, there are also well known extensions of OCT that can accomplish the same task while also supplying information related to blood flow velocity, DOCT, pvOCT and speckle variance OCT techniques. However, if the flow is orthogonal to the optical axis, the Doppler shift is exactly zero and the DOCT and pvOCT signals will also be zero. This issue is prominent if the path of the vasculature becomes tortuous, in which case the flow changes direction frequently and abruptly lead- ing to nodes in the DOCT and pvOCT images. These vessel discontinuities must be restored in order to properly map the vascular network.

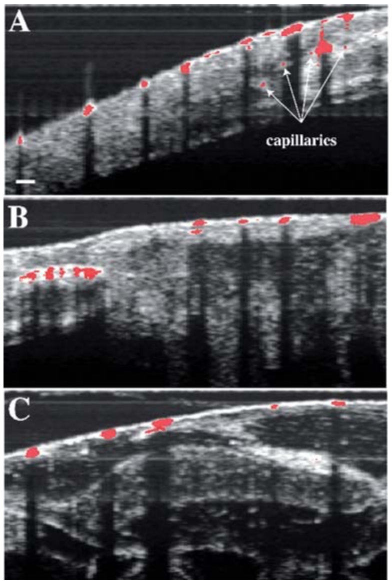

Figure 21: (A), (B), and (C) are PPOCT B-scans overlaid on the corresponding co-registered OCT B-scans. X. laevis vasculature are clearly depicted. Arrows in (A) point to capillaries that were not visible in conventional OCT. Scale bar is 100 mm.

The B-scans in Figure 21 clearly illustrate that PPOCT can be used to discriminate vasculature in vivo. As previously discussed, there are also well known orthogonal to the optical axis, the Doppler shift is exactly zero and the DOCT and pvOCT signals will also be zero. This issue is prominent if the path of the vasculature becomes tortuous, in which case the flow changes direction frequently and abruptly leading to nodes in the DOCT and pvOCT images. These vessel discontinuities must be restored in order to properly map the vascular network.

To illustrate this point, a volumetric PPOCT image of a tortuous vessel in an anesthesized Xenopus tadpole was acquired. Conventional DOCT and pvOCT post processing was performed on the same data set, since, the data required for Doppler and phase-variance processing is already acquired for PPOCT imaging. To ensure that the discontinuities in the DOCT and pvOCT images were not just due to low SNR at random image location, but rather due to low SNR at and around the nodes, we implemented spatial averaging to improve the SNR of the image. The same processing was also applied to the PPOCT images to facilitate comparison. We should note that far more OCT a-lines were used to calculate the DOCT image than are typically used which further improved the SNR over what is typically found in the literature. The averaging was performed as follows. The vol- umetric image was convolved in three-dimensions with a weighting function in which the weights were calculated as one divided by the pixel distance from the center pixel, including all pixels up to 2 from the center. For the purpose of calculating the weighted average of the pixels near the perimeter of the volume, the pixels outside the volume boundary were assumed to have a pixel value equal to the nearest known pixel value.

Figure 22 depicts an OCT volume (A) and two B-scans (B, C) depicting cross-sectional images of blood vessels. (D – G) are cross-sectional cuts along the yellow lines depicted in (B) and (C). The OCT, pvOCT, DOCT, and PPOCT images are depicted in (D), (E), (F), and (G), respectively. As discussed above, vasculature contrast in pvOCT and DOCT may result in nodes when imaging tortuous vessels. Because of its inherent molecular contrast, PPOCT is not sensitive to directionality of flow. This fact is evidenced in Figure 22(G), in which the entire vessel structure is clearly demarcated by the additional PPOCT contrast. Note that sharp changes in flow directionality do not degrade the PPOCT signal, in contrast to the pvOCT and DOCT images where nodes are clearly visible. From these results it appears PPOCT contrast may be more desirable than

DOCT or pvOCT when imaging tortuous vasculature. In addition, since pvOCT and DOCT processing can be performed on PPOCT data, any flow velocity information not inherent to PPOCT contrast can be obtained in post-processing.

Speckle variance techniques for imaging flow with OCT can also accurately reproduce the vasculature even when the flow is orthogonal to the illumination.

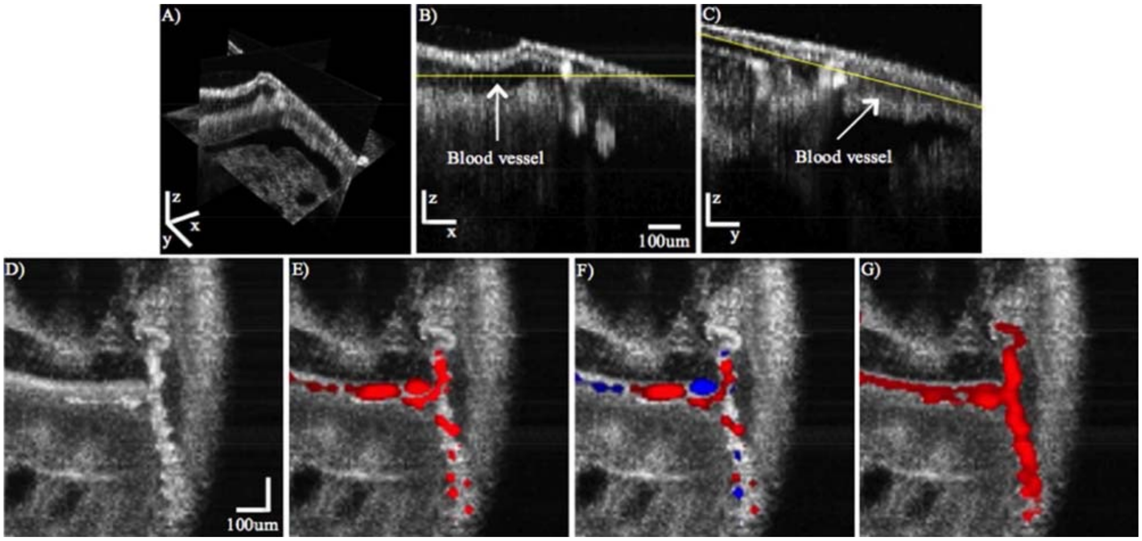

Figure 22: Volumetric OCT image of tadpole. (B) Cross-sectional image in the x, z plane. (C) Cross-sectional image in the y, z plane. D–G are cross-sectional images along the plane defined by the yellow lines in (B) and (C). (D) OCT image (E) OCT image overlaid with the phase variance signal indicating blood flow (F) OCT image overlaid with the Doppler Signal blood flow and direction. (G) OCT image overlaid with the pump-probe signal from blood. Note the continuity in the vessel indicated by the PPOCT image in this tortuous blood vessel. The tortuosity results in a large number of direction changes and therefore nodes in both the Doppler and phase variance images.

Speckle variance techniques for imaging flow with OCT can also accurately reproduce the vasculature even when the flow is orthogonal to the illumination. However the imaging speed for these techniques are fundamentally tied to the speckle decorrelation time which can be milliseconds [147, 148] for slow flowing blood like that found in capillary beds. Consequently, improving the imaging speed of the OCT system by for instance using a linescan camera with shorter read time and therefore higher line rates will not improve the imaging speed of speckle variance techniques in the same way it would for PPOCT.

Neovascularization and angiogenesis in malignant tumors typically leads to tortuous and leaky vascular networks. According to [149], “blood vessels of tumors are a messchaotic, leaky, inefficient, and barely making do.” OCT and its functional derivatives have been used extensively as a tool for understanding tumor growth including neovascularization and angiogenesis [150]. PPOCT imaging of hemoglo- bin can augment this set of tools to provide a more complete vascular map. It may also be able to provide some insight into leaky vasculature if erythrocytes are leaked to the surrounding tissue.

Many cancer studies are initiated for, or involve the imaging of excised tissue either from tissue biopsies or from excised tumors. In these cases, OCT techniques which require flow for mapping vasculature obviously fail. However, since PPOCT imaging of vas- culature only requires the presence of hemoglobin, it may be used as a tool to grade the extent of neovascularization and angiogenesis in excised tissues.

An ex vivo image of the vasculature in a euthanized Xenopus tadpole is shown in Figure 23. These two views of a volumetric PPOCT dataset show several vessels including a bifurcation. Qualitatively, the signal strength from non-flowing blood is stronger than for flowing blood. This may be due the generation of metHb in coagulated blood, hence engaging the first of the mechanisms for PPOCT signal gen- eration discussed above.

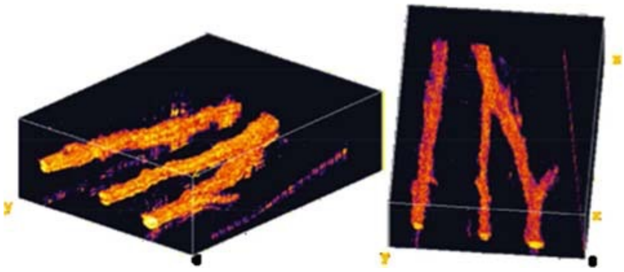

Figure 23: Two views of a volumetric reconstruction of the PPOCT data recorded on a euthanized Xenopus tadpole. The volume is 2mm 2mm 1mm. The lines in the low- er left and right edges of the images are artifacts.

PPOCT is directly measuring absorption in the molecule of interest, which suggests this technique could be used to measure blood oxygen saturation (SO2), a key parameter for early indication of many pathological conditions. PPOCT for retinal imaging may enable vasculature demarcation with simultaneous SO2 measurements. The complementary struc- tural and functional information provided via PPOCT may enable more accurate tracking of ocular diseases. The current standard for functional retinal imaging is a multi-color Scanning Laser Ophthalmoscope (SLO). However, SLO images are restricted to an en face view of the fundus due to its confocal gating detection scheme. Therefore, SO2 measurements and other functional parameters can only be extracted from the surface of the fundus. However, the retinal microvasculature is a complicated, three-dimensional network that extends through the different retinal sub-surface layers. As is well recognized, OCT coher- ence gating enables micron-scale, depth-resolved structural mappings of retinal layers. The additional molecular contrast provided by PPOCT could enable depth-resolved functional measurements of the entire retinal microvasculature, rather than solely surface vessels.

3.2 Imaging in larval stage of Zebrafish treated with MB

3.2.1 Method

As an initial step, we took a fresh look at the choice of pump laser sources. Recognizing the inefficiency of the 532 nm excitation, we looked to laser sources that could excite near the 660 nm peak where the absorption cross-section is a factor of 20 larger. Pulsed lasers with 10–100 kHz repetition rates at that wavelength are uncommon, hence we turned to continuous-wave (cw) diode lasers that could be amplitude modulated. Such lasers are inexpensive, robust, and readily available. In this regime, where there is no longer short-pulse laser ex- citation, the timing between the pump and probe pulse is obviated, thus enabling the use of cw probes, such as a superluminescent diode. Since the probe is the OCT light source, this paradigm shift enabled PPOCT imaging of MB with only minor modifications to an 830 nm band spectral-domain OCT system.

The losses due to transient absorption can be modeled as a reduction in the sample reflectivity (R_s), where the OCT signal is proportional to $R_s^{1/2} = r_s$. In the case of absorption due the triplet state of MB the reflectivity becomes $r_{s,0}(1 - \sigma_T N_T dz)$ where $\sigma_T$is the triplet state absorption cross-section, $N_T$is the triplet state population, dz is the pathlength, and we have assumed the weak absorption limit where the exponential function can be approximated by the first two terms of its Taylor series expansion. Prior to interacting with the pump laser, N_T is exactly zero. If we assume an impulse pump excitation, then N_T is populated by intersystem crossing from S_1 with a quantum efficiency of q and immediately begins to decay, yielding $N_T = qN_{S1}e^{-t/\tau}$ where τ-1 is the decay rate back to the ground state and the decay is assumed to be a single exponential. This approximation holds for short pulsed pump lasers as in our previous work. [131] There we were able to measure τ for MB by varying the interpulse delay between the pump and probe to map out the decay and fit to a single exponential. In the case of a sine modulated pump laser (i.e. $\frac{P_{pu}}{2}[1 + sin\ \omega t]$) we must explicitly consider the time dependent population of N_{S1}. Under these circumstances the triplet state population is proportional to the convolution, $N_T \propto [1 + sin(\omega t)] \otimes e^{-t/\tau}$. Evaluating the convolution yields, $N_T \propto \left[1 + (1 + \omega^2\tau^2)^{-1/2}\right]$.where $\phi = tan^{-1}\,\omega\tau$. Inserting a proportionality constant, β, to account for the efficiency with which the singlet excited (S_1) state is populated as well as folding in the quantum efficiency (q), the absorption cross-section (σ_T) and a factor of 0.5 we can rewrite the reflectivity as $r_s \approx r_{s,0}\left(1 - dzP_{pu}\beta\left[1 + (1 + \omega^2\tau^2)^{-1/2}\, sin(\omega t - \phi)\right]\right)$. Here we can see that the transient absorption signal will be sine modulated at the same frequency as the pump modulation with a phase shift of ϕ and scaled by $(1 + \omega^2\tau^2)^{-1/2}$. The phase shift and scaling are both dependent on the product of the modulation frequency and triplet state lifetime. This result is exactly analogous to frequency domain fluorescence lifetime microscopy where the phase of the signal is used to measure fluorescence lifetimes. [151] In our case the phase can be used to determine the triplet state lifetime.

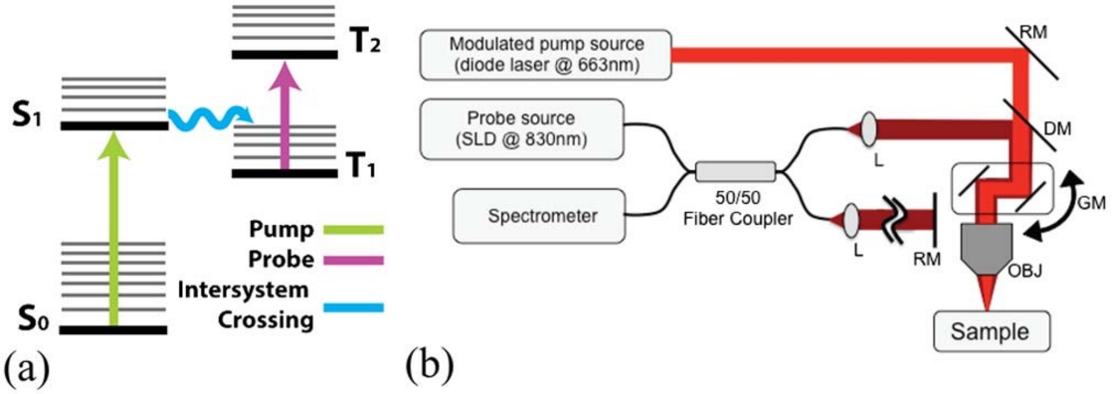

Figure 24: (a) Simplified energy level diagram for methylene blue. (b) PPOCT system schematic. Pump source, modulated 663-nm diode laser; probe source, SLD at 830-nm center wavelength; DM, dichroic mirror; RM, reference arm mirror; GM, galvanom- eter scanner; OBJ, objective lens.

The modified OCT system used for this study is shown schematically in Figure 1b. A superluminescent diode with ~40 nm bandwidth centered at 830 nm was used as the OCT light source. The pump source was a 663 nm diode laser (Toptica, iBeam Smart PT660) with a maximum output of 60 mW. The output of the diode laser could be sine modulated and/or pulsed. The 830 nm light was launched into a 2x2 fused fiber coupler that formed a Michelson interferometer. The 830 nm light in the sample arm also constitutes the probe. The pump beam was directed into the sample arm via a dichroic mirror. The pump and probe were focused at the same position to a spot diameter of ~19 μm and laterally scanned on the sample by a galvo mirror pair.. The signal due to the absorption of the pump was frequency encoded by modulation of the pump at 14 kHz in all cases. The detector was a custom spectrometer operated with a line rate of 40 kHz and 8 μs integration time. The spectral interferograms were processed in the typical way to generate OCT M-scans. The PPOCT signal was extracted from an M-scan via Fourier transform along the time axis and filtered as described previously [135].

3.2.2 Results

Initially we conducted a simple experiment on a phantom to validate a new background subtraction method. The background arises from amplitude noise on the light source that decays approximately as 1/f. The phantom was a 200 μm inner diameter plastic capillary tube containing a flowing solution of 2% MB mixed with titanium oxide (Sigma-aldrich). The pump power was 4.4 mW and the probe was 1.4 mW. The tube was positioned at an angle to avoid the strong specular reflection from the tube surface. Figure 2a is the power spectrum at one depth in a PPOCT A-line of the phantom. The peak at 14 kHz (pump on) is the PPOCT signal. When the pump is off the PPOCT signal is gone, but the noise remains. As a result, there is a strong background signal which if left uncorrected could complicate the interpretation of PPOCT images. In order to mitigate this problem, we used a background normalization method to remove signal background due to source intensity noise at the pump modulation frequency. The background level at frequencies above and below (±2 kHz) the pump modulation frequency were measured and averaged. The implicit assumption is that the background is well represented by a linear function over this small frequency range. The PPOCT signal was divided by the average noise background level, hence the mean of the noise background is 1. The normalized PPOCT signal was then thresholded to remove all of the noise background. We found that a threshold of 2.5 was sufficient to completely remove the background seen in the images of the phantom, Figure 25(b). This algorithm could be done on each pixel in the PPOCT image to enable essentially real-time measurement and removal of the background.

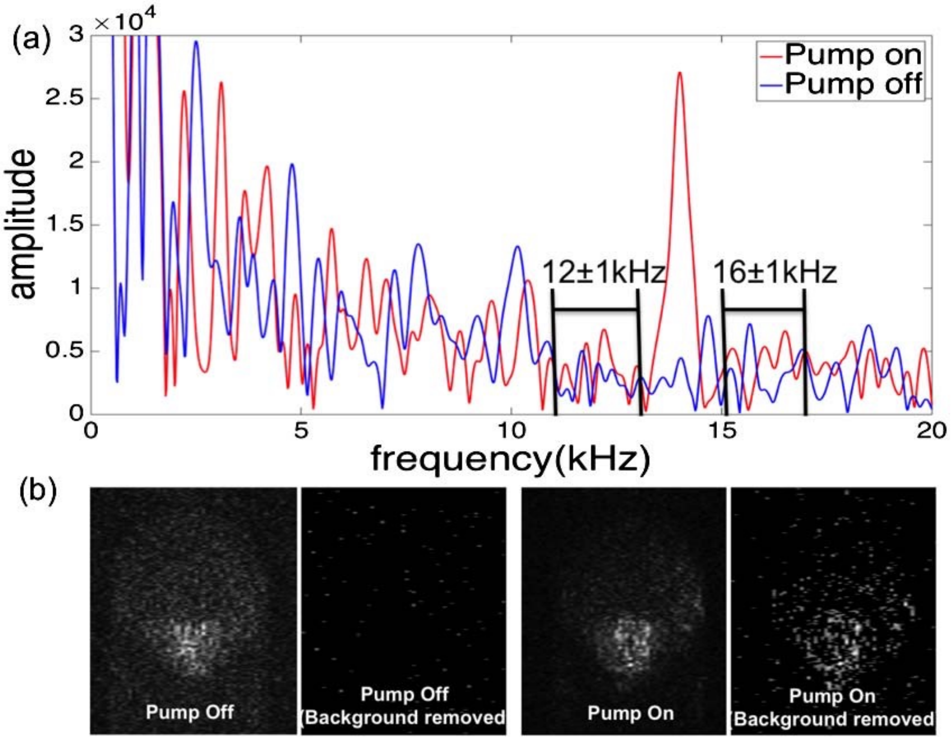

Figure 25: (a) Frequency domain signal from one pixel in the MB filled capillary tube with and without the pump on. The relevant aspects of the background subtraction algorithm are labeled where the background is assumed to vary linearly over a nar- row frequency range. (b) Comparison of PPOCT images with background subtraction, demonstrating the complete removal of the of noise background

Using this same phantom we sought to estimate the sensitivity of the technique. The essential idea was to measure the signal as a function of concentration and extrapolate to a minimum measureable concentration. We can arrive at the appropriate relationship by recognizing that $r_{s,0}$ is measured directly by the conventional OCT signal and β is a linear function of the MB concentration (C). Since we only extract the sine modulated portion of r_s the ratio of the PPOCT/OCT signals is $dzP_{pu}\beta(1+\omega^2\tau^2)^{-1/2}$ where other constants not specifically considered like detector responsivity cancel because they are the same in both the PPOCT and OCT signals. Since all other variables are known in a phantom experiment and only β varies with concentration, a measurement of this ratio as a function of concentration will reveal $\beta(C)$.

Measurements were made at 5 different concentrations of MB, 0.01%, 0.5%, 1%, 1.5% and 2%. The ratio $PPOCT/\left(OCTdzP_{pu}\right)$ was calculated as a function of the concentration and the results fit to a line to get $\beta(\mu m^{-1}mW^{-1}) = 0.087C(w/v\,\%) + 8.7\times10^{-5}$ with an R^2 of 0.95. Based on these results, if we assume a pathlength of 15 µm, a pump power of 1 mW, a tissue reflectivity of -30 dB, and a system sensitivty of 110 dB we can expect to be able to measure 0.013% (41 µM) concentration of MB with a PPOCT SNR of 1 dB. Here we are not explicitly considering the attenuation of the pump beam. However, if we assume we started with the ANSI limit for skin at 660 nm (19 mW) at the tissue surface and assume the scattering coefficient of 10% intralipid is a reasonable approximation for tissue (56 cm-1 at 660 nm [152]), then the pump would be reduced to 1 mW of power at a depth of ~0.5 mm.

In order to exam the capacity to measure MB in a biological sample we chose to image larval stage zebrafish. Zebrafish are an important model for developmental biology as well as numerous human diseases. [153] Larval zebrafish, treated in accordance with an animal use protocol overseen by the Institutional Animal Care and Use Committee (IACUC) at Texas A & M University, were obtained 14 days after breeding. The zebrafish had been treated with PTU to suppress melanin expression and housed in water free of MB. In order to stain the embryos a 0.01% aqueous methylene blue solution was prepared. The embryo was transferred to the MB solution and remained there for 6 hours before imaging. For reference, aquarium water is frequently treated with a 10 times lower concentration of MB for its antiparasitic effect while for the identification of sentinel nodes [154] in breast cancer a solution about 100 times stronger is injected. The embryos were anesthetized with MS222 (250mg/L, tricaine) before imaging. For in vivo imaging the pump and probe had a power of 1.4 mW.

In order to verify where MB was accumulating in the treated zebrafish, we processed histological slides were prepared for both treated and untreated specimens, Fig. 3a and 3b, respectively. The large dark areas on either side of the treated specimen near the midline correspond to the mesonephros, the basic excetory organ where MB is clearly accumulating in the treated sample. The mesonephros is the primodial kidney in fish and amphibians. MB is known to be cleared by the kidneys in humans when taken orally [155], so accumulation in the mesonephros was not unexpected. It is also rapidly reduced to leucomethylene blue which has no visible wavelength absorption and should be invisible to the PPOCT technique described here. It is likely that most of the MB was in the reduced form during the in vivo experiments and the intense blue coloring of the mesonephros is due to the fact that leucomethylene blue is also rapidly oxidized to MB by air [38] which would have happened during processing of the slides. In the untreated animal there are several dark areas at the top, bottom, and sides. It seems likely that these are due to incomplete suppression of melanin expression. The areas on the side coincide approximately to region of the mesonephros but are more superficial and likely due to highly pigmented stripes observed in adult zebrafish.

Just below the histology sections in Figure 26 (c, and d) are the fused OCT/PPOCT cross-sectional images generated by overlaying the background removed

PPOCT image on top of the OCT image. The images are from a similar location, but different animals than the histology slides. PPOCT signal arises from the same region as the darkened areas in the histology slides. The size of stained region of the mesonophros also qualitatively agrees with the histology, showing a large stained area where the mesonephros should be. The PPOCT signal along the back and superficial along the midline of the fish are attributed to residual melanin.

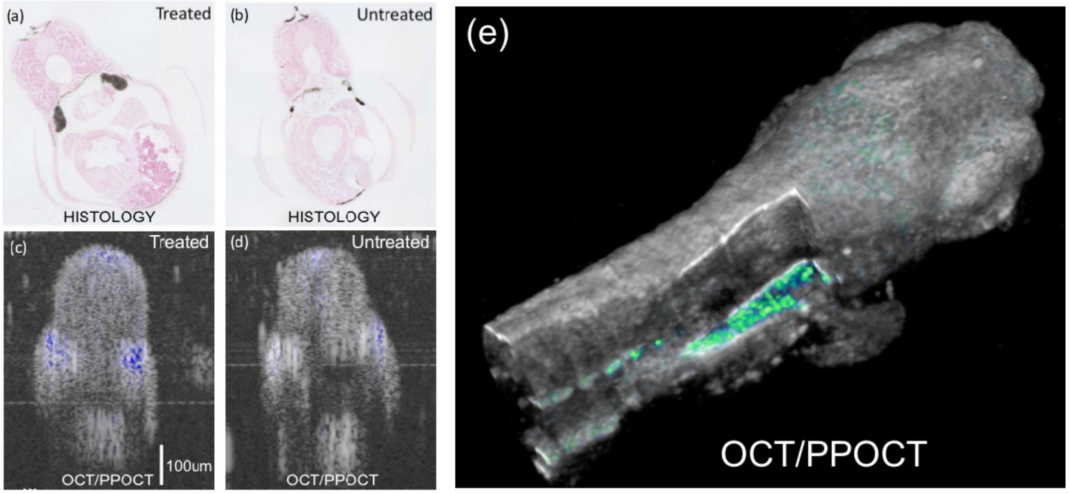

Figure 26: (a),(b) Histological cross-section from a zebrafish. Treated area corresponds to 0.01% (w/v) MB. Large dark areas at the midline of the treated animal are interpreted as accumu- lated MB in the mesonephros. Other dark areas also present in the untreated animal are attributed to residual melanin. (c), (d) Corresponding PPOCT cross-sectional images. Note, OCT images are shown on traditional log-intensity scale and PPOCT is shown on linear-intensity scale. (e) Intersecting planes from volumetric-data set with PPOCT signal and overlain on the OCT signal of a live zebrafish treated with MB.

4. DEVELOPMENT OF LESSLESS, ULTRA-WIDEBAND FIBER OPTIC ROTARY JOINT FOR BIOMEDICAL APPLICATIONS*

In this chapter, the lensless and ultra-wideband fiber optic rotary joint for endoscopic molecular-enhanced OCT imaging is developed, and also demonstrated how the performance of FORJ was tested.

4.1 Method

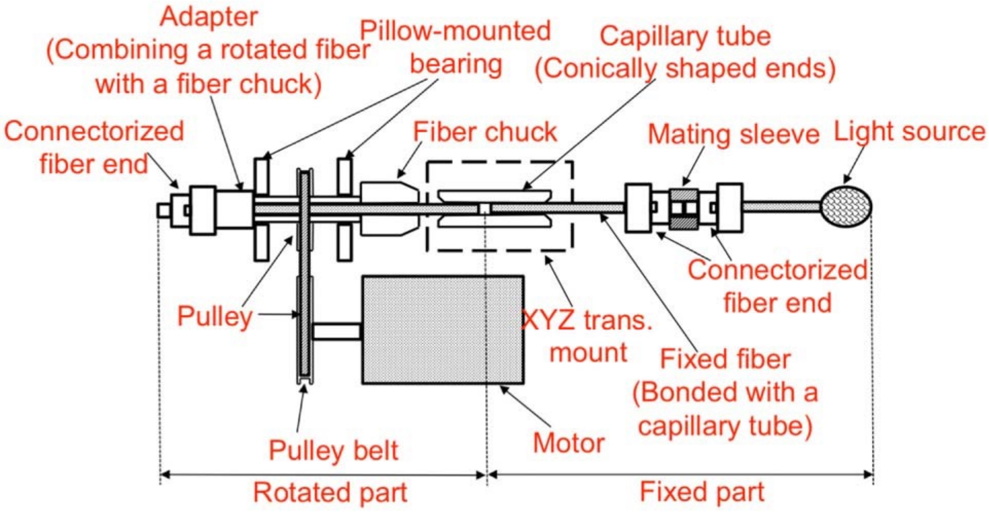

Figure 27: Schematic diagram of UFORJ

The primary components of the lensless ultra-wideband fiber optic rotary joint (UFORJ) are shown in Figure 27. A fiber chuck (FPH-J, Newport) was assembled with

---

* Reprinted with permission from [156] Kim, Wihan, Xi Chen, Javier A. Jo, and Brian E. Applegate. "Lensless, ultra-wideband fiber optic rotary joint for biomedical applications." Optics letters 41, no. 9 (2016): 1973-1976..

two pillow-mounted bearings and a bore diameter ($\emptyset = 3.175$ mm) pulley to hold the rotating portion of fiber. The fiber chuck could accommodate bare fibers up to 250 μm in diameter. An electric motor (RE50, Maxon Motor) fitted with a bore diameter pulley ($\emptyset = 8$ mm) was coupled to the fiber chuck via a pulley belt. The gear ratio and maximum rotation velocity of the loaded electric motor resulted in a maximum UFORJ rotational velocity of 8800 rpm. A short fiber patch cable connectorized on one side was placed in the fiber chuck and secured via a customized fit- ting. The connectorized end allows for easy substitution of fiber components on the rotating portion of the optical system, in our case, a fiber endoscope. The bare, cleaved, end of the patch cable was held by the fiber chuck and inserted into one side of a glass ferrule (FER-1.8-126-GL, OZ Optics) whose diameter (126 μm) was chosen to closely match the diameter of the bare fiber after removal of the buffer. The ferrule had conical shaped ends on both sides that tapered down to the inner ferrule diameter. This enabled easy damage free insertion of bare fiber on either end.

The glass ferrule did not rotate and was attached to a custom fitting held in an x, y, z adjustment mount. The x, y, z mount allowed for careful alignment of the glass ferrule to the fiber chuck. The nonrotating fiber was passed through the opposite end of the glass ferrule and butted up against the fiber held in the fiber chuck. Both fibers were cleaved before being inserted into the glass ferrule. The nonrotating fiber was bonded to the ferrule with epoxy. The glass ferrule was filled with lubricating fluid which served several purposes. It reduced reflections from the cleaved fibers and provided lubrication for the rotating fiber. It also enabled greater separation of the two fibers while maintaining good coupling efficiency.

First, we set out to determine the suitability of potential index matching fluids to cover the requisite bandwidth, 355–1360 nm. In addition to being transparent over this range, the index matching fluid was ideally chosen to minimize insertion loss due to reflections from, and separation between, the two fiber end faces. Losses due to both sources as a function of refractive index (n) and fiber separation (Z0) have been derived previously [157, 158] and are given by

$$\mathrm{L_{ref}} = -10\log\left[1-\left(\frac{(\mathrm{n_1}-\mathrm{n_2})}{(\mathrm{n_1}+\mathrm{n_2})}\right)^2\right], \tag{1}$$

$$\mathrm{L_{SMF}} = 8.686\ln\left[1+\frac{1}{2}\left(\frac{\lambda \mathrm{Z_0}}{\pi \mathrm{n_2} \mathrm{w_0^2}}\right)^2\right], \tag{2}$$

$$\mathrm{L_{\,MMF}} = -10\log\left(1-\frac{\mathrm{Z_0 NA}}{2\mathrm{n_2 r_1}}\right), \tag{3}$$

where L is the insertion loss on a dB scale due to reflection (ref), end-face separation in single-mode fiber (SMF), and in multi- mode fiber (MMF). Z0 is the axial separation between two fiber end faces, NA is the numerical aperture of the fiber, n_1 is the refractive index of the fiber core, r is the radius of the Gaussian beam diameter in a multi-mode fiber, w_0 is the mode field radius, and n_2 is the refractive index of the medium inside the gap between the fibers. Plots of these three equations are provided in Figure 28 with the following assumptions. We assume an NA of 0.2 for a double-clad fiber. r is taken to be the radius of the multimode core; 52.5 µm. w_0 is the mode field radius of the SMF core; 4.6 µm. n_1 is 1.46; and n_2 ranges from 1 to 2.

As expected, losses due to reflection [Figure 28(a)] are minimized when the refractive index of the lubricant (n_2) matches the index of the fiber core, i.e., $n_1 = n_2$. However, even in the worst case where the gap is air filled ($n_2 = 1$), the losses are relatively small at 0.15 dB. Insertion loss due to fiber end-face separation [Figure 28(b) and (c)] is less than 1 dB for separations in excess of 30 μm for all reasonable values of n_2. In the case of dual-clad fiber, one could also estimate the leakage from the single to the multimode core by assuming that all losses go to the multimode core. Under this assumption, Eq. (2) and Figure 28(a) can be interpreted as the leakage. Higher n_2 values can provide higher tolerances for fiber end-face separation, making alignment easier and reducing the potential for damage caused by bringing the two fibers into direct contact. Avoiding fiber damage by maintaining space between the two fiber end faces is expected to be key to achieving long operational life- times for the UFORJ. Based on these results, lubricants with refractive index equal to or larger than the fiber core would be the most desirable.

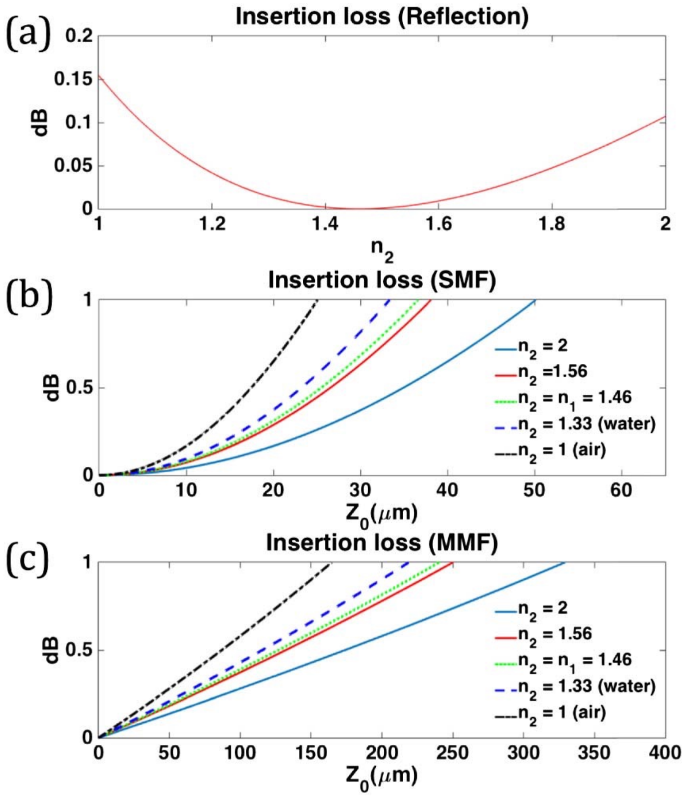

Figure 28: Insertion loss (a) due to reflections, (b) due to the separation of fiber end faces for single-mode fiber (SMF), and (c) due to sepa- ration of fiber end faces for multi-mode fiber (MMF). The fiber was assumed to have a refractive index of 1.46 (n1).

4.2 Results

We identified two potential lubricants both with a refractive index of 1.52. The first was an index matching fluid (Norland 105) with low viscosity but unknown absorption spectrum and UV performance. The second was microscope objective immersion oil (Olympus, Type-F) with relatively high viscosity and a manufacturer reported good performance in the UV. Using a 365 nm light source (Mos-Cure mini 365, U-VIX) we made a qualitative measure of the fluorescence from the two candidates. The immersion oil had relatively low fluorescence emission as reported by the manufacturer, however emission from the index matching fluid was much stronger. Based on these results we moved forward with only the immersion oil since the strong fluorescence from the index matching fluid would introduce a strong background for fluorescence imaging.

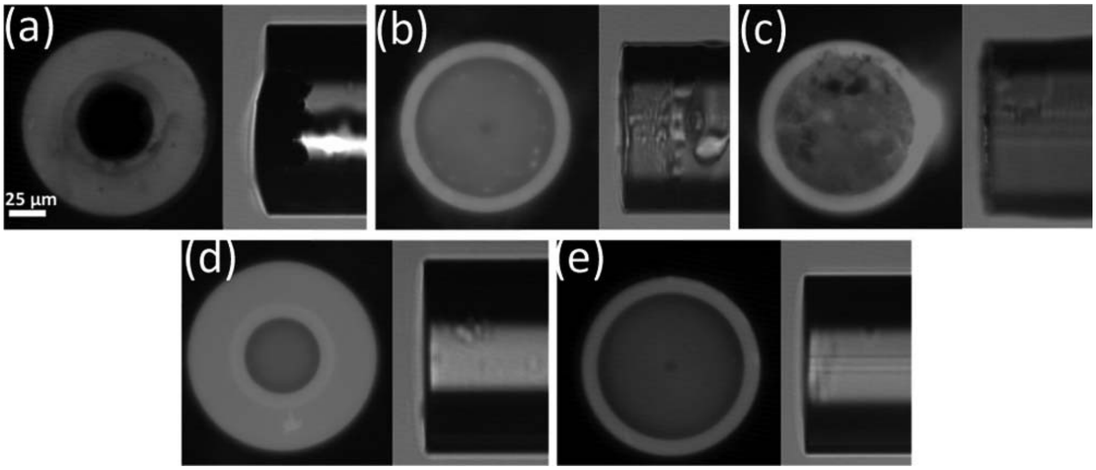

Figure 29: Images of fiber end-face damage after fiber illumination with 355 nm nanosecond laser light using immersion oil (Olympus, Type-F) and distilled water as lubricants (a) MMF after a few minutes with immersion oil, (b) DCF after a few minutes with immersion oil, (c) DCF after 20 minutes with immersion oil, (d) MMF after 20 minutes with water lubricant, (e) DCF after 20 mintues with water lubricant.

We identified two potential lubricants both with a refractive index of 1.52. The first was an index matching fluid (Norland 105) with low viscosity but unknown absorption spectrum and UV performance. The second was microscope objective immersion oil (Olympus, Type-F) with relatively high viscosity and a manufacturer reported good performance in the UV. Using a 365 nm light source (Mos-Cure mini 365, U-VIX) we made a qualitative measure of the fluorescence from the two candidates. The immersion oil had relatively low fluorescence

Next, we tested the immersion oil in the UFORJ, filling the capillary with the oil before inserting the freely rotating fiber. For initial testing, we chose to assemble the UFORJ with a multimode fiber designed to be used with high power lasers (FG050UGA, Thorlabs). The fiber had a core radius of 25 μm and a NA of 0.22. The laser source was a 355 nm, nanosecond pulsed laser with a 10 kHz repetition rate. After initially achiev- ing high power throughput, the power decreased dramatically within a few minutes. After disassembling the UFORJ, we noted physical damage to the fiber end faces. To investigate further, we took bare fibers with freshly cleaved ends and coupled the laser source into the fiber. The laser pulse energy at the exit of the fiber was approximately 3 μJ at a 10 kHz repetition rate. The other end of the fiber was submerged in the immersion oil and illu- minated for up to 20 min. The fiber end face was then imaged using a fusion splicing system (Vytran, FFS-2000) that offered 0.47 μm/pixel sampling. Figure 29(a) shows the results for the MMF in the immersion oil after only a few minutes of exposure. The smooth, cleaved fiber end face is essentially completely re- moved with deep pitting across the entire surface of the fiber core. We postulate that while the fluorescence of the immersion oil is low, the absorption is sufficient to cause localized heating and thermal damage to the fiber. Since we were ultimately interested in using double-clad fiber in our application, we decided to perform similar testing with the SM-9/105/125-20A fiber. It has a multimode core approximately twice as big as the MMF, which should help mitigate the heating issue by lowering the laser intensity by a factor of ~ 4. Figure 29(b) shows the results after a few minutes of exposure. There are some anomalies in the image, but clearly any damage is far less than with the MMF. We then extended the experiment using a fresh fiber to a 20 min exposure. The results, Figure 29(c), show obvious damage with pronounced pitting in the fiber endface. Clearly, the immersion oil cannot be used as a lubricant for chronic experiments when a UV pulsed laser is used, e.g., fluorescence lifetime imaging. However, the immersion oil may be a good solution for applications that use cw laser sources, since the peak intensity would be drastically reduced and likely enable damage free operation.

Since the development of our application, multimodal intra- vascular imaging with FLIM requires a short-pulsed UV laser source, we continued our pursuit of a suitable lubricant. The solution we arrived at was to simply lubricate the UFORJ with dis- tilled water. The solution has the requisite lack of absorption and emission over our desired spectral range. Likewise, with a refractive index of 1.33, it performs (see Figure 28) fairly well in terms of minimizing insertion loss due to reflection and increasing the tolerance for axial alignment of the two fibers. However, it is normally not considered to be a good lubricant because of its low viscosity and tendency to promote oxidation. Neither of these concerns is particularly relevant for this application. The rotating surfaces in contact with water are all smooth glass surfaces and nominally not load bearing; hence, the relative increase in friction due to the poor lubricant will not significantly impact the operational lifetime of the UFORJ. As an initial test of the water lubricant performance, we completed similar experiments, as de- scribed above, using bare fibers and inspecting the fiber end face for damage. The results are in Figure 29(d) and (e). After 20 min of exposure, there was no observable damage to the fiber.

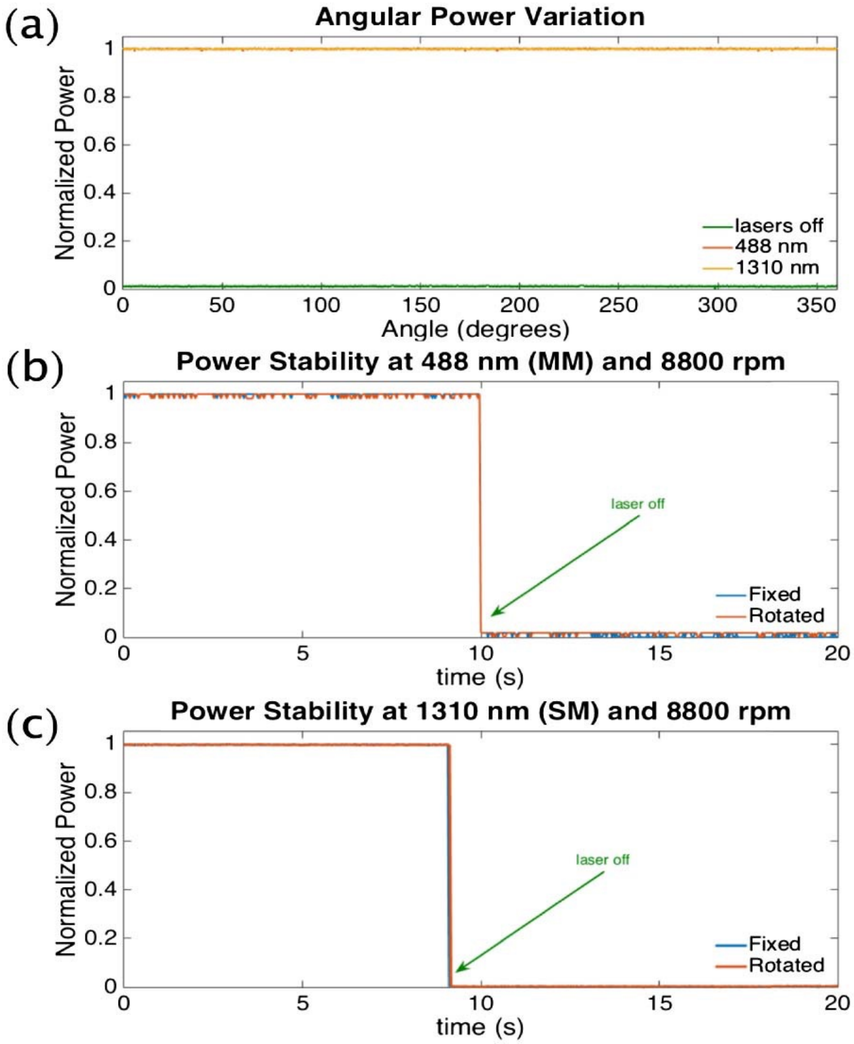

Figure 30: Measured output power variation with rotation of UFORJ. (a) Step-wise rotation through one cycle; (b) continuous rotation at 8800 rpm (146 Hz), 488 nm light coupled into the multimode core; and (c) continuous rotation at 8800 rpm (146 Hz), 1310 nm light coupled into the single-mode core.

After assembling the UFORJ using the double-clad fiber and distilled water as the lubricant, we began testing the functional performance of the rotary joint. For testing, we used two lights sources, a 488 nm cw diode laser (Toptica, iBEAM-SMART- PT-488HP) and a swept-laser source centered at 1310 nm with a sweep range of ±50 nm (Thorlabs, VCSEL, SL1310V1- 10048). We typically use the former for frequency domain FLIM applications and the latter for optical coherence tomography. Figure 30(a) shows the results for both wavelengths where the 1310 (single-mode core) and 488 nm (multimode core) light was coupled into the double-clad fiber and the UFORJ rotated through 360° while measuring the output with a power meter. The peak-to-valley variation of the throughput power was 0.07 dB at 488 nm and 0.15 dB at 1310 nm. The mean and standard deviation of the output power are essentially identical for both the rotating and nonrotating case, i.e., within the accuracy of our measurements, there is no variation in the insertion loss upon rotation. We also tested the UFORJ during high-speed rotation using fast photodetectors. Figure 30(b) and (c) show the results of measurements with continuous rotation at 8800 rpm (146 Hz) over 20 s. The averaged output power was 24 mW from 488 nm and 9.95 mW from 1310 nm with continuous rotation. The variation in the signal from the 488 nm laser on the photodetector, SD=7.6×10^{-3}, was similar to the noise when the laser was off, SD=6.4×10^{-3}. The intensity noise induced by rotation in the multimode core, therefore, is less than 1%. The variation in the signal from the 1310 nm laser on the photodectector, SD=8.3×10^{-4}, was similar to the noise with the laser off, SD=7.7×10^{-4}. The intensity noise induced by rotation in the single-mode core is less than 0.1%. For both the single-mode and multimode cores, we are near our limits of detection; hence, the values quoted should be taken as upper limits.

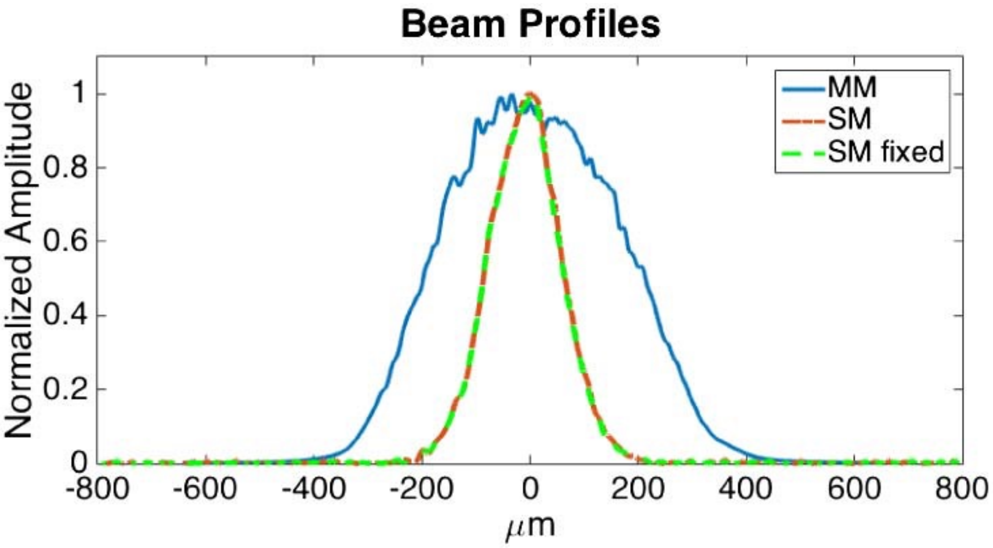

Figure 31: Measured beam profile from multimode (MM) and single- mode (SM) cores of the UFORJ while continuously rotating at 8800 rpm and the single-mode core while fixed.

Finally, we examined the integrity of the spatial mode to ensure that light propagating down the single-mode core was not bleeding into the multimode core at the interface of the two fibers. Some imaging technologies, such as OCT, suffer from artifacts when executed with multimode fiber. Using commercial beam profilers (Thorlabs, BP104-VIS or IR), we measured the profile of the fiber output after the UFORJ from light launched in both the single-mode and multimode cores. The measurements were made while rotating the UFORJ at 8800 rpm. The single-mode and multimode cores were illuminated with the 1310 and 488 nm light, respectively. The beam profiler, either Vis or IR, was placed at a fixed distance from the output of the fiber with no optics between. Only the relative size and shape of the two profiles have meaning. We expected that any significant coupling between the single-mode and multimode core would appear as broadening at the base of an otherwise Gaussian looking profile from the single-mode core.

Figure 31 shows the results. We first note that there is no apparent change in the spatial mode, comparing the fixed and rotating measurements from the single-mode. It is also apparent that there is no significant shoulder on the profiles from the single-mode core that could be attributed to 1310 nm light propagating in the multimode core. While there must be some leakage into the multimode core, this evidence suggests that it is small and beyond our current measurement technique.

We have begun using these UFORJ initially for intravascular FLIM imaging. Our experience so far is that the operational lifetime of the UFORJ is at least sufficient for research purposes. The longest imaging session to date was 3 h with 22 pullback images at rotational velocities of 2400–6000 rpm. At the end of the session, the UFORJ was still performing well. Given that the fiber end faces need not be in direct contact, we expect that operational lifetimes can ultimately be made to rival those of standard commercial FORJ.

5. FREQUENCY DOMAIN PUMP-PROBE OCT LIFETIME IMAGING OF MICROENCAPSULATED METHYLENE BLUE QUENCHING BY OXYGEN

This chapter discusses the design and development of the microencapsulated MB using PLGA as a new contrast agent for PPOCT and algorithms for detecting the excited state lifetime in the frequency domain. First subsection describes the how the microencapsulate MB was tested for PPOCT. Second subsection deals with how the microencapsulated MB works as the oxygen sensor using PPOCT.

5.1 Method

5.1.1 Developing microencapsulated MB and imaging it using PPOCT

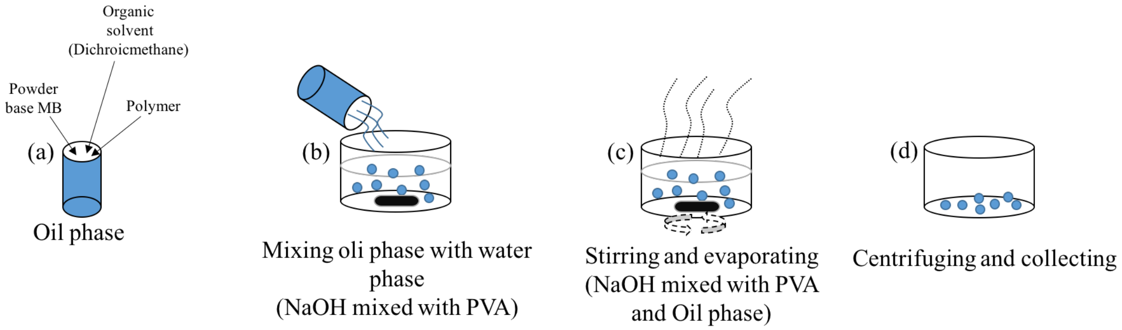

Figure 32: The solvent evaportion method.

The microspheres were synthesized using a solvent evaporation method, tuned to yield microspheres with a diameter of 2.5 μm. In Figure 32 the process of a solvent evaporation method is firstly to dissolve the hydrophobic drug into an organic solvent containing the polymer. Secondly, the oil phase based on an organic solvent containing polymer is emulsified in a water phase. Lastly the emulsified solution is centrifuged in order to sort the particles [159].

The starting concentration of MB was 0.01% w/v (mg MB per 100 ml solvent). For reference a concentration of 1% w/v has been injected to identify sentinel lymph nodes in breast cancer cases. Likewise, concentrations of 0.5-1% are used in chromoendoscopy applications of MB.

The PPOCT system used for this study is shown schematically in Figure 33. The pump source, a 663 nm diode laser, was sinusoidally modulated. The pump beam was directly delivered into the sample arm of the OCT system via a dichroic mirror. The SLD as a probe was launched into a 2x2 fused fiber coupler that formed a Michelson interferometer. Pump and probe beams were focused at the same position and laterally scanned on the sample by a galvo-scanning mirror. A tissue phantom was constructed from a 100 μm inside diameter plastic capillary tube containing a flowing suspension of MB microspheres submerged in 1% intralipid emulsion to mimic scattering in biological tissue. Also a tagging phantom was demonstrated by sprinkling MB microspheres onto a gelatin-based artificial tissue to mimic a monolayer tagging in biological tissue. The average probe power was 1.4 mW and the average pump power was 5.5 mW modulated at 10 kHz. If there is transient absorption, the pump modulation will be transferred to the probe (OCT signal). The PPOCT signal is extracted by measuring an M-scan, band pass filtering at the modulation frequency and integrating, hence one M-scan yields a single PPOCT A-line.

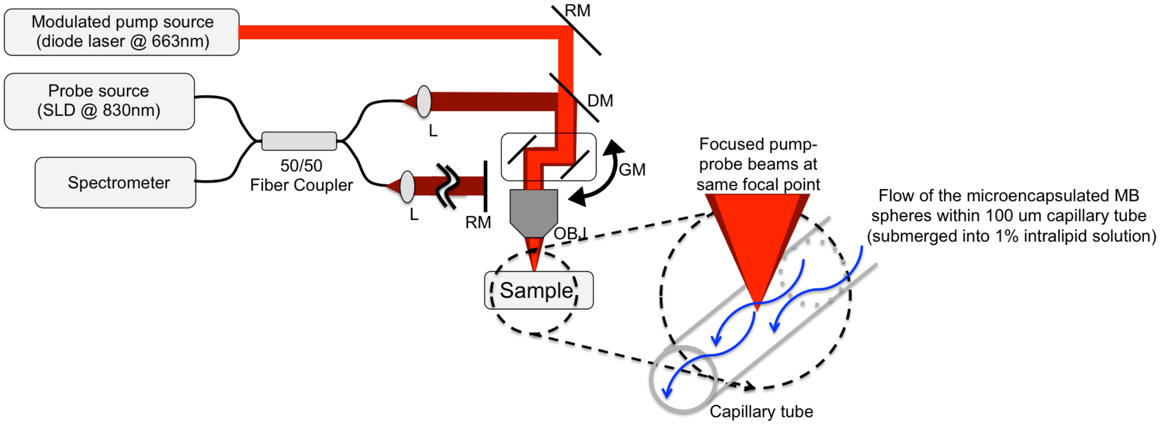

Figure 33: PPOCT system. Pump source: sinusoidal modulated 663nm diode laser, Probe source: 830 nm center wavelength SLD, L: lens, DM: dichroic mirror, RM: refection mirror, GM: galvanometer scanner, OBJ: objective lens.

5.1.2 Measuring the lifetime of transient absorption from the oxy/deoxygenated microencapsulated MB

Using time-resolved pump-probe spectroscopy, we measured the lifetime of transient absorption from the microencapsulated MB. The experimental system that we used for pump-probe spectroscopy in Figure 34(a). Based on ground-state and transient absorption peaks of the aqueous MB [134], a femtosecond Ti:sapphire laser ($\lambda_0 = 830\mathrm{nm}, \Delta\lambda = \pm 2\mathrm{nm}, \text{pulse width} = 140\mathrm{fs}$, Coherent, Chamelon-Ultra II) was used as a probe light source and modulated with 10 kHz using a pulse picker (Coherent,). As a pump light source, a diode laser ($\lambda_0 = 663\mathrm{nm}, \Delta\lambda = \pm 3\mathrm{nm}, \text{pulse width} = 400\mathrm{ns}$, Toptica, iBeam Smart PT660) was used and controlled by a delay generator (Highland Technology, P400), and 2 kHz sinusoidal signal generated from a function generator (Stanford Research System, DS335) was fed to modulate a pump light. By using a dichroic mirror (Semrock, ff670-SDi01-25×36), pump and probe beam are propagated and focused onto a same focal spot of sample. The computer controlled delay generator externally triggered by a pulse picker was used for delaying a pump light source versus a probe. The pump-probe signal from two beams was measured by a bandwidth balanced detector (Newport, Model 2001) to suppress unwanted noise signal. In order to get pure transient absorption signal, an optical long pass filter (Chroma, ET810lp) was used to block a pump source. The procedure of data process is that the measured signal is Fourier-transformed along the time axis. By delaying the interpulse of probe light led by the pump light from 0 to 6 us, the magnitude of the Fourier-transformed data is extracted from the side band(12kHz) of the carrier frequency (10kHz).

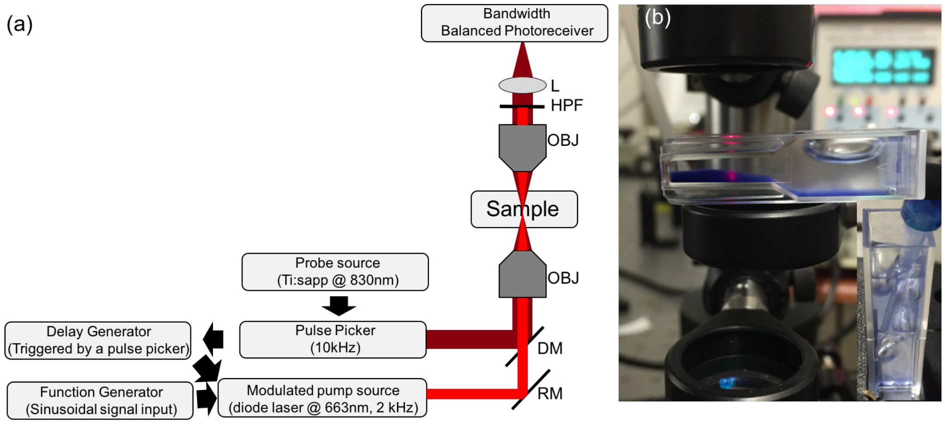

Figure 34: Time-resolved pump-probe spectroscopy system. (a) schematic diagram (a) measuring the lifetime of the trasient absorption from oxy/deoxygenated MB microspheres (lower-right-coner: controlling the oxygen level of MB microsphere by direcllty bubbling air or nitrogen gas), RM: reflective mirror, DM: dichroic mirror, OBJ: objective lens, LPF: low pass filter, L: focusing lens

In order to oxy- or deoxygenated the MB microsphere, we directly bubbled air or nitrogen gas into the microencapsulated MB solution in a cuvette for an hour in Figure 35 (b and lower-right-corner). For the reference data, 0.5% aqueous MB solution was also used to measure the lifetime of transient absorption with same oxygen level by bubbling the gas. In order to keep the condition of oxygen level, the cuvette was well sealed and capped while measuring the signal.

5.1.3 Frequency domain pump-probe OCT to measure phase shift for lifetime imaging

A developed system and algorithm is to observe the relative phase shift between the pump and probe that is a reliable indicator of the oxygen concentration in the frequency domain. The algorithm was described previously [138]. The basic concept is very similar to Frequency-Domain Fluorescent Lifetime Imaging (FDFLIM) [151], except instead of measuring changes in fluorescence we are measuring changes in the transient absorption. In frequency domain, a fundamental phase limit on the phase distribution follows Gaussian white-noise distribution [160]. Thus, the phase sensitivity can be expressed with

$$\delta\emptyset_{\mathrm{sens}} = \frac{1}{\sqrt{2\times 10^{(\mathrm{SNR}/10)}}} \tag{1}$$

,where SNR is the decible scale of PPOCT.

In order to prove the sensitivity of the technique, we compare experimental with fundamental phase sensitivity. Simply we built a Fourier-domain (FD) interferometer that is able to shift the phase of sample signal. We measured the phase by varying τ and SNR. It helps to estimate the limitation of PPOCT system on measuring the phase shift from the microencapsulated MB with varying oxygen concentrations.

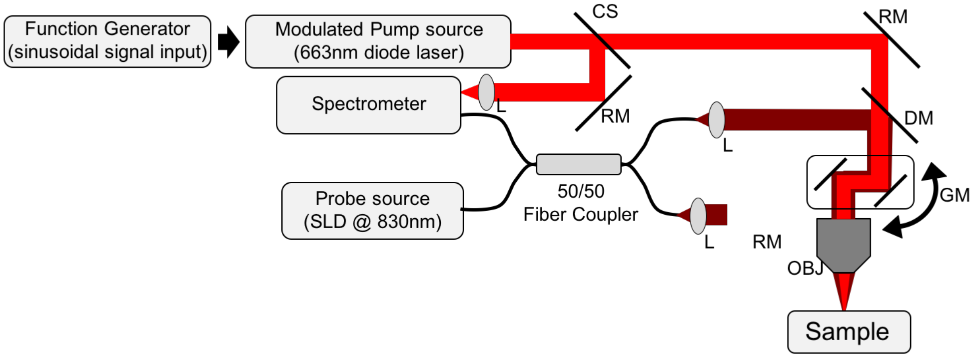

Figure 35: A schematic diagram of frequency-domain PPOCT (FD-PPOCT).

The FD-PPOCT system is described in Figure 35. Based on PPOCT system, a small amount of the pump beam was reflected with a microscope cover glass and directed onto a few pixels at the edge of pixel array in spectrometer in order to establish a reference phase signal. As following same protocol to change the oxygen level of the MB microsphere above, the phantom was directly bubbled air or nitrogen gas into the MB microsphere solution. Two of each 100 µm inside diameter plastic capillary tubes contained a solution of oxi/deoxygenated MB microspheres. In order to maintain oxygen level during scanning, two ends of each capillary tube was fully sealed. The tube was positioned at an angle to avoid the strong specular reflection from the tube surface.

The functional signal due to the absorption of the pump was frequency encoded by a 10 kHz sinusoidal modulation. The phase signal from the reference beam and the MB solution were then extracted at the modulation frequency from an M-scan via Fourier transform along the time. Because signals are shifted by the reference phase angle ($\emptyset_{\mathrm{Ref}}$), the measured phase ($\emptyset_{\mathrm{messured}}$) that we extracted from an M-scan data contains both the reference phase shift and the phase value ($\emptyset_{\mathrm{MB}}$) of interest from MB solution due to transient absorption. The actual phase should be calculated with the phase difference from $\emptyset_{\mathrm{MB}} = \emptyset_{\mathrm{measured}} - \emptyset_{\mathrm{Ref}}$.

5.2 Results

5.2.1 Fabricating and characterizing microencapsulated MB

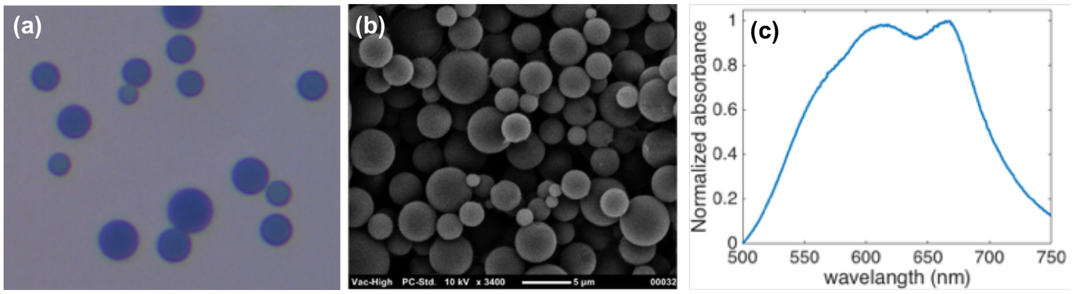

Figure 36: Microencapsulated MB. (a) taken from a bright field microscope (b) taken from the SEM (c) absorption spectrum

Figure 36(a) is a light microscope image of the fabricated microspheres loaded with the 0.01 % w/v MB solution. We can clearly see bluish microspheres. In Figure 36(b), the average diameter of the bluish microspheres was ~ 2.5 um from a scanning electron microscope (SEM). The absorption spectrum has a peak at around 660nm that is similar with raw MB.

5.2.2 Imaging microencapsulated MB using PPOCT

Figure 37(a), (b) and (c) composite OCT/PPOCT images of the tissue phantom described above. The PPOCT signal was processed with the background subtraction method before being overlain on the gray scale OCT image. The background noise level was measured and averaged from above and below (±2 kHz) pump-modulation frequency of PPOCT signal. The PPOCT signal at the modulation frequency is divided by the calculated background noise level. In order to completely remove the background noise signal, we set a threshold of 3 multiplied with standard deviation of background region on the treated PPOCT image. This algorithm was applied on each pixel in the PPOCT b-scan image. The algorithm is same with *in vivo* zebra fish experiment above [138]. In Figure 37(a), when the 660 nm pump laser is on, the PPOCT signal from the MB microsphere inside of a capillary is clearly visible in the blue-scale color image. While the MB microspheres were flowing within the capillary tube, the velocity was low enough that most of microspheres settled down to the lower half of the tube. Figure 37(b) is the composite image with the pump radiation blocked.

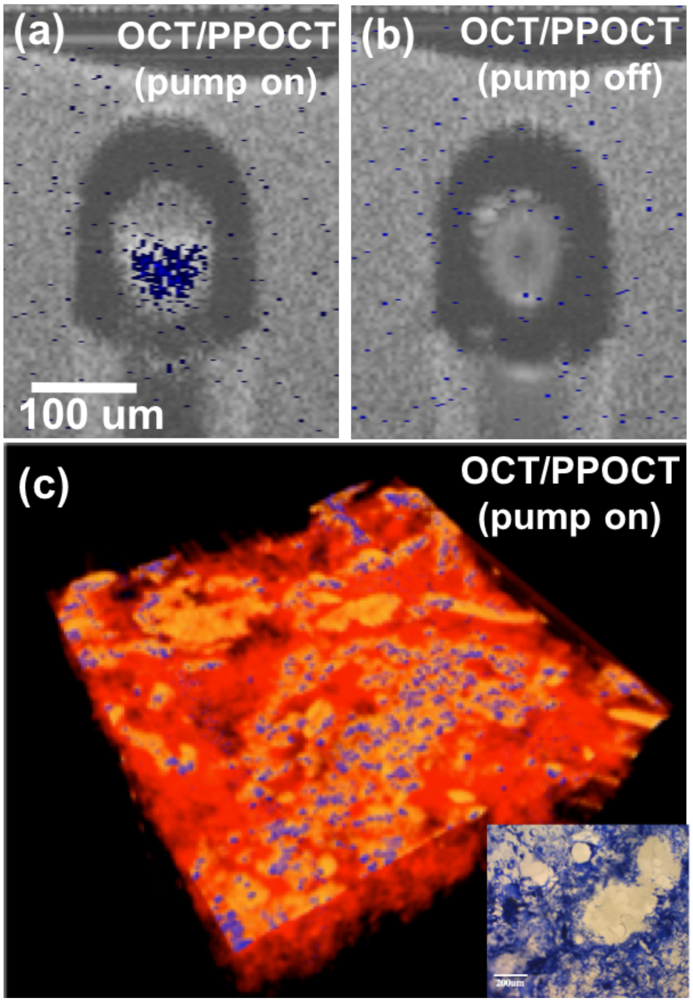

Figure 37: PPOCT images overlaid with OCT images from MB microspheres. (a),(b) b-scan images (PPOCT: blue-scaled, OCT: gray-scaled), (c) volume image (PPOCT: blue-scaled, OCT: red-scaled, the lower-right-corner: gelatin-based artificail tissue sprilinked with MB microspheres imaged from a bright field microscope)

We only see the OCT gray-scaled signal from the microspheres within the capillary tube and the intralipid emulsion. This confirms the signal is pump induced and essentially background free after using the background removal technique noted above. In Figure 37(c), the 3D volume image of OCT/PPOCT was taken from the monolayer phantom mentioned above. At the lower-right-corner of Figure 37, the image taken from a bright field microscope shows a gelatin-based artificial tissue phantom with MB microspheres. The microspheres were sprinkled on the top surface of the artificial tissue to create the monolayer phantom that effectevely mimic the case of active tagging. The volume image of OCT/PPOCT clearly shows PPOCT signal on the top of the artificial tissue.

5.2.3 Measuring the lifetime of transient absorption from microencapsulated MB quenching by oxygen

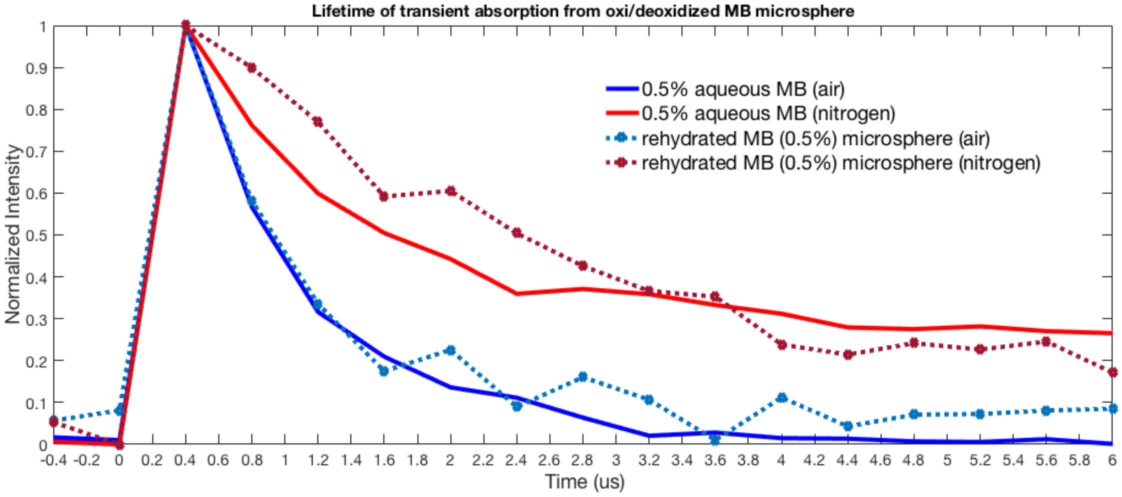

Figure 38: Lifetime of the transient absorption from oxi/deoxygenated 0.5% aqueous MB and microencapsualted MB using time-resolved pump-probe spectroscopy

By varying the oxygen concentration of the aqueous and microencapsulated MB with 0 or 21%, lifetime of the transient absorption was changed. Normalized lifetime intensity of the transient absorption is displayed in Figure 38. In case of air-bubbled, the lifetime of both 0.5% aqueous and rehydrated MB solution is quite same with around 1 us. The lifetime of deoxygenated 0.5% aqueous MB solution is about 1.8 us that is shorter than about 2.5 us of the deoxygenated MB microsphere. This could be happened by either the molecule of nitrogen could not well escape within a polymer shell or oxygen molecule could not penetrate into a polymer shell after deoxygenating.

5.2.4 Measuring the theoretical phase sensitivity and shift of FD-PPOCT system

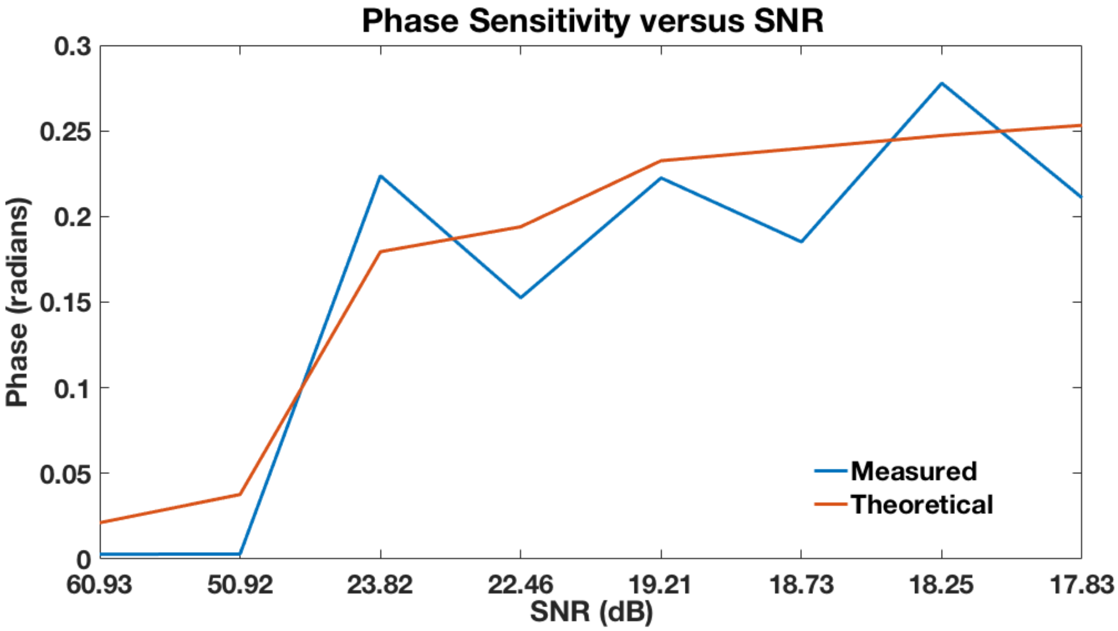

Figure 39: Theoretical and experimental phase sensitivity of FD-PPOCT system by varying SNR

We measured the experimental phase sensitivity using FD-PPOCT system. The algorithm to extract phase signal is similar with the PPOCT A-scan process described above. However, after Fourier transforming along the time domain of OCT M-scan, the phase, not magnitude for PPOCT, is extracted at the modulation frequency of pump. In each SNR case, the standard deviation were calculated from 30 measurements that implys the system phase variation. Based on the phase sensitivity at Eq. 1, we estimated the theoretical phase sensitivy from the SNR of the measurements.

The experimental phase variations are comparably matched with theoretical values. As expecting, the phase sensitivity explicitly depends on the function of the SNR.

5.2.5 Measuring the phase shift of microencapsulated MB quenching by oxygen

We measured the phase differences of microencapsulated MB solution with different concentration of oxygen.

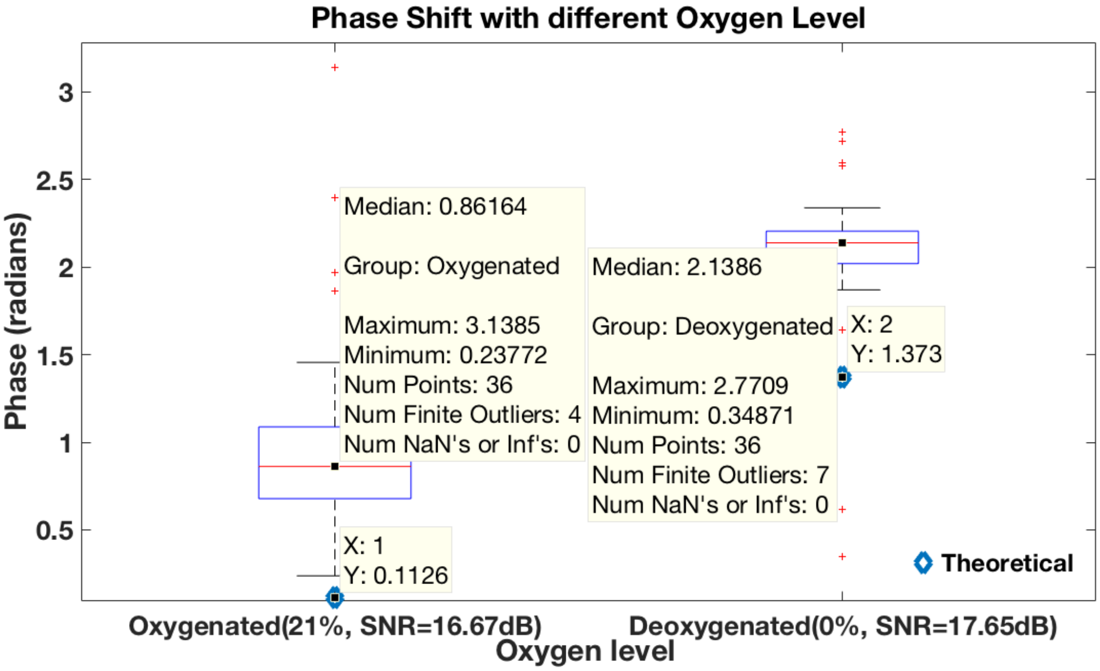

Figure 40: Measured phase shift from the MB microsphere solution dissolved with two different oxygen levels, 21% oxygenated and 0% dioxygenated

A 21% oxygen concentration solution was made by bubbling atmospheric air into the microencapsulated MB solution. The bubbler ensured a relatively homogenous solution. In case of each oxygen data, the statistical values are calculated from 36 measurments. The mean of phase angle was 0.861 with a standard deviation of 0.574. To get a 0% oxygen concentration, the nitogen gas was bubbed into the microencapsulated MB solution. Under these conditions the mean phase angle was 2.1386 with a standard deviation of 0.4501. Clearly the phase angle is capable of differentiating the two oxygen concentrations. The difference of two phases is 1.277. Based on the Eq. 1 about the phase sensitivity related SNR of PPCOT siganl, some sample signal having low SNR causes larger standard deviations. The measured PPOCT SNR of both oxygen condition were 16.67 and 17.65 dB.

We can also estimate the relative phase angle for the two oxygen concentrations based on the theory above and literature values for MB lifetimes under different oxygen conditions. Based on the theoretical equation, $\phi = \tan^{-1} \omega\tau$, where ω is the pump modulation frequency and τ is the triplet state lifetime [138]. The 21% oxygen-dissolved solution had 1.8us lifetime [162] and phase angle was 0.112. The 0% oxygen-leveled solution had 79.5 us [162] lifetime and phase angle was 1.373. The difference of two theoretical phase is 1.261. By comparison the experimental with theoretical phase angle, experimental result does not match with the theoretical value because the experimental phase imports relative values. But the differece values are well matched. We would need to calirate the inherent phase lag of the system to get the absolute phase shift. In fact we could use this experimental phase shift to get the calibrated phase lag.

DISCUSSION

In this dissertation, molecular contrast-enhanced imaging systems were built for OCT. Based on combining pump-probe spectroscopic technique, PPOCT system has been well researched and characterized to measure endogenous and exogenous molecular with morphological information. In order to extend PPOCT applications, UFORJ is developed for endoscopic imaging and a microencapsulate MB is developed for the new biocompatible contrast agent.

Firstly, using a novel, two-color Fourier-domain PPOCT system, the first in vivo cross-sectional PPOCT images of Xenopus tadpole vasculature were obtained. Additionally, varying the interpulse delay enabled differentiation of PPOCT signals originating from Methylene Blue and hemoglobin. PPOCT imaging of vasculature was com- pared to pvOCT and DOCT and determined to more accurately demarcate tortuous microvasculature, while still maintaining the data needed to calculate flow information.

Secondly, the introduction of the 663-nm diode laser, which acts as the pump in this implementation of pump-probe OCT (PPOCT), represents a minor modification to an otherwise typical OCT system. A newly developed background subtraction technique completely removes all background from intensity noise at the pump modulation frequency, simplifying the interpretation of PPOCT images. These developments have enabled the first in vivo imaging of MB with PPOCT that requires only minor modification to a standard 830-nm OCT system but enables efficient detecion of methylene blue (MB). The limit of MB detection (SNR 1 dB) for a 15-μm-thick sample at a depth of 0.5mm, derived from phantom studies, is 41 μM.

Thirdly, we have shown that a lensless fiber optic rotary joint, constructed by butting the ends of a fixed and rotating bare fiber, can be made to operate over a broad spectral range with low insertion loss. Using distilled water as the lubricant and index matching fluid enabled operation down into the UV, at least to 355 nm, and only limited by the absorption spectrum of water and chromatic losses in the chosen fiber. The rotary joint could also be operated at high rotational velocities. It was tested up to 8800 rpm. At this velocity, there is very little added intensity noise due to rotational misalignment and no discernable change in the observed spatial mode of the 1310 nm light.

Lastly, we have developed a novel microencapsulated MB contrast agent using an FDA approved biocompatible polymer. The microsphere encapsulation improves the PPOCT signal both by enhancing the scattering and preventing the reduction of MB to leucomethylene blue. The surface of the microsphere can readily be functionalized to enable active targeting of the contrast agent without modifying the excited state dynamics of MB that enable PPOCT imaging. PPOCT imaging of a tissue phantom show strong signals from the microspheres with essentially no background. Based on the success of the tissue phantom imaging we are working towards actively tagging a receptor for the first PPOCT imaging of an actively tagged contrast agent. By changing the oxygen level of a microencapsulated MB, we present preliminary experiments demonstrating a frequency domain phase angle measurement of PPOCT imaging technique from variance oxygen-leveled MB solution.

SUMMARY

Biological imaging techniques that are able to detect a contrast-enhanced signal from the target molecules have been widely applied to various techniques in the imaging field. The complex biological environment provides numerous and more efficient pathways along which the chromophores (light absorber) may release its energy. This energy can provide not only morphological information, but also specific molecular information such as a biochemical map of a sample. All diseases correlate with both morphological and biochemical changes.

Optical coherence tomography (OCT) system is one of the biological imaging techniques. OCT has widely been applied to many medical/clinical fields, giving benefit from a penetration depth of a few millimeters while maintaining a spatial resolution on the order of a micron [2-11]. Utilizing OCT, it is possible to selectively detect the ballistic propagation of backscattered light in a tissue medium. This backscattered light does not undergo randomized scattering or deflection to any optical beam pathway of the tissue. In a tissue medium, the intensity of backscattered light is varied from spatial variations in tissue refractive index. By measuring the variations, the sample images from OCT are generated.

Unfortunately, OCT lacks the straightforward functional molecular imaging extensions available for other technologies, e.g. confocal fluorescence microscopy and fluorescence diffuse optical tomography. This is largely because incoherent processes such as fluorescence emission and Raman scattering are not readily detectable with low

coherence interferometry that is the central technique that underlies all OCT systems. Despite a drawback of molecular imaging with OCT, it is highly desirable to measure not only morphological, but also molecular information from either endogenous or exogenous molecules.

In order to overcome the limitation of molecular contrast imaging for OCT, we propose the hybrid OCT imaging technique and a new exogenous contrast agent. Our contrast-enhanced imaging technique integrates OCT with a well-researched and well-established technique: two-colored pump-probe absorption spectroscopy. Our novel imaging technique is called Pump-Probe OCT (PPOCT). By using PPOCT, we firstly imaged Hemoglobin (Hb) from direct in vivo imaging and also Methylene Blue (MB) as the molecular contrast agent widely applied for the clinical fields [32-37, 161].

Based upon current successful results, molecular imaging with OCT potentially gives us the ability to identify pathologies. In order to expand the capacity of PPOCT, we developed ultra-wideband lensless optic fiber rotary joint with excellent performance (<0.2 dB insertion loss with high rotational velocities up to 8800 rpm). To the best of our knowledge this is the first demonstration of this type of rotary joint capable of such a wide bandwidth and high rotational velocities. By manipulating the new contrast agent based on the technique by evaporating solvent with MB, we fabricated the microencapsulated MB as a new biocompatible contrast agent suitable for PPOCT. Also we have developed a FD-PPOCT system and algorithms for detecting the excited state lifetime in the frequency domain. We observed that the relative phase shift between the pump and probe is a reliable indicator of the oxygen concentration. Furthermore, these results are in good agreement with our theoretical predictions. This development opens up the possibility of using MB for 3-D oxygen sensing with PPOCT.

Future work for this project involves ex vivo postmortem human coronary artery testing of functional tagging of MB microspheres that play an important role in atherosclerosis and it may be possible to use this technique for retinal oxygen saturation measurements.

REFERENCES

[1] P Mattison, Scott, Wihan Kim, Jesung Park, and Brian E Applegate. "Molecular Imaging in Optical Coherence Tomography." Current molecular imaging 3, no. 2 (2014): 88-105.

[2] Gora, Michalina J., Jenny S. Sauk, Robert W. Carruth, Kevin A. Gallagher, Melissa J. Suter, Norman S. Nishioka, Lauren E. Kava, Mireille Rosenberg, Brett E. Bouma, and Guillermo J. Tearney. "Tethered capsule endomicroscopy enables less invasive imaging of gastrointestinal tract microstructure." Nature medicine 19, no. 2 (2013): 238-240.

[3] Chen, Y., A. D. Aguirre, P-L. Hsiung, S. Desai, P. R. Herz, M. Pedrosa, Q. Huang et al. "Ultrahigh resolution optical coherence tomography of Barrett’s esophagus: preliminary descriptive clinical study correlating images with histology." Endoscopy 39, no. 07 (2007): 599-605.

[4] Karl, A., H. Stepp, E. Willmann, A. Buchner, Y. Hocaoglu, C. Stief, and S. Tritschler. "Optical coherence tomography for bladder cancer-ready as a surrogate for optical biopsy?-results of a prospective mono-centre study." European journal of medical research 15, no. 3 (2010): 131.

[5] Kim, Chang Soo, Petra Wilder-Smith, Yeh-Chan Ahn, Lih-Huei L. Liaw, Zhongping Chen, and Young Jik Kwon. "Enhanced detection of early-stage oral cancer in vivo by optical coherence tomography using multimodal delivery of gold nanoparticles." Journal of biomedical optics 14, no. 3 (2009): 034008-034008.

[6] Jo, Javier A., Brian E. Applegate, Jesung Park, Sebina Shrestha, Paritosh Pande, Irma B. Gimenez-Conti, and Jimi L. Brandon. "In vivo simultaneous morphological and biochemical optical imaging of oral epithelial cancer." IEEE Transactions on Biomedical Engineering 57, no. 10 (2010): 2596-2599.

[7] Gladkova, Natalya D., G. A. Petrova, N. K. Nikulin, S. G. Radenska- Lopovok, L. B. Snopova, Yu P. Chumakov, V. A. Nasonova et al. "In vivo optical coherence tomography imaging of human skin: norm and pathology." Skin Research and Technology 6, no. 1 (2000): 6-16.

[8] Greaves, N., B. Benatar, M. Baguneid, and A. Bayat. "Is nonivasive optical coherence tomography a reliable alternative to invasive histological assessment of acute wound healing in human skin?." In would repair and regeration, vol. 21, no. 6, pp. A66-A66. 11 river st, hoboken 07030-5774, NJ USA: Wiley-blackwell, 2013.

[9] Srinivas, Shyam M., Johannes F. de Boer, Hyle Park, Kourosh Keikhanzadeh, L. Huang Huai-en, Jun Zhang, Woong Qyu Jung, Zhongping Chen, and J. Stuart Nelson. "Determination of burn depth by polarization-sensitive optical coherence tomography." Journal of Biomedical Optics 9, no. 1 (2004): 207-212.

[10] Nguyen, Freddy T., Adam M. Zysk, Eric J. Chaney, Jan G. Kotynek, Uretz J. Oliphant, Frank J. Bellafiore, Kendrith M. Rowland, Patricia A. Johnson, and Stephen A. Boppart. "Intraoperative evaluation of breast tumor margins with optical coherence tomography." Cancer research 69, no. 22 (2009): 8790-879.

[11] Alawi, Seyed Arash, Monika Kuck, Caroline Wahrlich, Sebastian Batz, Gordon McKenzie, Joachim W. Fluhr, Juergen Lademann, and Martina Ulrich. "Optical coherence tomography for presurgical margin assessment of non- melanoma skin cancer–a practical approach." Experimental dermatology 22, no. 8 (2013): 547-551.

[12] Drexler, Wolfgang, and James G. Fujimoto, eds. Optical coherence tomography: technology and applications. Springer Science & Business Media, 2008.

[13] Klein, Thomas, Wolfgang Wieser, Raphael André, Tom Pfeiffer, Christoph M. Eigenwillig, and Robert Huber. "Multi-MHz FDML OCT: snapshot retinal imaging at 6.7 million axial-scans per second." In SPIE BiOS, pp. 82131E-82131E. International Society for Optics and Photonics, 2012.

[14] Xu, Jingjiang, Chi Zhang, Jianbing Xu, K. K. Y. Wong, and K. K. Tsia. "Megahertz all-optical swept-source optical coherence tomography based on broadband amplified optical time-stretch." Optics letters 39, no. 3 (2014): 622-625.

[15] Skala, Melissa C., Matthew J. Crow, Adam Wax, and Joseph A. Izatt. "Photothermal optical coherence tomography of epidermal growth factor receptor in live cells using immunotargeted gold nanospheres." Nano letters 8, no. 10 (2008): 3461-3467.

[16] Adler, Desmond C., Shu-Wei Huang, Robert Huber, and James G. Fujimoto. "Photothermal detection of gold nanoparticles using phase-sensitive optical coherence tomography." Optics Express 16, no. 7 (2008): 4376-4393.

[17] Oldenburg, Amy, Farah Toublan, Kenneth Suslick, Alexander Wei, and Stephen Boppart. "Magnetomotive contrast for in vivo optical coherence tomography." Optics Express 13, no. 17 (2005): 6597-6614.

[18] Oldenburg, Amy L., Caterina M. Gallippi, Frank Tsui, Timothy C. Nichols, Kellie N. Beicker, Raghav K. Chhetri, Dmitry Spivak, Aaron Richardson, and Thomas H. Fischer. "Magnetic and contrast properties of labeled platelets for magnetomotive optical coherence tomography." Biophysical journal 99, no. 7 (2010): 2374-2383.

[19] Robles, Francisco E., Christy Wilson, Gerald Grant, and Adam Wax. "Molecular imaging true-colour spectroscopic optical coherence tomography." Nature photonics 5, no. 12 (2011): 744-747.

[20] Li, You Leo, Kevin Seekell, Hsiangkuo Yuan, Francisco E. Robles, and Adam Wax. "Multispectral nanoparticle contrast agents for true-color spectroscopic optical coherence tomography." Biomedical optics express 3, no. 8 (2012): 1914-1923.

[21] Telenkov, Sergey A., Digant P. Dave, and Thomas E. Milner. "Low-coherence optical probe for non-contact detection of photothermal and photoacoustic phenomena in biomaterials." In AIP conference proceedings, no. A, pp. 852-858. IOP publishing LTD, 2003.

[22] Yin, Biwei, Roman V. Kuranov, Austin B. McElroy, Shams Kazmi, Andrew K. Dunn, Timothy Q. Duong, and Thomas E. Milner. "Dual-wavelength photothermal optical coherence tomography for imaging microvasculature blood oxygen saturation." Journal of biomedical optics 18, no. 5 (2013): 056005-056005.

[23] Oldenburg, Amy, Farah Toublan, Kenneth Suslick, Alexander Wei, and Stephen Boppart. "Magnetomotive contrast for in vivo optical coherence tomography." Optics Express 13, no. 17 (2005): 6597-6614.

[24] Oldenburg, Amy L., Caterina M. Gallippi, Frank Tsui, Timothy C. Nichols, Kellie N. Beicker, Raghav K. Chhetri, Dmitry Spivak, Aaron Richardson, and Thomas H. Fischer. "Magnetic and contrast properties of labeled platelets for magnetomotive optical coherence tomography." Biophysical journal 99, no. 7 (2010): 2374-2383.

[25] Oldenburg, Amy L., Gongting Wu, Dmitry Spivak, Frank Tsui, Alisa S. Wolberg, and Thomas H. Fischer. "Imaging and elastometry of blood clots using magnetomotive optical coherence tomography and labeled platelets." IEEE Journal of Selected Topics in Quantum Electronics 18, no. 3 (2012): 1100-1109.

[26] Morgner, U., W. Drexler, F. X. Kärtner, X. D. Li, C. Pitris, E. P. Ippen, and J. G. Fujimoto. "Spectroscopic optical coherence tomography." Optics letters 25, no. 2 (2000): 111-113.

[27] Kang, Jin U., and Xuan Liu. "High resolution hemoglobin oxygen saturation level imaging using Morlet wavelet transformed spectroscopic Optical Coherence Tomography." In 2010 IEEE International Symposium on Biomedical Imaging: From Nano to Macro, pp. 1431-1434. IEEE, 2010.

[28] Xu, Chenyang, Farzad Kamalabadi, and Stephen A. Boppart. "Comparative performance analysis of time–frequency distributions for spectroscopic optical coherence tomography." Applied optics 44, no. 10 (2005): 1813-1822.

[29] Oldenburg, Amy L., Chenyang Xu, and Stephen A. Boppart. "Spectroscopic optical coherence tomography and microscopy." IEEE Journal of Selected Topics in Quantum Electronics 13, no. 6 (2007): 1629-1640.

[30] Robles, Francisco E., Christy Wilson, Gerald Grant, and Adam Wax. "Molecular imaging true-colour spectroscopic optical coherence tomography." Nature photonics 5, no. 12 (2011): 744-747.

[31] Carmichael, Ian, and Gordon L. Hug. "Triplet–triplet absorption spectra of organic molecules in condensed phases." Journal of physical and chemical reference data 15, no. 1 (1986): 1-250.

[32] Schirmer, R. Heiner, Boubacar Coulibaly, August Stich, Michael Scheiwein, Heiko Merkle, Jana Eubel, Katja Becker et al. "Methylene blue as an antimalarial agent." Redox report 8, no. 5 (2003): 272-275.

[33] Tardivo, Joao Paulo, Auro Del Giglio, Carla Santos de Oliveira, Dino Santesso Gabrielli, Helena Couto Junqueira, Dayane Batista Tada, Divinomar Severino, Rozane de Fátima Turchiello, and Mauricio S. Baptista. "Methylene blue in photodynamic therapy: from basic mechanisms to clinical applications." Photodiagnosis and Photodynamic Therapy 2, no. 3 (2005): 175-191.

[34] Link, E. M., P. J. Blower, D. C. Costa, D. M. Lane, D. Lui, R. S. D. Brown, P. J. Ell, and M. F. Spittle. "Early detection of melanoma metastases with radioiodinated methylene blue." European journal of nuclear medicine 25, no. 9 (1998): 1322-1329.

[35] Song, Louis Michel Wong Kee, Douglas G. Adler, Bipan Chand, Jason D. Conway, Joseph MB Croffie, James A. DiSario, Daniel S. Mishkin et al. "Chromoendoscopy." Gastrointestinal endoscopy 66, no. 4 (2007): 639-649.

[36] Gonzalez-Bejar, Maria, Pedro Montes-Navajas, Hermenegildo García, and J. C. Scaiano. "Methylene blue encapsulation in cucurbit [7] uril: laser flash photolysis and near-IR luminescence studies of the interaction with oxygen." Langmuir 25, no. 18 (2009): 10490-10494.

[37] Olliver, J. R., C. P. Wild, P. Sahay, S. Dexter, and L. J. Hardie. "Chromoendoscopy with methylene blue and associated DNA damage in Barrett's oesophagus." The Lancet 362, no. 9381 (2003): 373-374..

[38] Mills, Andrew, and Jishun Wang. "Photobleaching of methylene blue sensitised by TiO 2: an ambiguous system?." Journal of Photochemistry and Photobiology A: Chemistry 127, no. 1 (1999): 123-134.

[39] Applegate, Brian, Changhuei Yang, and Joseph Izatt. "Theoretical comparison of the sensitivity of molecular contrast optical coherence tomography techniques." Optics express 13, no. 20 (2005): 8146-8163..

[40] Li, Ming, Olivier Rouaud, and Denis Poncelet. "Microencapsulation by solvent evaporation: State of the art for process engineering approaches." International Journal of pharmaceutics 363, no. 1 (2008): 26-39.

[41] Makadia, Hirenkumar K., and Steven J. Siegel. "Poly lactic-co-glycolic acid (PLGA) as biodegradable controlled drug delivery carrier." Polymers 3, no. 3 (2011): 1377-1397.

[42] Swanhart, Lisa M., Chiara Cianciolo Cosentino, Cuong Q. Diep, Alan J. Davidson, Mark de Caestecker, and Neil A. Hukriede. "Zebrafish kidney development: basic science to translational research." Birth Defects Research Part C: Embryo Today: Reviews 93, no. 2 (2011): 141-156.

[43] Telenkov, Sergey A., Digant P. Dave, and Thomas E. Milner. "Low-coherence optical probe for non-contact detection of photothermal and photoacoustic phenomena in biomaterials." In AIP CONFERENCE PROCEEDINGS, no. A, pp. 852-858. IOP INSTITUTE OF PHYSICS PUBLISHING LTD, 2003.

[44] Telenkov, Sergey A., Digant P. Dave, Shriram Sethuraman, Taner Akkin, and Thomas E. Milner. "Differential phase optical coherence probe for depth-resolved detection of photothermal response in tissue." Physics in medicine and biology 49, no. 1 (2003): 111.

[45] Akkin, Taner, Digant P. Davé, Jong- In Youn, Sergey A. Telenkov, H. Grady Rylander, and Thomas E. Milner. "Imaging tissue response to electrical and photothermal stimulation with nanometer sensitivity." Lasers in Surgery and Medicine 33, no. 4 (2003): 219-225.

[46] Kim, Jihoon, Junghwan Oh, and Thomas E. Milner. "Measurement of optical path length change following pulsed laser irradiation using differential phase optical coherence tomography." Journal of biomedical optics 11, no. 4 (2006): 041122-041122.

[47] Guan, Guangying, Roberto Reif, Zhihong Huang, and Ruikang K. Wang. "Depth profiling of photothermal compound concentrations using phase sensitive optical

coherence tomography." Journal of biomedical optics 16, no. 12 (2011): 126003-1260039.

[48] Skala, Melissa C., Matthew J. Crow, Adam Wax, and Joseph A. Izatt. "Photothermal optical coherence tomography of epidermal growth factor receptor in live cells using immunotargeted gold nanospheres." Nano letters 8, no. 10 (2008): 3461-3467.

[49] Tucker-Schwartz, J. M., T. A. Meyer, C. A. Patil, C. L. Duvall, and M. C. Skala. "In vivo photothermal optical coherence tomography of gold nanorod contrast agents." Biomedical optics express 3, no. 11 (2012): 2881-2895.

[50] Adler, Desmond C., Shu-Wei Huang, Robert Huber, and James G. Fujimoto. "Photothermal detection of gold nanoparticles using phase-sensitive optical coherence tomography." Optics Express 16, no. 7 (2008): 4376-4393.

[51] Boyer, David, Philippe Tamarat, Abdelhamid Maali, Brahim Lounis, and Michel Orrit. "Photothermal imaging of nanometer-sized metal particles among scatterers." Science 297, no. 5584 (2002): 1160-1163.

[52] Tucker-Schwartz, Jason M., Tu Hong, Daniel C. Colvin, Yaqiong Xu, and Melissa C. Skala. "Dual-modality photothermal optical coherence tomography and magnetic-resonance imaging of carbon nanotubes." Optics letters 37, no. 5 (2012): 872-874.

[53] Zhou, Chao, Tsung-Han Tsai, Desmond C. Adler, Hsiang-Chieh Lee, David W. Cohen, Amy Mondelblatt, Yihong Wang, James L. Connolly, and James G.

Fujimoto. "Photothermal optical coherence tomography in ex vivo human breast tissues using gold nanoshells." Optics letters 35, no. 5 (2010): 700-702.

[54] Pache, Christophe, Noelia L. Bocchio, Arno Bouwens, Martin Villiger, Corinne Berclaz, Joan Goulley, Matthew I. Gibson, Christian Santschi, and Theo Lasser. "Fast three-dimensional imaging of gold nanoparticles in living cells with photothermal optical lock-in Optical Coherence Microscopy." Optics express 20, no. 19 (2012): 21385-21399.

[55] Kennedy, Laura C., Lissett R. Bickford, Nastassja A. Lewinski, Andrew J. Coughlin, Ying Hu, Emily S. Day, Jennifer L. West, and Rebekah A. Drezek. "A New Era for Cancer Treatment: Gold- Nanoparticle- Mediated Thermal Therapies." Small 7, no. 2 (2011): 169-183.

[56] Zhang, Hongtao, Alan Berezov, Qiang Wang, Geng Zhang, Jeffrey Drebin, Ramachandran Murali, and Mark I. Greene. "ErbB receptors: from oncogenes to targeted cancer therapies." The Journal of clinical investigation 117, no. 8 (2007): 2051-2058.

[57] Lynch, Thomas J., Daphne W. Bell, Raffaella Sordella, Sarada Gurubhagavatula, Ross A. Okimoto, Brian W. Brannigan, Patricia L. Harris et al. "Activating mutations in the epidermal growth factor receptor underlying responsiveness of non–small-cell lung cancer to gefitinib." New England Journal of Medicine 350, no. 21 (2004): 2129-2139.

[58] Puvanakrishnan, Priyaveena, Parmeswaran Diagaradjane, S. M. Kazmi, Andrew K. Dunn, Sunil Krishnan, and James W. Tunnell. "Narrow band imaging of

squamous cell carcinoma tumors using topically delivered anti- EGFR antibody conjugated gold nanorods." Lasers in surgery and medicine 44, no. 4 (2012): 310-317.

[59] Keely, N. O., and M. J. Meegan. "Targeting tumors using estrogen receptor ligand conjugates." Current cancer drug targets 9, no. 3 (2009): 370-380.

[60] Kasaragod, Deepa, Kin Man Au, Zenghai Lu, David Childs, Steven P. Armes, and Stephen J. Matcher. "Photothermal detection of the contrast properties of polypyrrole nanoparticles using optical coherence tomography." In SPIE BiOS, pp. 85960R-85960R. International Society for Optics and Photonics, 2013.

[61] Subhash, Hrebesh M., Hui Xie, Jeffrey W. Smith, and Owen JT McCarty. "Optical detection of indocyanine green encapsulated biocompatible poly (lactic-co-glycolic) acid nanoparticles with photothermal optical coherence tomography." Optics letters 37, no. 5 (2012): 981-983.

[62] Jung, Yeongri, Guangying Guan, Chen-wei Wei, Roberto Reif, Xiaohu Gao, Matthew O'Donnell, and Ruikang K. Wang. "Multifunctional nanoprobe to enhance the utility of optical based imaging techniques." Journal of biomedical optics 17, no. 1 (2012): 0160151-0160156.

[63] Maslov, Konstantin, Gheorghe Stoica, and Lihong V. Wang. "In vivo dark-field reflection-mode photoacoustic microscopy." Optics letters 30, no. 6 (2005): 625-627.

[64] Yao, Da-Kang, Ruimin Chen, Konstantin Maslov, Qifa Zhou, and Lihong V. Wang. "Optimal ultraviolet wavelength for in vivo photoacoustic imaging of cell nuclei." Journal of biomedical optics 17, no. 5 (2012): 0560041-0560047.

[65] Zhang, Chi, Yu Shrike Zhang, Da-Kang Yao, Younan Xia, and Lihong V. Wang. "Label-free photoacoustic microscopy of cytochromes." Journal of biomedical optics 18, no. 2 (2013): 020504-020504.

[66] Tay, Benjamin Chia-Meng, Tzu-Hao Chow, Beng-Koon Ng, and Thomas Kwok-Seng Loh. "Dual-window dual-bandwidth spectroscopic optical coherence tomography metric for qualitative scatterer size differentiation in tissues." IEEE Transactions on Biomedical Engineering 59, no. 9 (2012): 2439-2448.

[67] Yin, Biwei, Roman V. Kuranov, Austin B. McElroy, Shams Kazmi, Andrew K. Dunn, Timothy Q. Duong, and Thomas E. Milner. "Dual-wavelength photothermal optical coherence tomography for imaging microvasculature blood oxygen saturation." Journal of biomedical optics 18, no. 5 (2013): 056005-056005.

[68] Raschke, G., S. Brogl, A. S. Susha, A. L. Rogach, T. A. Klar, J. Feldmann, B. Fieres et al. "Gold nanoshells improve single nanoparticle molecular sensors." Nano letters 4, no. 10 (2004): 1853-1857.

[69] Wang, Yi, Weiping Qian, Yong Tan, and Shaohua Ding. "A label-free biosensor based on gold nanoshell monolayers for monitoring biomolecular interactions in diluted whole blood." Biosensors and Bioelectronics 23, no. 7 (2008): 1166-1170.

[70] Skala, Melissa C., Matthew J. Crow, Adam Wax, and Joseph A. Izatt. "Photothermal optical coherence tomography of epidermal growth factor receptor

in live cells using immunotargeted gold nanospheres." Nano letters 8, no. 10 (2008): 3461-3467.

[71] Su, Chia-Hao, Hwo-Shuenn Sheu, Chia-Yun Lin, Chih-Chia Huang, Yi-Wei Lo, Ying-Chih Pu, Jun-Cheng Weng, Dar-Bin Shieh, Jyh-Horng Chen, and Chen-Sheng Yeh. "Nanoshell magnetic resonance imaging contrast agents." Journal of the American Chemical Society 129, no. 7 (2007): 2139-2146.

[72] Gobin, André M., Min Ho Lee, Naomi J. Halas, William D. James, Rebekah A. Drezek, and Jennifer L. West. "Near-infrared resonant nanoshells for combined optical imaging and photothermal cancer therapy." Nano letters 7, no. 7 (2007): 1929-1934.

[73] Coughlin, Andrew J., Jeyarama S. Ananta, Nanfu Deng, Irina V. Larina, Paolo Decuzzi, and Jennifer L. West. "Gadolinium- Conjugated Gold Nanoshells for Multimodal Diagnostic Imaging and Photothermal Cancer Therapy." Small 10, no. 3 (2014): 556-565.

[74] Nanospectra Biosciences I. [cited 2014 January 29]; Available from: http://www.nanospectra.com/about/about.html.

[75] Morgner, U., W. Drexler, F. X. Kärtner, X. D. Li, C. Pitris, E. P. Ippen, and J. G. Fujimoto. "Spectroscopic optical coherence tomography." Optics letters 25, no. 2 (2000): 111-113.

[76] Schmitt, J. M., S. H. Xiang, and K. M. Yung. "Differential absorption imaging with optical coherence tomography." JOSA A 15, no. 9 (1998): 2288-2296.

[77] Yang, Changhuei, Laura EL McGuckin, John D. Simon, Michael A. Choma, Brian E. Applegate, and Joseph A. Izatt. "Spectral triangulation molecular contrast optical coherence tomography with indocyanine green as the contrast agent." Optics letters 29, no. 17 (2004): 2016-2018.

[78] Robles, Francisco E., Christy Wilson, Gerald Grant, and Adam Wax. "Molecular imaging true-colour spectroscopic optical coherence tomography." Nature photonics 5, no. 12 (2011): 744-747.

[79] Xu, Chenyang, Farzad Kamalabadi, and Stephen A. Boppart. "Comparative performance analysis of time–frequency distributions for spectroscopic optical coherence tomography." Applied optics 44, no. 10 (2005): 1813-1822.

[80] Jaedicke, Volker, Semih Agcaer, Francisco E. Robles, Marian Steinert, David Jones, Sebastian Goebel, Nils C. Gerhardt, Hubert Welp, and Martin R. Hofmann. "Comparison of different metrics for analysis and visualization in spectroscopic optical coherence tomography." Biomedical optics express 4, no. 12 (2013): 2945-2961.

[81] Bosschaart, Nienke, Maurice C. Aalders, Dirk J. Faber, Jelmer J. Weda, Martin J. van Gemert, and Ton G. van Leeuwen. "Quantitative measurements of absorption spectra in scattering media by low-coherence spectroscopy." Optics letters 34, no. 23 (2009): 3746-3748.

[82] Kang, Jin U., and Xuan Liu. "High resolution hemoglobin oxygen saturation level imaging using Morlet wavelet transformed spectroscopic Optical Coherence

Tomography." In 2010 IEEE International Symposium on Biomedical Imaging: From Nano to Macro, pp. 1431-1434. IEEE, 2010.

[83] Oldenburg, Amy L., Chenyang Xu, and Stephen A. Boppart. "Spectroscopic optical coherence tomography and microscopy." IEEE Journal of Selected Topics in Quantum Electronics 13, no. 6 (2007): 1629-1640.

[84] Bosschaart, Nienke, Ton G. van Leeuwen, Maurice CG Aalders, and Dirk J. Faber. "Quantitative comparison of analysis methods for spectroscopic optical coherence tomography." Biomedical optics express 4, no. 11 (2013): 2570-2584.

[85] Xu, Chenyang, Jian Ye, Daniel L. Marks, and Stephen A. Boppart. "Near-infrared dyes as contrast-enhancing agents for spectroscopic optical coherence tomography." Optics letters 29, no. 14 (2004): 1647-1649.

[86] Oldenburg, Amy L., Matthew N. Hansen, Tyler S. Ralston, Alexander Wei, and Stephen A. Boppart. "Imaging gold nanorods in excised human breast carcinoma by spectroscopic optical coherence tomography." Journal of materials chemistry 19, no. 35 (2009): 6407-6411.

[87] Khlebtsov, Nikolai G., and Lev A. Dykman. "Optical properties and biomedical applications of plasmonic nanoparticles." Journal of Quantitative Spectroscopy and Radiative Transfer 111, no. 1 (2010): 1-35.

[88] Li, You Leo, Kevin Seekell, Hsiangkuo Yuan, Francisco E. Robles, and Adam Wax. "Multispectral nanoparticle contrast agents for true-color spectroscopic optical coherence tomography." Biomedical optics express 3, no. 8 (2012): 1914-1923.

[89] Pircher, Michael, Erich Götzinger, Rainer Leitgeb, Adolf Fercher, and Christoph Hitzenberger. "Measurement and imaging of water concentration in human cornea with differential absorption optical coherence tomography." Optics Express 11, no. 18 (2003): 2190-2197.

[90] Fleming, Christine P., Jocelyn Eckert, Elkan F. Halpern, Joseph A. Gardecki, and Guillermo J. Tearney. "Depth resolved detection of lipid using spectroscopic optical coherence tomography." Biomedical optics express 4, no. 8 (2013): 1269-1284.

[91] Barnes, R. J., M. S. Dhanoa, and Susan J. Lister. "Standard normal variate transformation and de-trending of near-infrared diffuse reflectance spectra." Applied spectroscopy 43, no. 5 (1989): 772-777.

[92] Faber, Dirk J., Egbert G. Mik, Maurice CG Aalders, and Ton G. van Leeuwen. "Toward assessment of blood oxygen saturation by spectroscopic optical coherence tomography." Optics letters 30, no. 9 (2005): 1015-1017.

[93] Faber, Dirk J., Egbert G. Mik, Maurice CG Aalders, and Ton G. van Leeuwen. "Light absorption of (oxy-) hemoglobin assessed by spectroscopic optical coherence tomography." Optics letters 28, no. 16 (2003): 1436-1438.

[94] Bosschaart, Nienke, Dirk J. Faber, Ton G. Van Leeuwen, and Maurice CG Aalders. "In vivo low-coherence spectroscopic measurements of local hemoglobin absorption spectra in human skin." Journal of biomedical optics 16, no. 10 (2011): 100504-100504.

[95] Oldenburg, Amy, Farah Toublan, Kenneth Suslick, Alexander Wei, and Stephen Boppart. "Magnetomotive contrast for in vivo optical coherence tomography." Optics Express 13, no. 17 (2005): 6597-6614.

[96] Oldenburg, Amy L., Vasilica Crecea, Stephanie A. Rinne, and Stephen A. Boppart. "Phase-resolved magnetomotive OCT for imaging nanomolar concentrations of magnetic nanoparticles in tissues." Optics express 16, no. 15 (2008): 11525-11539.

[97] Hamaguchi, Shigeaki, Iwai Tohnai, Akira Ito, Kenji Mitsudo, Toshio Shigetomi, Masafumi Ito, Hiroyuki Honda, Takeshi Kobayashi, and Minoru Ueda. "Selective hyperthermia using magnetoliposomes to target cervical lymph node metastasis in a rabbit tongue tumor model." Cancer science 94, no. 9 (2003): 834-839.

[98] Oldenburg, Amy L., Vasilica Crecea, Stephanie A. Rinne, and Stephen A. Boppart. "Phase-resolved magnetomotive OCT for imaging nanomolar concentrations of magnetic nanoparticles in tissues." Optics express 16, no. 15 (2008): 11525-11539..

[99] Oldenburg, Amy L., Caterina M. Gallippi, Frank Tsui, Timothy C. Nichols, Kellie N. Beicker, Raghav K. Chhetri, Dmitry Spivak, Aaron Richardson, and Thomas H. Fischer. "Magnetic and contrast properties of labeled platelets for magnetomotive optical coherence tomography." Biophysical journal 99, no. 7 (2010): 2374-2383.

[100] Crecea, Vasilica, Adeel Ahmad, and Stephen A. Boppart. "Magnetomotive optical coherence elastography for microrheology of biological tissues." Journal of biomedical optics 18, no. 12 (2013): 121504-121504.

[101] Pouliquen, D., R. Perdrisot, A. Ermias, S. Akoka, P. Jallet, and J. J. Le Jeune. "Superparamagnetic iron oxide nanoparticles as a liver MRI contrast agent: contribution of microencapsulation to improved biodistribution." Magnetic resonance imaging 7, no. 6 (1989): 619-627.

[102] Chen, Hongyu, Daniel C. Colvin, Bin Qi, Thomas Moore, Jian He, O. Thompson Mefford, Frank Alexis, John C. Gore, and Jeffrey N. Anker. "Magnetic and optical properties of multifunctional core–shell radioluminescence nanoparticles." Journal of materials chemistry 22, no. 25 (2012): 12802-12809.

[103] Madru, Renata, Pontus Kjellman, Fredrik Olsson, Karin Wingårdh, Christian Ingvar, Freddy Ståhlberg, Johan Olsrud et al. "99mTc-labeled superparamagnetic iron oxide nanoparticles for multimodality SPECT/MRI of sentinel lymph nodes." Journal of Nuclear Medicine 53, no. 3 (2012): 459-463.

[104] Kim, Jeehyun, Junghwan Oh, Thomas E. Milner, and J. Stuart Nelson. "Hemoglobin contrast in magnetomotive optical Doppler tomography." Optics letters 31, no. 6 (2006): 778-780.

[105] Debus, E. S., G. Torsello, T. Schmitz-Rixen, T. Hupp, W. Lang, T. Noppeney, A. Oberhuber, and R. T. Grundmann. "Manifestationen und Prävention der Arteriosklerose." Gefässchirurgie 18, no. 7 (2013): 644-651.

[106] Oh, Junghwan, Marc D. Feldman, Jihoon Kim, Hyun Wook Kang, Pramod Sanghi, and Thomas E. Milner. "Magneto- motive detection of tissue- based macrophages by differential phase optical coherence tomography." Lasers in surgery and medicine 39, no. 3 (2007): 266-272.

[107] Kim, Jongsik, Adeel Ahmad, Marina Marjanovic, Eric J. Chaney, Joanne Li, Jonathan Rasio, Zita Hubler, Darold Spillman, Kenneth S. Suslick, and Stephen A. Boppart. "Magnetomotive optical coherence tomography for the assessment of atherosclerotic lesions using αvβ3 integrin-targeted microspheres." Molecular Imaging and Biology 16, no. 1 (2014): 36-43.

[108] Tal, M., C. R. King, M. H. Kraus, A. Ullrich, J. Schlessinger, and D. Givol. "Human HER2 (neu) promoter: evidence for multiple mechanisms for transcriptional initiation." Molecular and cellular biology 7, no. 7 (1987): 2597-2601.

[109] John, Renu, Freddy T. Nguyen, Kenneth J. Kolbeck, Eric J. Chaney, Marina Marjanovic, Kenneth S. Suslick, and Stephen A. Boppart. "Targeted multifunctional multimodal protein-shell microspheres as cancer imaging contrast agents." Molecular Imaging and Biology 14, no. 1 (2012): 17-24.

[110] Oldenburg, Amy L., Gongting Wu, Dmitry Spivak, Frank Tsui, Alisa S. Wolberg, and Thomas H. Fischer. "Imaging and elastometry of blood clots using magnetomotive optical coherence tomography and labeled platelets." IEEE Journal of Selected Topics in Quantum Electronics 18, no. 3 (2012): 1100-1109.

[111] Broughton 2nd, G., Jeffrey E. Janis, and Christopher E. Attinger. "The basic science of wound healing." Plastic and reconstructive surgery 117, no. 7 Suppl (2006): 12S-34S.

[112] Liang, Xing, Vasilica Crecea, and Stephen A. Boppart. "Dynamic optical coherence elastography: a review." Journal of innovative optical health sciences 3, no. 04 (2010): 221-233.

[113] Bloembergen, Nicolaas, Richard K. Chang, S. S. Jha, and C. H. Lee. "Optical second-harmonic generation in reflection from media with inversion symmetry." Physical Review 174, no. 3 (1968): 813.

[114] Sarunic, Marinko V., Brian E. Applegate, and Joseph A. Izatt. "Spectral domain second-harmonic optical coherence tomography." Optics letters 30, no. 18 (2005): 2391-2393.

[115] Fraser, R. D. B., and T. P. MacRae. "The crystalline structure of collagen fibrils in tendon." Journal of molecular biology 127, no. 1 (1979): 129-133.

[116] Shoulders, Matthew D., and Ronald T. Raines. "Collagen structure and stability." Annual review of biochemistry 78 (2009): 929.

[117] Jiang, Yi, Ivan Tomov, Yimin Wang, and Zhongping Chen. "Second-harmonic optical coherence tomography." Optics letters 29, no. 10 (2004): 1090-1092.

[118] Jiang, Yi, Ivan V. Tomov, Yimin Wang, and Zhongping Chen. "High-resolution second-harmonic optical coherence tomography of collagen in rat-tail tendon." Applied Physics Letters 86, no. 13 (2005): 133901.

[119] Applegate, Brian E., Changhuei Yang, Andrew M. Rollins, and Joseph A. Izatt. "Polarization-resolved second-harmonic-generation optical coherence tomography in collagen." Optics letters 29, no. 19 (2004): 2252-2254..

[120] Jo, Javier A., Brian E. Applegate, Jesung Park, Sebina Shrestha, Paritosh Pande, Irma B. Gimenez-Conti, and Jimi L. Brandon. "In vivo simultaneous morphological and biochemical optical imaging of oral epithelial cancer." IEEE Transactions on Biomedical Engineering 57, no. 10 (2010): 2596-2599.

[121] Hariri, Lida P., Erica R. Liebmann, Samuel L. Marion, Patricia B. Hoyer, John R. Davis, Molly A. Brewer, and Jennifer K. Barton. "Simultaneous optical coherence tomography and laser induced fluorescence imaging in rat model of ovarian carcinogenesis." Cancer biology & therapy 10, no. 5 (2010): 438-447.

[122] Hariri, Lida P., Alexandre R. Tumlinson, David G. Besselsen, Urs Utzinger, Eugene W. Gerner, and Jennifer K. Barton. "Endoscopic optical coherence tomography and laser- induced fluorescence spectroscopy in a murine colon cancer model." Lasers in surgery and medicine 38, no. 4 (2006): 305-313.

[123] Wall, R. Andrew, Garret T. Bonnema, and Jennifer K. Barton. "Focused Optical Coherence Tomography and Laser-Induced Fluorescence Endoscope." In LASERS IN SURGERY AND MEDICINE, pp. 72-72. DIV JOHN WILEY & SONS INC, 111 RIVER ST, HOBOKEN, NJ 07030 USA: WILEY-LISS, 2010.

[124] Park, Jesung, Javier A. Jo, Sebina Shrestha, Paritosh Pande, Qiujie Wan, and Brian E. Applegate. "A dual-modality optical coherence tomography and fluorescence lifetime imaging microscopy system for simultaneous morphological and biochemical tissue characterization." Biomedical optics express 1, no. 1 (2010): 186-200.

[125] Yuan, Shuai, Qian Li, James Jiang, Alex Cable, and Yu Chen. "Three-dimensional coregistered optical coherence tomography and line-scanning fluorescence laminar optical tomography." Optics letters 34, no. 11 (2009): 1615-1617.

[126] Chen, Yu, Shuai Yuan, Jeremiah Wierwille, Renee Naphas, Qian Li, Tiffany R. Blackwell, Paul T. Winnard Jr, Venu Raman, and Kristine Glunde. "Integrated optical coherence tomography (OCT) and fluorescence laminar optical tomography (FLOT)." IEEE Journal of Selected Topics in Quantum Electronics 16, no. 4 (2010): 755-766.

[127] Patil, Chetan A., Nienke Bosschaart, Matthew D. Keller, Ton G. van Leeuwen, and Anita Mahadevan-Jansen. "Combined Raman spectroscopy and optical coherence tomography device for tissue characterization." Optics letters 33, no. 10 (2008): 1135-1137.

[128] Ashok, Praveen C., Bavishna B. Praveen, Nicola Bellini, Andrew Riches, Kishan Dholakia, and C. Simon Herrington. "Multi-modal approach using Raman spectroscopy and optical coherence tomography for the discrimination of colonic adenocarcinoma from normal colon." Biomedical optics express 4, no. 10 (2013): 2179-2186.

[129] Mahadevan-Jansen, Anita, and Rebecca R. Richards-Kortum. "Raman spectroscopy for the detection of cancers and precancers." Journal of Biomedical Optics 1, no. 1 (1996): 31-70.

[130] Georgakoudi, Irene, Brian C. Jacobson, Markus G. Müller, Ellen E. Sheets, Kamran Badizadegan, David L. Carr-Locke, Christopher P. Crum et al. "NAD (P)

H and collagen as in vivo quantitative fluorescent biomarkers of epithelial precancerous changes." Cancer research 62, no. 3 (2002): 682-687.

[131] Carrasco- Zevallos, Oscar, Ryan L. Shelton, Wihan Kim, Jeremy Pearson, and Brian E. Applegate. "In vivo pump- probe optical coherence tomography imaging in Xenopus laevis." Journal of biophotonics 8, no. 1-2 (2015): 25-35.

[132] Applegate, Brian E., and Joseph A. Izatt. "Molecular imaging of endogenous and exogenous chromophores using ground state recovery pump-probe optical coherence tomography." Optics express 14, no. 20 (2006): 9142-9155.

[133] Yaqoob, Zahid, Emily McDowell, Jigang Wu, Xin Heng, Jeff Fingler, and Changhuei Yang. "Molecular contrast optical coherence tomography: a pump-probe scheme using indocyanine green as a contrast agent." Journal of biomedical optics 11, no. 5 (2006): 054017-054017.

[134] Rao, K. Divakar, Michael A. Choma, Siavash Yazdanfar, Andrew M. Rollins, and Joseph A. Izatt. "Molecular contrast in optical coherence tomography by use of a pump–probe technique." Optics letters 28, no. 5 (2003): 340-342.

[135] Jacob, Desmond, Ryan L. Shelton, and Brian E. Applegate. "Fourier domain pump-probe optical coherence tomography imaging of Melanin." Optics express 18, no. 12 (2010): 12399-12410.

[136] Wan, Qiujie, and Brian E. Applegate. "Multiphoton coherence domain molecular imaging with pump-probe optical coherence microscopy." Optics letters 35, no. 4 (2010): 532-534.

[137] Yang, Changhuei, Michael A. Choma, Laura E. Lamb, John D. Simon, and Joseph A. Izatt. "Protein-based molecular contrast optical coherence tomography with phytochrome as the contrast agent." Optics letters 29, no. 12 (2004): 1396-1398.

[138] Kim, Wihan, and Brian E. Applegate. "In vivo molecular contrast OCT imaging of methylene blue." Optics letters 40, no. 7 (2015): 1426-1429.

[139] Applegate, Brian, Changhuei Yang, and Joseph Izatt. "Theoretical comparison of the sensitivity of molecular contrast optical coherence tomography techniques." Optics express 13, no. 20 (2005): 8146-8163.

[140] Gonzalez-Bejar, Maria, Pedro Montes-Navajas, Hermenegildo García, and J. C. Scaiano. "Methylene blue encapsulation in cucurbit [7] uril: laser flash photolysis and near-IR luminescence studies of the interaction with oxygen." Langmuir 25, no. 18 (2009): 10490-10494.

[141] Barton, Jennifer Kehlet, George Frangineas, Herbert Pummer, and John F. Black. "Cooperative phenomena in two- pulse, two- color laser photocoagulation of cutaneous blood vessels." Photochemistry and Photobiology 73, no. 6 (2001): 642-650.

[142] Black, John F., and Jennifer Kehlet Barton. "Chemical and structural changes in blood undergoing laser photocoagulation." Photochemistry and photobiology 80, no. 1 (2004): 89-97.

[143] Boelsterli, Urs A. Mechanistic toxicology: the molecular basis of how chemicals disrupt biological targets. CRC Press, 2007.

[144] Black, John F., Norman Wade, and Jennifer Kehlet Barton. "Mechanistic comparison of blood undergoing laser photocoagulation at 532 and 1,064 nm." Lasers in surgery and medicine 36, no. 2 (2005): 155-165.

[145] Adler, Desmond C., Shu-Wei Huang, Robert Huber, and James G. Fujimoto. "Photothermal detection of gold nanoparticles using phase-sensitive optical coherence tomography." Optics Express 16, no. 7 (2008): 4376-4393.

[146] Kuranov, Roman V., Jinze Qiu, Austin B. McElroy, Arnold Estrada, Anthony Salvaggio, Jeffrey Kiel, Andrew K. Dunn, Timothy Q. Duong, and Thomas E. Milner. "Depth-resolved blood oxygen saturation measurement by dual-wavelength photothermal (DWP) optical coherence tomography." Biomedical optics express 2, no. 3 (2011): 491-504.

[147] Draijer, Matthijs, Erwin Hondebrink, Ton van Leeuwen, and Wiendelt Steenbergen. "Review of laser speckle contrast techniques for visualizing tissue perfusion." Lasers in medical science 24, no. 4 (2009): 639-651.

[148] Stücker, M., V. Baier, T. Reuther, K. Hoffmann, K. Kellam, and P. Altmeyer. "Capillary blood cell velocity in human skin capillaries located perpendicularly to the skin surface: measured by a new laser Doppler anemometer." Microvascular research 52, no. 2 (1996): 188-192.

[149] Shchors, Ksenya, and Gerard Evan. "Tumor angiogenesis: cause or consequence of cancer?." Cancer research 67, no. 15 (2007): 7059-7061.

[150] Vakoc, Benjamin J., Dai Fukumura, Rakesh K. Jain, and Brett E. Bouma. "Cancer imaging by optical coherence tomography: preclinical progress and clinical potential." Nature Reviews Cancer 12, no. 5 (2012): 363-368.

[151] van Munster, Erik B., and Theodorus WJ Gadella. "Fluorescence lifetime imaging microscopy (FLIM)." In Microscopy techniques, pp. 143-175. Springer Berlin Heidelberg, 2005.

[152] Flock, Stephen T., Steven L. Jacques, Brian C. Wilson, Willem M. Star, and Martin JC van Gemert. "Optical properties of Intralipid: a phantom medium for light propagation studies." Lasers in surgery and medicine 12, no. 5 (1992): 510-519.

[153] Lieschke, Graham J., and Peter D. Currie. "Animal models of human disease: zebrafish swim into view." Nature Reviews Genetics 8, no. 5 (2007): 353-367.

[154] Golshan, Mehra, and Faina Nakhlis. "Can methylene blue only be used in sentinel lymph node biopsy for breast cancer?." The breast journal 12, no. 5 (2006): 428-430.

[155] Disanto, Anthony R., and John G. Wagner. "Pharmacokinetics of highly ionized drugs II: methylene blue—absorption, metabolism, and excretion in man and dog after oral administration." Journal of pharmaceutical sciences 61, no. 7 (1972): 1086-1090.

[156] Kim, Wihan, Xi Chen, Javier A. Jo, and Brian E. Applegate. "Lensless, ultra-wideband fiber optic rotary joint for biomedical applications." Optics letters 41, no. 9 (2016): 1973-1976.

[157] Gilsdorf, Robert W., and Joseph C. Palais. "Single-mode fiber coupling efficiency with graded-index rod lenses." Applied optics 33, no. 16 (1994): 3440-3445.

[158] Mynbaev, Djafar K., and Lowell L. Scheiner. Fiber-optic communications technology. Prentice Hall, 2001.

[159] Li, Ming, Olivier Rouaud, and Denis Poncelet. "Microencapsulation by solvent evaporation: State of the art for process engineering approaches." International Journal of pharmaceutics 363, no. 1 (2008): 26-39.

[160] Choma, Michael A., Audrey K. Ellerbee, Changhuei Yang, Tony L. Creazzo, and Joseph A. Izatt. "Spectral-domain phase microscopy." Optics letters 30, no. 10 (2005): 1162-1164.

[161] Wright, Robert O., William J. Lewander, and Alan D. Woolf. "Methemoglobinemia: etiology, pharmacology, and clinical management." Annals of emergency medicine 34, no. 5 (1999): 646-656

[162] Gonzalez-Bejar, Maria, Pedro Montes-Navajas, Hermenegildo García, and J. C. Scaiano. "Methylene blue encapsulation in cucurbit [7] uril: laser flash photolysis and near-IR luminescence studies of the interaction with oxygen." Langmuir 25, no. 18 (2009): 10490-10494.